Optimizing spectral electrical impedance tomography technology for improved subsurface characterization

von der Fakultät Bau- und Umweltingenieurwissenschaften der Universität Stuttgart zur Erlangung der Würde eines Doktor-Ingenieurs (Dr.-Ing.) genehmigte Abhandlung

vorgelegt von

Haoran Wang

aus Xiangyang, China

Hauptberichter:	Prof. Dr. Johan Alexander Huisman
Mitberichter:	Prof. Dr. Florian M. Wagner

Tag der mündlichen Prüfung 14.11.2023

Institut für Wasser- und Umweltsystemmodellierung (IWS) der Universität Stuttgart
2023

In memory of my great mom,

Che, Xiaohong (1966-2022)

纪念我伟大的母亲：

车小红 （1966-2022）

她倾尽一生成就了现在以及未来的我

妈，我好想你。

Declaration of authorship

I, Haoran Wang, declare that this thesis titled, "Optimizing spectral electrical impedance tomography technology for improved subsurface characterization" and the work presented in it are my own. Due acknowledgement has been made in the text to all the other works and materials that were used.

Hiermit erkläre ich, Haoran Wang, dass diese Arbeit nur meine Originalarbeit umfasst und dass ich die vorliegende Dissertation "Optimizing spectral electrical impedance tomography technology for improved subsurface characterization" unabhängig geschrieben habe. Alle anderen verwendeten Quellen und Materialien wurden im Text entsprechend anerkannt.

Signature: ______________________________

Date: ______________________________

Acknowledgements

This PhD project was funded by the China Scholarship Council (CSC) with project number 201908440295.

First, I would like to express my gratitude to my supervisor, Prof. Dr. Johan Alexander (Sander) Huisman. Over the past four years, he has always been patient in guiding me, explaining my questions, and discussing solutions to the challenges encountered in my research. During the early stage of my PhD, when I was not fully familiar with the details of my research topic, he would sit down with me, using a pencil and a piece of paper to do calculations together and gradually guide me through. I enjoyed every brainstorming session with him, as they were always enlightening. With his help, I was able to quickly immerse myself in my research and make good progress. Afterwards, he gave me the necessary autonomy while providing support in different ways. He introduced me to collaborative research opportunities and supported additional research ideas. I would like to mention one more story from the times of the COVID-19 pandemic. When I expressed that a meeting in person would help me better understand and address research issues, he specifically came to the research center to meet with me, even though he had originally planned to work from home. Beyond all of this, there have been many details over these four years that have made me feel appreciated. I am grateful for the opportunity to work with Sander, who is talented, knowledgeable, responsible, and optimistic. I also want to thank him for his help in writing, as he always manages to clear the fog and guide me to better present my work. For those who are considering or are about to work with him, I would never hesitate to recommend it.

Secondly, I would like to extend my sincere thanks to Dr. Egon Zimmerman. His nice publication (*Zimmermann et al.*, 2019) inspired and initiated my research work. Basically, two chapters in my thesis were developed based on the ideas and data in his paper. Thanks to him for sharing the data, that allowed me to work on advanced sEIT measurements and make further improvements. He actively participated in my research and in the regular weekly meetings, and helped me solve many technical problems. I learned a lot from his expertise, especially in electronics and electrical systems. I enjoyed discussions with him and will fondly remember the many electric circuits he drew to explain my questions. Without his help, I would not been able to achieve the results presented in this thesis.

I would also like to express my gratitude to Prof. Dr. Harry Vereecken and Prof. Dr. Jan Vanderborght for their interest and suggestions during the PhD report discussions and seminars. I am grateful to Dr. Maximilian Weigand for the inspiring discussions about EIT inversion, which helped to improve this part of my thesis significantly. I would also like to thank Prof. Dr. Adrian Mellage and Cora Strobel for the opportunity to play with borehole SIP measurements, which is a stimulating research direction for further development of the methods presented in this thesis. I also want to thank Prof. Dr. Florian Wagner for agreeing to examine my thesis. I extend my thanks to my colleagues at IBG-3, Odilia Esser and Ansgar Weuthen, as well as Walter Glaas from ZEA-2, for their assistance with my field experiments. I appreciate the help of Gaby Pillert, Dr. Marie-Isabel Ludwig, and Dr. Kathrin Vermöhlen in administrative matters.

My gratitude also goes to my office mates and fellow PhD students, Tarig Bukhary, Dr. Joseph Piotrowski, Olga Dombrowski, Yafei Huang, David Mengen, Lukas Strebel, Theresa Boas, and Dr. Yi Yu, for all the good times we shared during these years. I also feel grateful to Fang Li for continuous free supply of fantastic homemade chili oil. I would also like to thank my neighbor Dr. Ling Zou for often sharing delicious food and snacks. Furthermore, a special thanks to my friend Hanjin Wu for always sharing happy things and bringing endless laughter.

Lastly, I want to say thanks to my two aunties, my mother's sisters. They supported me in the most difficult time of my life.

Abstract

Spectral electrical impedance tomography (sEIT) is a promising geophysical method to image the subsurface complex electrical conductivity distribution in a broad frequency range (i.e. mHz to kHz). sEIT has received increasing interest in recent years, especially in the case of environmental and hydrogeophysical applications. Promising laboratory results have demonstrated the usefulness of broadband spectral induced polarization (SIP) measurements. It is now desirable to obtain accurate and broadband imaging results at the field scale. However, there is still a range of challenges that need to be addressed to achieve accurate sEIT imaging at the field scale. In this context, the aim of this thesis is to enhance the applicability of sEIT technology at the field scale by improving the inversion of complex EIT data and developing strategies to address so-called electromagnetic coupling effects at high frequencies.

In a first step, key questions associated with the inversion of complex EIT data were addressed. In particular, a new inversion strategy that simultaneously considers the coupling between real and imaginary parts of the complex data and model and the separated treatment in terms of data weighting and model regularization was proposed. This newly proposed strategy was then compared with three existing inversion strategies. The first strategy (CVI) formulates the inverse problem in the complex number domain and is mathematically the most elegant method. The second strategy (RVI) is the established real-valued inversion method, which decouples the inversion of the real and imaginary parts and completely ignores the complex nature of the data and model. The third strategy (ALT) is very similar to the RVI strategy in terms of small phase angles, but it considers the complex coupling in the forward operator and alternately updates the real and imaginary of the model in the presence of large phase angles. The different inversion strategies were tested with two synthetic models that differed in the range of considered phase values. In the case of the model with a small phase angle, the CVI strategy was able to resolve the distribution of the electrical conductivity amplitude, but the inversion result for the phase angle was less reliable. The other three strategies presented similar results and the models were well resolved within the expected data error. In the case of the model with large phase angles, only the newly formulated CVI+ strategy was able to produce reliable inversion results. It was found that the cross-sensitivity provided unique information during the inversion, and should be carefully considered when the mean value of the measured phase angle is larger than 50 mrad. It was concluded that the CVI+ strategy is theoretically the most comprehensive and correct approach for EIT inversion. In the case of small phase angles, the RVI strategy has the practical advantage that no complex calculations are required, which substantially reduces the required computational effort.

In a second step, the influence of inductive coupling on the measured complex impedance was evaluated for different electrode and cable configurations. A novel index to evaluate the inductive coupling strength (ICS) was proposed and used as a data filter to select data with limited inductive coupling. In addition, the inductive coupling strength was evaluated for different cable layouts, subsurface properties, and electrode configurations for a short electrode layout with 30 electrodes and 1 m electrode spacing. It was found that a fan-shaped cable layout should be preferred over more commonly used layouts with parallel multicore cables because the wire separation in the fan-shaped layout is much larger than in multicore cables, which allows for more measurements with small ICS. Using a fan-shaped cable layout, further analysis showed that accurate sEIT measurements that do not need correction for inductive coupling are difficult to obtain for highly conductive but weakly polarizable subsurface materials. The analysis of different types of electrode configurations showed that the widely used α type electrode configurations have a much higher ICS than other types of electrode configurations when using a fan-shaped cable layout. Using a synthetic modelling study with a fan-shaped cable layout, reliable inversion results were achieved without data correction for inductive coupling if measurements with high ICS values were filtered out before inversion. Finally, the novel filtering approach was tested with actual surface sEIT measurements. The EIT inversion results based on the filtered data corresponded well with inversion results using data corrected for inductive coupling and also showed good spectral consistency. It was concluded that it is possible to achieve reliable inversion results without data correction for inductive coupling when a fan-shaped layout and configurations with sufficiently low inductive coupling strength are used.

In a third and final step, an approach to estimate measurement errors due to capacitive coupling was proposed based on EIT modelling considering capacitances and leakage currents. It was found that the imaginary part of the impedance due to the capacitive coupling can be separately modelled without considering the imaginary part of the electrical conductivity distribution. A workflow was then proposed to calculate the capacitive coupling strength (CCS) for each electrode configuration, which is defined as the ratio of the imaginary part of the impedance induced by capacitive coupling and the imaginary part of the impedance due to the soil electrical conductivity. In the first step of this workflow, the distribution of the real part of the electrical conductivity is determined. The obtained 2D distribution was mapped to a 3D model and the total capacitance between the cable shield and ground was distributed along the cables by integrating capacitances at the corresponding nodes in the 3D forward model. Forward modelling with the real part of the electrical conductivity distribution, integrated capacitances and measured leakage currents was then conducted to obtain the imaginary part of the impedance induced by capacitive coupling. Finally, the CCS values for all considered measurements were calculated by assuming that all other sources of errors are negligible. It was found that measurements with large normalized leakage current are more likely to have high CCS values. In the end, measurements with low CCS values were selected for inversion and the results were compared with inversion results obtained with a so-called complete electrode configuration. The inversion results using CCS-filtered configurations showed good spectral consistency without correction for capacitive coupling. It was concluded that filtering based on CCS is promising and of great potential to achieve consistent and reliable sEIT imaging results over a broad frequency range up to the kHz frequency range.

Overall, this thesis provides an important contribution to the establishment of the sEIT method for accurate imaging of the subsurface complex electrical conductivity distribution in the mHz to kHz frequency range at the field scale. A new comprehensive complex inversion approach was proposed, enabling accurate inversion of field sEIT measurements with large phase angles. Comparison of this new approach with other strategies clarified the feasibility of using simplified strategies for the inversion of sEIT measurements with small phase angles. Data filters were proposed to deal with EM coupling effects in broadband sEIT measurements. With the use of the developed filtering approaches, reliable inversion results in a broad frequency range up to kHz were successfully achieved without correction of EM coupling.

Zusammenfassung

Die spektrale elektrische Impedanztomographie (sEIT) ist eine vielversprechende geophysikalische Methode zur bildgebenden Messung der komplexen elektrischen Leitfähigkeitsverteilung im Untergrund in einem breiten Frequenzbereich (von mHz bis kHz). sEIT hat in den letzten Jahren zunehmendes Interesse gefunden, insbesondere bei umwelt- und hydrogeophysikalischen Anwendungen. Vielversprechende Laborergebnisse haben das Potential von breitbandigen Messungen der spektral induzierten Polarisation (SIP) gezeigt. Es ist nun wünschenswert auch für bildgebende Messungen auf der Feldskala genaue und breitbandige Ergebnisse zu erhalten. Es gibt jedoch noch eine Reihe von Herausforderungen, die angegangen werden müssen, um eine genaue sEIT-Abbildung des Untergrundes auf der Feldskala zu erreichen. In diesem Zusammenhang besteht das Ziel dieser Arbeit darin, die Anwendbarkeit der sEIT-Technologie auf der Feldskala durch die Verbesserung der Inversion komplexer EIT-Daten und die Entwicklung von Strategien zur Bewältigung sogenannter elektromagnetischer Kopplungseffekte bei hohen Frequenzen zu verbessern.

In einem ersten Schritt wurden zentrale Fragen im Zusammenhang mit der Inversion komplexer EIT-Daten behandelt. Insbesondere wurde eine neue Inversionsstrategie (CVI+) vorgeschlagen, die gleichzeitig die Kopplung zwischen realen und imaginären Teilen der komplexen Daten und des Modells sowie die getrennte Behandlung in Bezug auf die Datengewichtung und die Modellregularisierung berücksichtigt. Diese neu vorgeschlagene Strategie wurde dann mit drei bestehenden Inversionsstrategien verglichen. Die erste Strategie (CVI) formuliert das inverse Problem im Bereich der komplexen Zahlen und ist mathematisch gesehen die eleganteste Methode. Die zweite Strategie (RVI) ist die etablierte reellwertige Inversionsmethode, die die Inversion des Real- und Imaginärteils entkoppelt und die Komplexwertigkeit der Daten und des Modells vollständig ignoriert. Die dritte Strategie (ALT) ist der RVI-Strategie in Bezug auf kleine Phasenwinkel sehr ähnlich, berücksichtigt aber die komplexe Kopplung im Vorwärtsoperator und aktualisiert bei großen Phasenwinkeln abwechselnd den Real- und Imaginärteil des Modells. Die ver-

schiedenen Inversionsstrategien wurden mit zwei synthetischen Modellen getestet, die sich durch den Phasenbereich unterschieden. Für das Modell mit einem kleinen Phasenbereich konnte die CVI-Strategie die Amplitudenverteilung der elektrischen Leitfähigkeit auflösen, aber das Inversionsergebnis für den Phasenwinkel war weniger zuverlässig. Die anderen drei Strategien lieferten ähnliche Ergebnisse und die Modelle wurden innerhalb des erwarteten Datenfehlers gut aufgelöst. Im Falle des Modells mit großen Phasenwinkeln war nur die neu formulierte CVI+-Strategie in der Lage, zuverlässige Inversionsergebnisse zu liefern. Es wurde festgestellt, dass die Kreuzsensitivität einzigartige Informationen während der Inversion lieferte und sorgfältig berücksichtigt werden sollte, wenn der Mittelwert des gemessenen Phasenwinkels größer als 50 mrad ist. Es wurde festgestellt, dass die CVI+-Strategie theoretisch der umfassendste und korrekteste Ansatz für die EIT-Inversion ist. Bei kleinen Phasenwinkeln hat die RVI-Strategie den praktischen Vorteil, dass keine komplexen Berechnungen erforderlich sind, was den erforderlichen Rechenaufwand erheblich reduziert.

In einem zweiten Schritt wurde der Einfluss der induktiven Kopplung auf die gemessene komplexe Impedanz für verschiedene Elektroden- und Kabelkonfigurationen bewertet. Ein neuartiger Index zur Bewertung der induktiven Kopplungsstärke (ICS) wurde vorgeschlagen und als Datenfilter verwendet, um Daten mit kleiner induktiver Kopplung auszuwählen. Darüber hinaus wurde die induktive Kopplungsstärke für verschiedene Kabellayouts, Untergrundeigenschaften und Elektrodenkonfigurationen für ein kurzes Elektrodenlayout mit 30 Elektroden und 1 m Elektrodenabstand evaluiert. Es wurde festgestellt, dass ein fächerförmiges Kabellayout gegenüber den üblicherweise verwendeten Layouts mit parallelen mehradrigen Kabeln zu bevorzugen ist, da der Drahtabstand im fächerförmigen Layout viel größer ist als bei mehradrigen Kabeln, wodurch kleinere ICS bei den Messungen erzielt werden. Weitere Analysen zeigten, dass genaue sEIT-Messungen ohne Korrektur der induktiven Kopplungseffekte für hoch leitfähige, aber schwach polarisierbare Materialien im Untergrund, kaum möglich sind. Die Analyse verschiedener Arten von Elektrodenkonfigurationen zeigte, dass die weit verbreiteten Alpha-Elektrodenkonfigurationen bei Verwendung eines fächerförmigen Kabellayouts einen viel höheren ICS aufweisen als andere Arten von Elektrodenkonfigurationen. Anhand einer synthetischen Modellierungsstudie mit einem fächerförmigen Kabellayout konnten zuverlässige Inversionsergebnisse ohne Datenkorrektur für induktive Kopplung erzielt werden, wenn Messungen mit hohen ICS-Werten vor der Inversion herausgefiltert wurden. Schließlich wurde der neuartige Filterungsansatz mit tatsächlichen sEIT-Messungen getestet. Die EIT-Inversionsergebnisse auf der Grundlage der gefilterten Daten stimmten gut mit den Inversionsergebnissen überein, bei denen die Daten um die induktive Kopplung korrigiert wurden, und zeigten auch eine gute spektrale Konsistenz. Es wurde festgestellt, dass es möglich ist, zuverlässige Inversionsergebnisse ohne Datenkorrektur für induktive Kopplung zu erzielen, wenn ein fächerförmiges Layout und Konfigurationen mit ausreichend geringen induktiven ICS-Wertenverwendet werden.

In einem dritten und letzten Schritt wurde ein Ansatz zur Abschätzung von Messfehlern aufgrund von kapazitiver Kopplung vorgeschlagen, der auf einer EIT-Modellierung unter Berücksichtigung von Kapazitäten und Leckströmen beruht. Es wurde festgestellt, dass der Imaginärteil der Impedanz aufgrund der kapazitiven Kopplung separat modelliert werden kann, ohne den Imaginärteil der elektrischen Leitfähigkeitsverteilung zu berücksichtigen. Anschließend wurde ein Verfahren zur Berechnung der kapazitiven Kopplungsstärke (CCS) für jede Elektrodenkonfiguration vorgeschlagen, die als das Verhältnis zwischen dem Imaginärteil der durch kapazitive Kopplung induzierten Impedanz und dem Imaginärteil der Impedanz aufgrund der elektrischen Leitfähigkeit des Bodens, definiert ist. Im ersten Schritt des Verfahrens wird die Verteilung des Realteils der elektrischen Leitfähigkeit bestimmt. Die so erhaltene 2D-Verteilung wurde auf ein 3D-Modell abgebildet und die Gesamtkapazität zwischen Kabelschirm und Erde wurde entlang der Kabel verteilt, indem die Kapazitäten an den entsprechenden Knoten im 3D-Vorwärtsmodell integriert wurden. Anschließend wurde eine Vorwärtsmodellierung mit dem Realteil der elektrischen Leitfähigkeitsverteilung, den integrierten Kapazitäten und den gemessenen Ableitströmen durchgeführt, um den Imaginärteil der durch die kapazitive Kopplung induzierten Impedanz zu erhalten. Schließlich wurden die CCS-Werte für alle betrachteten Messungen berechnet, wobei davon ausgegangen wurde, dass alle anderen Fehlerquellen vernachlässigbar sind. Es wurde festgestellt, dass Messungen mit großen normalisierten Leckströmen eher hohe CCS-Werte aufweisen. Schließlich wurden Messungen mit niedrigen CCS-Werten für die Inversion ausgewählt, und die Ergebnisse wurden mit Inversionsergebnissen verglichen, die mit einer so genannten vollständigen Elektrodenkonfiguration erzielt wurden. Die Inversionsergebnisse mit CCS-gefilterten Konfigurationen zeigten eine gute spektrale Konsistenz ohne Korrektur für kapazitive Kopplung. Es wurde festgestellt, dass die Filterung auf der Grundlage von CCS vielversprechend ist und ein großes Potenzial hat, konsistente und zuverlässige sEIT-Bildgebungsergebnisse über einen breiten Fre-

quenzbereich bis hin zum kHz-Frequenzbereich zu erzielen.

Insgesamt liefert diese Arbeit einen wichtigen Beitrag zur Etablierung der sEIT-Methode zur genauen Bildgebung der komplexen elektrischen Leitfähigkeitsverteilung im Untergrund im Frequenzbereich von mHz bis kHz auf der Feldskala. Es wurde ein neuer umfassender komplexer Inversionsansatz vorgeschlagen, der eine genaue Inversion von sEIT-Feldmessungen mit großen Phasenwinkeln ermöglicht. Der Vergleich dieses neuen Ansatzes mit anderen Strategien bestätigt die Eignung vereinfachter Strategien für die Inversion von sEIT-Messungen mit kleinen Phasenwinkeln. Es wurden Datenfilter zur Behandlung von EM-Kopplungseffekten bei breitbandigen sEIT-Messungen vorgeschlagen. Mit Hilfe der entwickelten Filteransätze konnten zuverlässige Inversionsergebnisse in einem breiten Frequenzbereich bis zu kHz ohne Korrektur der EM-Kopplung erzielt werden.

Contents

Declaration of authorship i

Acknowledgements iii

Abstract v

Zusammenfassung ix

Contents xiii

List of figures xvii

List of tables xxi

List of abbreviations xxiii

List of symbols xxv

1 Introduction 1

1.1 Motivation 1

1.2 Inversion of sEIT measurements 3

1.3 Electromagnetic (EM) coupling effects in sEIT 5

1.4 Objectives and outline of thesis 8

2 Theory and background 11

2.1 Fundamentals of sEIT 11

2.1.1 Spectral induced polarization (SIP) measurements 11

2.1.2 Spectral electrical impedance tomography (sEIT) 14

2.2 Forward modelling 17

2.3 Calculation of sensitivity 18

2.4 General formulation of the inverse problem 19
    2.4.1 Basic formulation 19
    2.4.2 Determination of the regularization parameter 21
    2.4.3 Line search 22
    2.4.4 Inversion workflow 23
    2.4.5 Model appraisal 24
2.5 Inversion strategies for EIT measurements 25
    2.5.1 Direct complex inversion (CVI) 26
    2.5.2 Two-step real-valued inversion (RVI) 26
    2.5.3 Alternate inversion (ALT) 27
2.6 Field measurements and used EIT instrumentation 28

3 Comparison of different inversion strategies for EIT measurements 31
3.1 Introduction 31
3.2 Materials and methods 32
    3.2.1 Improved complex inversion (CVI+) 32
    3.2.2 Synthetic modelling study 34
3.3 Results and discussion 35
    3.3.1 Results for Model-1 (small phase angle) 35
    3.3.2 Results for Model-2 (large phase angle) 38
    3.3.3 Discussion of cross-sensitivity 40
    3.3.4 Inversion results for field measurements 43
3.4 Conclusions 46

4 Experimental design to reduce inductive coupling in sEIT measurements 49
4.1 Introduction 49
4.2 Materials and methods 50
    4.2.1 Inductive coupling strength (ICS) 50
    4.2.2 Cable layouts 51
    4.2.3 Synthetic modelling experiment 53
    4.2.4 Analysis of Lozollo dataset 54
4.3 Results and discussion 55
    4.3.1 Evaluation of ICS for fan-shaped layout 55
    4.3.2 Evaluation of ICS for parallel cable layout 60
    4.3.3 Synthetic model study 65

4.3.4 Field example 66
4.4 Conclusions 70

5 Reduction of capacitive coupling in broadband sEIT measurements 71
5.1 Introduction 71
5.2 Materials and methods 72
5.2.1 Conceptual model 72
5.2.2 Normalized leakage current and the total capacitance 73
5.2.3 Decoupling of capacitive coupling 74
5.2.4 Capacitive coupling strength 77
5.2.5 Field measurements 78
5.3 Results and discussion 78
5.3.1 Total capacitance and leakage current 78
5.3.2 Evaluation of CCS 80
5.3.3 Inversion results of sEIT measurements 84
5.4 Conclusions 86

6 Conclusions and outlook 89
6.1 Conclusions 89
6.2 Outlook 93
6.2.1 Inversion 93
6.2.2 EM coupling reduction 98

References 103

List of figures

2.1 Schematic plots showing laboratory four-point SIP measurement and measured time series. 12

2.2 Schematic illustration of a sEIT measurement setup at the field scale. . . . 15

2.3 Three types of arrangement for a four-pole array. 15

2.4 A typical L-curve and its curvature. 21

2.5 Inversion workflow. 24

2.6 A typical eigenvalue spectrum with the relative eigenvalue range (RER) and the null space indicated. 25

2.7 Schematic representation of a fan-shaped survey layout. 29

2.8 The EIT40 measurement system and its block diagram. 30

3.1 Total objective function value Φ as a function of step lengths τ_A and τ_P for the logarithmic amplitude and phase angle of the electrical conductivity. . 33

3.2 Amplitude and phase of two subsurface models used in the synthetic modelling study. 35

3.3 Inversion results for electrical conductivity amplitude and phase of Model-1. 36

3.4 Inversion results for electrical conductivity amplitude and phase of Model-2. 39

3.5 Pseudo-section of the amplitude of the modelled apparent complex conductivity using Model-2. 40

3.6 Eigenvalue spectrum of Model-1 and Model-2. 42

3.7 Model updates calculated using different Jacobian. 43

3.8 Error estimation for the Lozzolo dataset. 44

3.9 Inversion results obtained by different strategies for the Lozzolo dataset. . 44

3.10 Inversion results obtained by different strategies for the Lozzolo dataset. . 46

4.1 Layout of two straight grounded wires connected to the system at position O in a horizontal plane. 52

4.2 Geometry of parallel cables and cross-section of multicore cable. 53

4.3 Subsurface model used in the synthetic modelling experiments. 53

4.4 Number of electrode configurations below a given ICS value for fan-shaped layout. 56

4.5 ICS values of the rank 1596 configuration for different subsurface conductivity magnitude and phase angle for the fan-shaped cable layout. 57

4.6 Number of electrode configurations below a given ICS value for α, β and *gamma* type configurations for Model-2 using a fan-shaped layout. 58

4.7 Number of configurations with ICS below 5 per cent for a fan-shaped layout with different separation between the EIT system and the survey line and different electrode spacings. 59

4.8 Number of electrode configurations below a given ICS value for parallel cable layout for two subsurface models. 60

4.9 Number of configurations below a given ICS value for configurations with separated transmitter and receiver cables for Model-2. 61

4.10 Number of configurations with ICS below 5 per cent for the parallel cable layout as a function of cable separations. 62

4.11 Schematic illustration showing the separation of the mutual inductance in several parts for configurations with wires for current and potential measurements in separate cables. 63

4.12 Contribution of horizontal and vertical cable segments (Mh and Mv) on mutual inductance M and inductive coupling strength ICS as a function of cable separation for three representative electrode configurations. 64

4.13 Inversion results for synthetic datasets: DD, DD-C, ICS5, ICS5-C. 66

4.14 Resolution of configuration dipole–dipole and 5 per cent ICS-filtered arrays. 66

4.15 Inversion results for field datasets: EZ, EZ-C, ICS5, ICS5-C. 67

4.16 Number of electrode configurations below a given ICS value for the field measurement configurations. 68

4.17 Resolution of EZ and ICS5 arrays. 69

4.18 Phase angle and imaginary part of complex impedance for four different datasets. 69

5.1 Schematic illustrating capacitive coupling between ground and cable shield. 73

5.2 Workflow to calculate the capacitive coupling strength (CCS). 78

5.3 (a) Relationship between the mean value of recorded voltages U_p and the corresponding leakage current I_L for all excitations at 1950 Hz and (b) estimated total capacitances as a function of frequency. 79

5.4 (a) Relationship between real part of the injected current I_1 and the real part of $-I_2$ at 1950 Hz and (b) the relationship between the real and imaginary part of the normalized leakage current at 1950 Hz. 80

5.5 (a) 2D inversion result for the real part of the electrical conductivity; (b) 3D conductivity model with integrated capacitances (black dots). 81

5.6 (a) Percentage of measurements with CCS $> 50\%$ as a function of the absolute normalized leakage current for the 22 selected excitations and (b) number of electrode configurations below a given CCS value in the remaining 5288 measurements after filtering. 82

5.7 Spectra of the imaginary part of the impedance for different datasets before and after correction. 83

5.8 Inversion results for the imaginary part of the electrical conductivity for the following datasets. 85

5.9 Resolution of EZ, CCS5, and CCS15 datasets. 86

6.1 (a) Development of the normalized data misfit, and (b) the model roughness during ERT inversion using different data types. 95

List of tables

3.1 Data weighting and the final regularization factors for different inversion strategies in the inversion of the phase angle of Model-1. 37

3.2 Data weighting and the final regularization factors for different inversion strategies in the inversion of the phase angle of Model-2. 40

4.1 Mutual inductance, geometric factor and ICS values for three selected electrode configurations 56

List of abbreviations

ALT	Alternate inversion strategy
CCS	Capacitive coupling strength
CVI	Complex-valued inversion strategy
CVI+	Improved complex inversion strategy
EIT	Electrical impedance tomography
EM	Electromagnetic
ERT	Electrical resistivity tomography
FEM	Finite element method
ICS	Inductive coupling strength
RVI	Two-step real-valued inversion strategy
sEIT	Spectral electrical impedance tomography
SIP	Spectral induced polarization

List of symbols

α	Alpha type electrode configuration
β	Beta type electrode configuration
γ	Gamma type electrode configuration
δ	Dirac delta function
$\boldsymbol{\Delta m}$	Model update
η	Eddy current constant
λ	Regularization factor
μ	Magnetic permeability
ρ^*	Complex electrical resistivity
ρ'	Real part of complex electrical resistivity
σ^*	Complex electrical conductivity
σ'	Real part of complex electrical conductivity
σ''	Imaginary part of complex electrical conductivity
σ_{bulk}	Bulk electrical conductivity
σ^*_{surf}	Surface electrical conductivity
σ'_{surf}	Real part of surface electrical conductivity
σ''_{surf}	Imaginary part of surface electrical conductivity

σ_∞	High frequency conductivity
σ_0	Low frequency conductivity
τ_t	Relaxation time
τ	Step length
τ_{opt}	Optimal step length
τ_A	Step length for the logarithm of the amplitude of conductivity
τ_P	Step length for the phase angle
ϕ^*	Complex electrical potential
$\tilde{\phi}^*$	Fourier transformed complex potential
φ	Phase angle
φ_a	Measured phase angle
φ_i	Phase angle of applied alternating current
φ_u	Phase angle of measured complex voltage
Φ	Total objective function
Φ_d	Data misfit
Φ_m	Model roughness
χ^2	Normalized data misfit
Ψ_d	logarithm of data misfit Φ_d
Ψ_m	logarithm of model roughness Φ_m
ω	Angular frequency
A	Surface area of column
c	Relaxation exponent

C_T	Total capacitance
$\boldsymbol{d}$	Data vector
d_i	i^{th} data
$\boldsymbol{e}$	Data error
e_i	Error for i^{th} data
f	Frequency
$f_i(\boldsymbol{m})$	The i^{th} modelled response for a given model $\boldsymbol{m}$
$\boldsymbol{G}$	Jacobian matrix
i	Imaginary unit
I	Electric current
I_i	Current through capacitance
I_L	Leakage current
I_s	Symmetric current
I_1	Current through the positive current electrode
I_2	Current through the negative current electrode
I^*	Complex electric current
k	Wavenumber
K	Geometric factor
$\boldsymbol{L}$	Damping matrix
$\boldsymbol{m}$	Model vector
m_c	Chargeability
m_i	i^{th} model parameter

M	Mutual inductance
nLS	Normalized leakage current
$P(r)$	Mutual impedance
$Q(r)$	Response due to soil
r	Distance
$rErr$	Relative error in the approximated real part impedance
R	Resistance
U^*	Complex voltage
U'	Real part of complex voltage
U''_c	Imaginary part voltage due to capacitive coupling
U_p	Voltage measured at electrodes relative to system ground
U''_s	Imaginary part voltage due to soil polarization
$\boldsymbol{W}_d$	Data weighting matrix
$\boldsymbol{W}_m$	Model regularization matrix
$\boldsymbol{Y}^*$	Discrete complex conductivity matrix
$\boldsymbol{Y}''_c$	Diagonal matrix with integrated capacitances
$\boldsymbol{Y}'_s$	Real part of discrete complex conductivity matrix
$\boldsymbol{Y}''_s$	Imaginary part of discrete complex conductivity matrix
Z^*	Complex impedance
Z_0	Noise-free complex impedance
Z'_0	Real part of noise-free complex impedance
Z''_0	Imaginary part of noise-free complex impedance

Z'_{app}	Approximated real part impedance
Z''_c	Imaginary part impedance due to capacitive coupling
Z_m	Measured impedance

Chapter 1

Introduction

1.1 Motivation

Subsurface characterization is a critical step in many soil and hydrogeological investigations. The bulk electrical conductivity has long been used as a key parameter for characterizing subsurface materials, such as investigation of bedrock topography (*Griffiths and Barker*, 1993) and aquifer architecture (*Rayner et al.*, 2007; *Schütze et al.*, 2012), mapping the hydrostratigraphy (*Clifford and Binley*, 2010) and the groundwater resources (*Auken et al.*, 2006), and characterizing contaminants (*Chambers et al.*, 2010). The bulk electrical conductivity reflects the ability to conduct electric current. For typical porous geomaterials, such as soil and rock, the bulk electrical conductivity refers to the electrolytic conduction in the pore space given that the solid phase is non-conducting. Dating back to the early 1940s, the bulk electrical conductivity has been linked to the porosity of porous materials (*Archie*, 1942). In recent decades, there has been a significant increase in the application of electrical conductivity imaging techniques to better understand and characterize subsurface conditions (*Park*, 1998; *Loke et al.*, 2013; *Dimech et al.*, 2022). While the bulk electrical conductivity provides useful information, it has limitations in terms of capturing the full complexity of subsurface materials. For example, it is difficult to differentiate clayey soil and saline soil solely based on the bulk electrical conductivity, because they both lead to a high electrical conductivity. Recognizing this, complex electrical conductivity measurements have emerged as a more advanced approach (*Luo and Zhang*, 1998).

The complex conductivity can be measured by applying alternating electric current at a certain frequency and is usually measured over a broad frequency range from mHz to kHz (referred to as spectral induced polarization). The complex electrical conductivity consists of a real and imaginary part. The real part of the electrical conductivity is mainly controlled by the bulk electrical conductivity, while the imaginary part is associated with polarization process within the material when applying an alternating electric current (*Revil and Florsch*, 2010). The dominant polarization mechanisms in the mHz to kHz frequency range are Maxwell-Wagner polarization in the frequency range above 1 kHz and polarization associated with the electrical double layer (EDL) for frequencies below 1 kHz (*Kemna et al.*, 2012). The behaviour of the frequency dependent imaginary part of the electrical conductivity can be quite different depending on the physical and chemical properties of the investigated materials, including particle/pore size (*Koch et al.*, 2011; *Revil et al.*, 2012), moisture content (*Ulrich and Slater*, 2004), temperature (*Bairlein et al.*, 2016), ionic concentration (*Izumoto et al.*, 2020), and pH (*Skold et al.*, 2011). Often, the frequency-dependent imaginary part of the electrical conductivity displays a distinct peak response. This peak frequency is closely related to the dominant polarization mechanism and the associated length scale (*Mellage et al.*, 2018a; *Tsukanov and Schwartz*, 2021), and can be linked to other properties of interest, such as the hydraulic conductivity (*Slater and Lesmes*, 2002; *Binley et al.*, 2005). Laboratory studies over the past decades have shown that this peak frequency can vary in a broad frequency range from mHz to kHz for different materials (*Aal et al.*, 2006; *Mellage et al.*, 2018a,b; *Gao et al.*, 2019). Therefore, broadband measurements of the complex electrical conductivity are desirable to characterize the full complexity of the electrical response of the investigated materials.

Given the promising laboratory results, there is an increasing interest in obtaining the distribution of the complex electrical conductivity at the field scale using spectral electrical impedance tomography (sEIT) technology, particularly in the case of environmental and hydrogeophysical applications such as contaminated site characterization (*Flores Orozco et al.*, 2012a), biogeochemical investigations (*Williams et al.*, 2009; *Flores Orozco et al.*, 2011), hydraulic conductivity determination (*Attwa and Günther*, 2013) and imaging of the plant root zone (*Weigand and Kemna*, 2019). To obtain reliable imaging results over a broad frequency range, a proper inversion strategy as well as accurate measurements are both important. However, there are still questions and challenges associated with sEIT data inversion and acquisition that need to be addressed before sEIT will gain widespread acceptance, which will be elaborated in the following sections.

1.2 Inversion of sEIT measurements

Inversion of sEIT measurements is usually carried out frequency by frequency, although there are algorithms that consider a direct inversion of multi-frequency data (*Loke et al.*, 2006; *Günther and Martin*, 2016). Different from the inversion of electrical resistivity tomography (ERT) data where only the amplitude of the measurements is considered, the inversion of single frequency EIT data deals with complex measurements involving the amplitude and phase (or real and imaginary parts) of the measured impedances. Early work on the inversion of time-domain induced polarization (TDIP) data linearized the chargeability in the inverse problem and used a formulation in the real number domain (*Oldenburg and Li*, 1994; *Beard et al.*, 1996). In the frequency domain, complex-valued forward modeling (*Weller et al.*, 1996) enabled a complex inversion (*Weller et al.*, 1997). However, *Weller et al.* (1997) inverted the complex data using a simultaneous iterative reconstruction technique, which was developed for linear problems and thus not fully suitable for the nonlinear geoelectrical inverse problem. Based on the non-linear Gauss-Newton method that is widely adopted in the inversion of ERT data (*Sasaki*, 1992; *LaBrecque et al.*, 1996; *Loke and Barker*, 1996), a direct complex inversion strategy with the data and model in complex form can be formulated. For this case, *Kemna* (2000) showed that the inversion was dominated by the real part of the data and model because the real part is usually several orders of magnitude larger than the imaginary part. Therefore, an additional inversion step called the final phase improvement (FPI) was proposed by *Kemna* (2000) to separately refine the phase model.

Recent developments in the inversion of EIT data have tried to simplify and separate the inversion of the real and imaginary part to a larger extent. For example, *Martin and Günther* (2013) adopted a two-step real-valued inversion approach where the amplitude was inverted first in the real number domain (i.e. ERT inversion), and the imaginary part of the resistivity was then separately inverted using the final real-valued Jacobian from the first step. The strategy proposed by *Martin and Günther* (2013) can be referred to as a two-step inversion, which ignores the complex nature in the forward modelling and imaginary part of the complex Jacobian. These simplifications assume that only small phase angles are present in the subsurface. Although this assumption is often justified in near surface applications, large phase angles were also occasionally reported. For example, *Kulenkampff and Yaramanci* (1993) showed that the measured phase angle for rock salt can be extremely large with phase values up to 1000 mrad. Recently, *Peruzzo et al.* (2021)

also presented large phase angles above 500 mrad associated with the plant root system of crops.

Johnson and Thomle (2018) proposed a decoupled strategy for the inversion of EIT measurements, which is especially beneficial for large-scale problems because the complex forward modelling was decomposed and can be done in the real number domain. In particular, the imaginary potential distribution was obtained in the real number domain after the real part of the potential was solved. In the case of small phase angles, their approach becomes again a two-step inversion similar to *Kemna* (2000) and *Martin and Günther* (2013). For large phase angles, this approach alternately inverts for the real and imaginary part of the electrical conductivity using the decoupled forward modelling and approximated sensitivity. Although this approach considers the complex coupling in the forward modelling, it does not consider the imaginary part of the complex Jacobian matrix in the inversion. Unfortunately, the inversion strategy proposed by *Johnson and Thomle* (2018) was only tested with models showing small phase values. It remains to be seen how this alternate inversion strategy performs and whether the cross-sensitivity can be neglected in the case of models with large phase values.

Based on these previous studies, the inversion approaches for EIT data can be divided into three strategies. The first strategy is the direct complex inversion where the data and model are complex numbers. The second strategy is a two-step inversion approach that separately inverts the real and imaginary parts of the considered data while ignoring their complex nature. The third strategy is an alternate inversion approach that updates the real and imaginary parts of the considered model alternately in each iteration and is specially designed to deal with large phase angles. Although the drawbacks of the first strategy have been pointed out before (*Kemna*, 2000; *Günther and Martin*, 2016), it remains to be explained in detail how the real part of the data and model dominate the inversion. The second and the third strategies consider the separated treatment of the real and imaginary part of the complex data and model in terms of data weighting and model regularization to some extent, but they do not fully consider the complex nature of EIT data inversion. The cross-sensitivity has always been neglected so far, but this simplification needs further investigation for the case that the measurements show large phase angles. The theoretically ideal case for EIT inversion should consider simultaneously the coupling between real and imaginary parts of the complex data and model, and the separated treatment in terms of data weighting and model regularization.

Such an inversion approach has not been formulated and implemented yet.

1.3 Electromagnetic (EM) coupling effects in sEIT

EM coupling effects including both inductive and capacitive coupling effects have long been an essential problem in obtaining accurate and broadband sEIT measurements. Inductive coupling in sEIT measurements includes the cable-to-cable effect and the earth-return inductance (*Sunde*, 1968). The cable-to-cable effect refers to the phenomenon where the alternating current in an electrical wire generates a magnetic field around the wire. This magnetic field, in turn, induces a voltage in the wires for voltage measurements. The earth-return inductance is associated with the secondary magnetic field induced by the current flowing through the earth that can also induce voltages in the wires for voltage measurements. Ideally, both inductive coupling effects should be considered in forward modelling, which requires that the distribution of the subsurface electrical conductivity is known (*Ingeman-Nielsen and Baumgartner*, 2006a,b). If this is not the case, the full consideration of inductive coupling requites the consideration within the 3D EIT inversion (*Commer et al.*, 2011), which however is computationally expensive. In the case of small scale applications, only the cable-to-cable effect needs to be considered *Wait* (1984). Early work on EM coupling removal focused on the inductive coupling. Correction methods for inductive coupling based on the constant phase assumption (*Coggon*, 1984) or the Cole-Cole model (*Pelton et al.*, 1978) were of limited use because the IP and EM effects are in general more complicated than the assumed models. In case of the cable-to-cable effect, the amount of inductive coupling depends on the measurement frequency and the mutual inductance between the cables used for current injection and potential measurements (*Sunde*, 1968). Early work to remove inductive coupling based on the mutual inductance for large-scale applications (*Wait and Gruszka*, 1986; *Routh and Oldenburg*, 2001) showed promising results, but they were limited to very low frequencies around 1 Hz because of the use of long cables. In the case of small scale applications, correction methods to remove inductive coupling from sEIT measurements have been proposed and applied to a broader frequency range (*Zhao et al.*, 2013, 2015). The use of these correction methods provided consistent inversion results up to 1 kHz for borehole (*Kelter et al.*, 2018) and surface sEIT measurements (*Zimmermann et al.*, 2019). These correction methods require estimates of the mutual inductance between cables used for current injection and potential measurements. If the geometry of the cable layout is known, this mutual inductance can be calculated numerically. However, it is challenging to accurately calculate the mutual inductance for multicore cables because the wires are close together and often twisted (*Zhao et al.*, 2015). In this case, the mutual inductance can be estimated using calibration measurements (*Zhao et al.*, 2015; *Kelter et al.*, 2018; *Weigand et al.*, 2022). Despite the initial promising results reported in *Zhao et al.* (2013, 2015) and *Zimmermann et al.* (2019), inductive coupling and the proposed correction methods deserve a more detailed investigation. For example, it is expected that some measurement configurations are strongly affected by inductive coupling, and it may be desirable to not correct but instead remove such configurations before inversion. In addition, it is interesting to explore whether a careful selection of electrode configurations for sEIT measurements would allow to obtain reliable inversion results without the need for correction of inductive coupling.

Capacitive coupling in sEIT measurement usually refers to the leakage of electric current through possible capacitances wherever a potential difference exists. Using a simple parallel electric circuit model with an impedance and capacitance representing the path for leakage current, the behaviour of capacitive coupling as a function of the subsurface electrical properties can be well explained. In the case of conductive soil, the electric current preferably flows through the ground impedance rather than through the capacitance, resulting in a small leakage current and minor capacitive coupling. In the case of a resistive soil, the leakage current is large and the capacitive coupling dominates the data quality. Capacitive coupling in sEIT measurements includes mainly three types of sources: coupling between the cables, coupling between the ground and electrodes and coupling between the ground and cables (*Radić*, 2004; *Dahlin and Leroux*, 2012; *Zhao et al.*, 2013). The first type of capacitive coupling is usually the most important one when using non-shielded multicore cables. *Dahlin and Leroux* (2012) proposed a parallel cable layout separating the current injection and potential measurement in different cable bundles to reduce this type of capacitive coupling in TDIP measurements. Alternatively, the capacitive coupling between cables can be significantly reduced by using shielded cables (*Flores Orozco*, 2012; *Zhao*, 2017; *Flores Orozco et al.*, 2021). A remaining source of capacitive coupling when using shielded cables is the capacitance between the inner wire and the shield, which can be eliminated by using so-called active electrodes (i.e. amplifiers mounted at the electrodes) as in *Zimmermann et al.* (2010). The second type of capacitive coupling between the ground and electrodes is associated with the contact impedance and the internal electronics in the amplifier (i.e. the input capacitance). *Kelter et al.* (2015) and *Huisman et al.* (2016) have presented methods to estimate the contact impedance and correct the induced error at the field and laboratory scale, respectively. With the use of the so-called active electrodes (i.e. amplifier mounted at the electrodes), the input capacitance for voltage measurement can be largely reduced to 5 pF (*Zimmermann et al.*, 2008a), which can be further corrected by implementing the 5 pF capacitance at the electrodes in the forward modelling (*Zimmermann et al.*, 2019). With all these advanced improvements, the first two types of capacitive coupling can be suppressed to a large extent. The remaining main source of capacitive coupling then becomes the capacitive coupling between the cable shield and the ground (*Zhao et al.*, 2013, 2015; *Zimmermann et al.*, 2019).

To deal with the capacitive coupling between the cable shield and the ground (or the materials of interest), a straightforward strategy is to put the cables in the air in the case of a conventional surface survey, for example by using Styrofoam to elevate the cables from the ground (*Weigand et al.*, 2022). For monitoring purposes and relatively small survey layouts (*Weigand et al.*, 2022), it is worth dealing with this source of capacitive coupling in this way but it does require extra field handling of the cables. However, it is not always possible to reduce capacitive coupling by increasing the separation between cables and the material of interest, for example in the case of borehole EIT measurements where the contact between cable and ground water cannot be avoided. For such cases, *Zhao et al.* (2013) proposed to consider capacitive coupling in the finite element forward modelling during inversion by integrating capacitances at nodes that represent the cable position. In the case of small leakage currents, the proposed correction method improved the results up to kHz for single-borehole sEIT measurements (*Zhao et al.*, 2013) and cross-hole sEIT measurements *Zhao et al.* (2015). To consider large leakage current, *Zimmermann et al.* (2019) abandoned the widely used assumption of a symmetric current injection. Instead, they considered both the integrated capacitances and the actual measured currents in the forward modelling for surface sEIT measurements. With the use of this advanced modelling approach, *Zimmermann et al.* (2019) improved the phase results at 71 Hz substantially. However, the corrections were only partly successful for higher frequencies. In addition, the results presented in *Zimmermann et al.* (2019) were limited to a small set of electrode configurations from the so-called complete configuration (*Xu and Noel*, 1993), and capacitive coupling associated with other possible electrode configurations was not investigated. The question here is similar to that in the case of inductive coupling. Some measurement configurations may be strongly affected by capacitive coupling, and it may be desirable to remove instead of correct such measurements before inversion. Furthermore, it is again interesting to investigate whether a careful selection of electrode configurations for sEIT measurements would allow to obtain reliable inversion results without the need for correction of capacitive coupling.

1.4 Objectives and outline of thesis

The brief overview of previous work highlighted the capability of SIP measurements to provide a comprehensive characterization of subsurface materials and reviewed the continuous improvements in the application of sEIT at the field scale. Considering the identified knowledge gaps in both inversion and the consideration of EM coupling, the overall objective of this thesis is to enhance the applicability of sEIT technology at the field scale to facilitate accurate and comprehensive subsurface imaging.

To address this overall objective, three sub-objectives have been defined. The first sub-objective is to develop an inversion strategy that can fully account for the intrinsic complex nature of EIT data while considering a separated treatment in terms of data weighting and model regularization and to compare this newly formulated strategy with other available inversion strategies. The second sub-objective is to investigate whether a careful selection of electrode configurations for sEIT measurements would allow to obtain reliable broadband inversion results without the need for correction of inductive coupling and to better understand the inductive coupling in terms of different cable layouts, electrode configurations and soil properties. Similar to the second sub-objective dealing with inductive coupling, the third sub-objective is to explore the possibility to obtain reliable inversion results by selecting electrode configurations that do not require correction of capacitive coupling. To achieve this, it is important to investigate in detail the modelling approach considering integrated capacitances and leakage currents, and to develop a strategy to model the impedances induced by capacitive coupling.

The remainder of this thesis is organized as follows. In Chapter 2, the background and theory of sEIT will be provided. First, the basics of sEIT technology will be introduced, including the electrical conductivity of materials, measurement methods at both laboratory and field scales, as well as a description of the EIT measurement system used in this thesis. Then, the forward modelling problem in sEIT will be described. This chapter will conclude with a detailed description of the inverse problem and the existing inversion strategies.

In Chapter 3, a novel inversion strategy that can fully account for the intrinsic complex nature of sEIT data inversion will be introduced. Then, this newly formulated inversion strategy will be compared with the other inversion strategies described in Chapter 2. Synthetic modelling studies will be carried out for the comparison of different inversion strategies and models with small and large phase angles will be used to investigate the role of the imaginary part of the complex sensitivity in the inversion of EIT measurements.

Chapter 4 deals with inductive coupling in sEIT measurements. First, a novel measure to assess the inductive coupling strength of a given electrode and cable configuration will be proposed. The proposed index will then be used as a filter to select data with limited inductive coupling. The inductive coupling strength of fan-shaped and parallel cable layouts and different electrode configurations will be evaluated for different homogeneous subsurface models. A synthetic model study will first be used to illustrate the usefulness of the proposed filter. In a final step, field measurements with low inductive coupling strength will be selected for final inversion without correction for inductive coupling and the results will be compared to the inversion results obtained using established correction procedures for inductive coupling.

Chapter 5 deals with capacitive coupling in sEIT measurements. A new method will first be presented to model the imaginary part of the impedance induced by the capacitive coupling before actual inversion of the data. Then, an index to quantify the capacitive coupling strength will be proposed and used as a data filter to remove measurements that are strongly affected by capacitive coupling. The capacitive coupling strength of all possible electrode configurations will then be examined assuming that only capacitive coupling needs to be considered and that other sources of measurement error are of secondary importance. In a final step, electrode configurations with low capacitive coupling strength will be selected for inversion of sEIT data and the results will be compared to standard inversion results.

This thesis concludes with Chapter 6, in which a synthesis of the findings and achievements in this thesis will be provided and possible directions for further research will be discussed.

Chapter 2

Theory and background

In this chapter, essential background information related to the sEIT method will be provided. First, laboratory SIP measurements and the concept of complex electrical conductivity will be introduced, including the measurement method and polarization mechanisms. This will be followed by the description of the field measurement method (i.e. sEIT) and the associated measurement procedures and electrode configurations. After this, the forward modelling problem and the calculation of the sensitivity will be described. This will be followed by a detailed description of the general inverse formulation in electrical tomography. Implementations of methods to determine the important parameters in the general inversion approach, such as the regularization factor and the step length, will be illustrated in detail. The inversion workflow will be summarized and tools to evaluate the inversion results will be introduced. Based on the general inverse formulation, strategies for EIT data inversion will be reviewed. At the end of this chapter, the field measurements as well as the measurement system used in this thesis will be introduced with a description of the key features that are important for the development of the ideas presented in this thesis.

2.1 Fundamentals of sEIT

2.1.1 Spectral induced polarization (SIP) measurements

Figure 2.1(a) shows a schematic illustration of a typical four-point laboratory SIP measurement. Alternating current I^* is applied to the sample through two electrodes at the top and bottom of the sample. Two other electrodes with a distance r are used to measure the potential difference U^*. The current and voltage are all measured in time domain as time series shown in Figure 2.1(b) and then converted to the frequency domain as complex numbers using a Fourier transformation (*Zimmermann et al.*, 2008b). The complex impedance Z^* between the two potential electrodes can be calculated using:

$$Z^*(\omega) = \frac{U^*(\omega)}{I^*(\omega)} = \frac{|U^*|e^{i\varphi_u}}{|I^*|e^{i\varphi_i}} = |Z^*|e^{i(\varphi_u - \varphi_i)} \tag{2.1}$$

where $\omega = 2\pi f$ is the angular frequency with f being the measurement frequency (i.e. frequency of the applied alternating current), i is the imaginary unit, φ_u and φ_i are the phase angles for the measured voltage and applied current. Considering the exponential form of the complex numbers in Equation 2.1, it can be easily seen that the phase shift between the injected current and the measured voltage shown in Figure 2.1(b) represents the phase angle of the complex impedance Z^*.

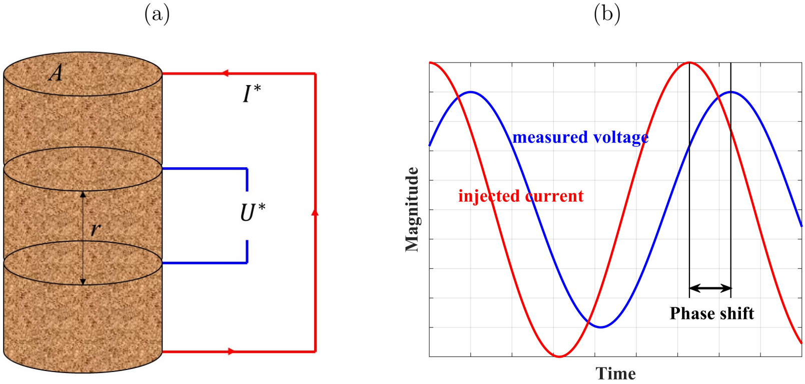

Figure 2.1: (a) Schematic plots showing laboratory four-point SIP measurement and (b) measured time series.

The complex electrical conductivity σ^* of the sample, which is the inverse of the complex resistivity ρ^* of the sample, can then be calculated using:

$$\sigma^* = \frac{1}{\rho^*} = \frac{1}{KZ^*} = \frac{r}{A}\frac{I^*}{U^*} \tag{2.2}$$

where $K = A/r$ is the geometric factor of the sample, and A is the surface area of the sample column. The complex electrical conductivity can be expressed either by the amplitude and phase angle or the real and the imaginary part:

$$\sigma^* = |\sigma^*|e^{i\varphi} = \sigma' + i\sigma'' \tag{2.3}$$

where $|\sigma^*|$ is the amplitude of complex electrical conductivity σ^*, φ is the phase angle, and σ' and σ'' are the real and the imaginary part of the electrical conductivity, respectively. Based on a parallel electric circuit model (*Marshall and Madden*, 1959; *Waxman and Smits*, 1968), the complex electrical conductivity can be described by the summation of two components (*Lesmes and Frye*, 2001):

$$\sigma^* = \sigma_{\text{bulk}} + \sigma^*_{\text{surf}}(\omega) = (\sigma_{\text{bulk}} + \sigma'_{\text{surf}}(\omega)) + i\sigma''_{\text{surf}}(\omega) \tag{2.4}$$

where σ_{bulk} is the frequency-independent bulk conductivity, and σ'_{surf} and σ''_{surf} are the real and imaginary parts of the complex surface conductivity σ^*_{surf}. The bulk electrical conductivity reflects the capacity to conduct electric currents. In the case of common porous geomaterials like soil and rock where the solid phase is non-conducting, the bulk electrical conductivity σ_{bulk} refers to the electrolytic conduction within the pore space. The real part of the complex surface conductivity σ'_{surf} refers to the conduction occurring at the surface or interface of the porous material and is frequency-dependent. In the low frequency range, the bulk conductivity is much larger than the real part of the complex surface conductivity.

The phase angle or the imaginary part of the complex electrical conductivity is controlled by the pore surface properties and related to the polarization (energy storage). In the presence of an external electric field, polarization refers to the phenomenon of induced electrical charge separation in dielectric materials. It can occur through different mechanisms depending on the frequency range (*Kemna et al.*, 2012). At lower frequencies, polarization is mainly attributed to the macroscopic movement of ions, which require time to reach equilibrium and thus contribute to polarization. The sources are usually referred to as grain polarization and membrane polarization (*Revil*, 2012). Grain polarization can be attributed to the movement and reorientation of ions within the electrical double layer (i.e. Stern layer and the diffuse layer) in the presence of an external electrical field, resulting in the separation of positive and negative charges (*Revil et al.*, 2012). Membrane polarization (*Marshall and Madden*, 1959) which is also closely related to electrical double layer arises from the different mobility of ions in the narrow parts of the pore space, such as pore throats. It occurs when movement of ions is restricted due to the geometry or surface properties of the pores. Maxwell-Wagner polarization (*Leroy et al.*, 2008), which is particularly prominent at higher frequencies above 1 kHz, refers to the phenomenon that occurs at the interfaces between materials with different electrical conductivity and permittivity. Regardless of the active polarization mechanisms, the frequency-dependent complex conductivity can often be described by the widely used Cole-Cole model (*Cole and Cole*, 1941):

$$\sigma^* = \sigma_\infty(1 - \frac{m_c}{1 + (i\omega\tau_t)^c}) \tag{2.5}$$

where $m_c = (\sigma_\infty - \sigma_0)/\sigma_\infty$ is the chargeability, σ_∞ and σ_0 are the high- and low-frequency conductivity respectively, ω is the angular frequency, τ_t is the relaxation time constant, and c is the relaxation exponent. Although there are limitations and uncertainties when using empirical models to describe SIP measurements (*Tarasov and Titov*, 2013), the calculated relaxation time from the Cole-Cole model has been shown to correlate with key hydrological properties, such as the hydraulic conductivity (*Slater and Lesmes*, 2002; *Attwa and Günther*, 2013).

2.1.2 Spectral electrical impedance tomography (sEIT)

sEIT is an extension of the widely applied electrical resistivity tomography (ERT) method, which measures only the amplitude of the impedance (resistance) using a direct electric current. In contrast, alternating current is applied in the sEIT method and the complex impedances can be measured in a broad frequency range from mHz to kHz. The measurement setup of sEIT at the field scale is also similar to ERT. A typical 2D survey with a multi-electrode setup is shown in Figure 2.2. A number of electrodes are placed along the survey line. Two electrodes are selected for current excitation and the remaining electrodes can be used for potential measurements. Similar to the laboratory SIP measurements, the potential difference between two arbitrary electrodes is considered, which is referred to as a four-point measurement configuration. A sequence of four-point measurements need to be acquired along the multi-electrode setup with different electrode separations. The movement of a four-point configuration along the survey line allows to detect lateral changes, whereas a larger electrode separation increases the sensing depth.

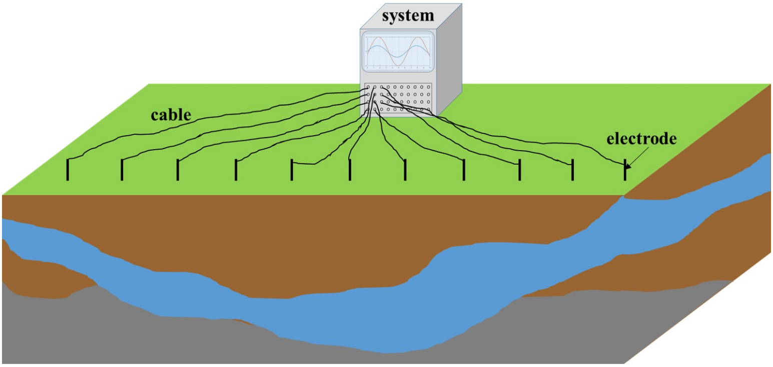

Figure 2.2: Schematic illustration of a sEIT measurement setup at the field scale.

The arrangement of the current and potential electrodes and the selection of measurement configurations is an important decision in any geoelectrical survey. There are many well-established conventional measurement schemes, such as the Wenner and dipole-dipole schemes (*Dahlin and Zhou*, 2004), which have been widely adopted for field data acquisition. In general, there are three types of electrode configurations: α, β, and γ configurations as shown in Figure 2.3 (*Carpenter and Habberjam*, 1956; *Loke et al.*, 2010). In the α type configuration, the potential electrodes are nested between the current electrodes. The β type configuration has separated current and potential dipoles. In the γ type configuration, current and potential electrodes are interleaved.

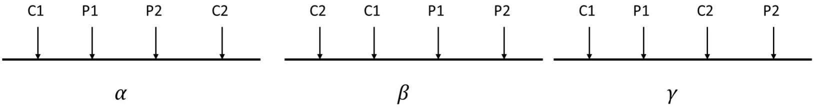

Figure 2.3: Three types of arrangement for a four-pole array (C1 and C2 are current poles, P1 and P2 are potential poles).

For a homogeneous subsurface model with a complex electrical conductivity σ^*, the measured complex impedance Z^* can be calculated using the geometric factor K, which depends on the position of the electrodes at the surface:

$$Z^* = \frac{1}{K\sigma^*} \tag{2.6}$$

$$K = \frac{2\pi}{\dfrac{1}{r_{C1P1}} - \dfrac{1}{r_{C2P1}} - \dfrac{1}{r_{C1P2}} + \dfrac{1}{r_{C2P2}}} \tag{2.7}$$

where r indicates the distance between different electrode pairs indicated by the suffixes. The geometric factor is usually considered as a good indicator of signal-to-noise ratio. Combining Equation 2.1 and 2.6, it can be seen that a high geometric factor results in small recorded voltage, and vice versa. In field measurements where noise is present, it is crucial to ensure that the measured voltage is significantly larger than the voltage error caused by noise. One possible strategy to achieve this is by increasing the injected current. However, there are practical limits to the amount of current that can be applied, depending on the equipment used. Configurations with low geometric factors are more likely to yield larger voltage measurements, and are thus preferred in geoelectrical surveys. However, it is important to note that the geometric factor is based on a homogeneous subsurface model with a uniform resistivity distribution but the real cases are mostly heterogeneous.

Electrode configurations of the α and β types are usually preferred in geoelectrical surveys, while the γ type is rarely used. In studies on optimized experimental design for geoelectrical surveys (*Wilkinson et al.*, 2006a; *Loke et al.*, 2010), the γ type configuration was completely discarded for several reasons. First of all, γ type configurations can be reconstructed by a combination of α and β configurations, and it is thus often argued that they do not provide additional information. Second, γ type configurations can produce negative apparent resistivities in certain circumstances (*Carpenter and Habberjam*, 1956), which can be problematic when the logarithm of apparent resistivity or conductivity is used as data in the inversion. Third, γ type configurations can lead to measurements with zero impedance. This is related to the potential field distribution that changes from positive to negative with a zero-potential point between the current electrodes. Beyond the current electrodes, the potential decreases from positive to zero with distance from the positive electrode, and it increases from negative to zero with distance from the negative electrode. This means that equipotential lines always traverse inside and outside the two current electrodes. Therefore, there is a high possibility of measuring a zero or near-zero potential difference with the use of the γ type configuration, which is very sensitive to noise in the voltage measurement. Restricting the range of considered geometric factors does not always avoid this problems. Despite these concerns, it has been shown that the γ type configuration has a deeper investigation depth (*Acworth*, 1981; *Szalai et al.*, 2020). In this thesis, γ type configurations are not discarded a priori, but careful selection will need to be used to ensure meaningful sEIT results.

2.2 Forward modelling

The forward problem in EIT involves solving the Poisson equation for a given complex electrical conductivity distribution and measurement configuration:

$$\nabla \cdot (\boldsymbol{\sigma}^* \nabla \boldsymbol{\phi}^*) = I(\delta(\boldsymbol{r} - \boldsymbol{r_{C1}}) - \delta(\boldsymbol{r} - \boldsymbol{r_{C2}})) \tag{2.8}$$

where $\boldsymbol{\sigma}^*$ is the complex conductivity of the medium, $\boldsymbol{\phi}^*$ is the complex potential, I is the electric current, and $\delta(\boldsymbol{r} - \boldsymbol{r_{C1}})$ is the Dirac delta function. The forward problem can be solved in 3D (*Li and Spitzer*, 2002) or in 2.5D (*Dey and Morrison*, 1979) assuming no variation along the direction perpendicular to the modelling plane. In the latter case, the forward and inverse Fourier cosine transforms are applied to solve Equation 2.8 in the wavenumber domain:

$$\tilde{\phi^*}(x,k,z) = 2\int_0^\infty \phi^*(x,y,z)cos(ky)dy \tag{2.9}$$

$$\phi^*(x,y,z) = \frac{1}{\pi}\int_0^\infty \tilde{\phi^*}(x,k,z)cos(ky)dk \tag{2.10}$$

where $\tilde{\phi}$ and k are the transformed complex potential and wavenumber, respectively. To solve Equation 2.10 accurately, the wavenumber k should be selected appropriately. Although optimized routines for the selection of wavenumbers have been proposed (*Xu et al.*, 2000; *Pidlisecky and Knight*, 2008), the method presented in *LaBrecque et al.* (1996) and Appendix C of *Kemna* (2000) were used in this thesis to determine the wavenumber. In particular, a characteristic wavenumber k_0 is first determined based on the length of electrode configuration and used to split the integral into two parts. The first integral from 0 to k_0 is calculated using a N_G-point Gaussian quadrature and the second integral above k_0 is calculated using a 4-point Laguerre-type formula. N_G is determined based on the length of the survey line and the electrode configuration.

In this thesis, the forward problem was solved using the finite element method (FEM) in a custom-made Matlab program extended from *Zimmermann* (2011). Neumann (no-flow) boundary conditions were applied to all domain boundaries and the subsurface boundaries were put sufficiently far away from the survey area of interest. The FEM grids were generated using Gmsh (*Geuzaine and Remacle*, 2009). The modelling grids were refined around the electrodes by using an element size of 1/10 of the electrode spacing and the element size gradually increased with increasing distance from the electrodes. For all grids, the accuracy of the forward modelling was tested using a homogeneous model with known electrical conductivity and the relative error was better than 1% for all measurement configurations considered in this thesis.

2.3 Calculation of sensitivity

The sensitivity is defined as the partial derivative of the data with respect to a model parameter. It quantifies the extent to which a change in a model element would affect the measurement. It can be easily calculated using the products from the forward modelling based on the reciprocity theorem (*Murai and Kagawa*, 1985; *Park and Van*, 1991). In the complex form, considering the complex electrical conductivity as model parameter and the complex impedances as data, the sensitivity can be expressed as:

$$\frac{\partial Z^*}{\partial \sigma^*} = -\int \frac{\nabla \phi_C^*}{I_C} \cdot \frac{\nabla \phi_P^*}{I_P} d\Omega \tag{2.11}$$

where $\boldsymbol{\phi}_C^*$ and $\boldsymbol{\phi}_P^*$ are the complex potential distribution induced by current excitation $\boldsymbol{I}_C$ and $\boldsymbol{I}_P$ at the transmitter (current poles) and the receiver (potential poles), respectively, $\boldsymbol{Z}^*$ is the complex impedance, and $d\Omega$ represents a small volume element. The sensitivity for the logarithm of the data and model can be derived using the chain rule:

$$\frac{\partial ln Z^*}{\partial ln \sigma^*} = \frac{\sigma^*}{Z^*} \frac{\partial Z^*}{\partial \sigma^*} \tag{2.12}$$

The sensitivity for a complex model and complex data also is a complex number. The right-hand side of Equation 2.12 consists of two different kinds of sensitivity shown in Equation 2.13 and 2.14, i.e. the real and imaginary parts of the complex sensitivity. The relation for the different derivatives is given by the following Cauchy-Riemann conditions (*Kwok*, 2010):

$$Real\left(\frac{\partial lnZ^*}{\partial ln\sigma^*}\right) = \frac{\partial ln|Z^*|}{\partial ln|\sigma^*|} = \frac{\partial \varphi_a}{\partial \varphi} \tag{2.13}$$

$$Imag\left(\frac{\partial lnZ^*}{\partial ln\sigma^*}\right) = \frac{\partial \varphi_a}{\partial ln|\sigma^*|} = -\frac{\partial ln|Z^*|}{\partial \varphi} \tag{2.14}$$

The real part of the complex sensitivity describes the change in the logarithm of the amplitude (or the phase) of the measured data due to a change in the logarithm of amplitude (or the phase) of the model parameters. The imaginary part of the complex sensitivity, also known as the cross-sensitivity, describes the change in the logarithm of amplitude (or the phase) of the measured data due to a change in the phase (or the logarithm of amplitude) of the complex model.

2.4 General formulation of the inverse problem

2.4.1 Basic formulation

Since the inversion approaches discussed in this thesis are all based on a Gauss-Newton scheme, the general inversion formulation will first be presented and the different strategies for EIT inversion will be discussed in detail afterwards. The inversion aims to find a model $\boldsymbol{m} = (m_1, m_2, m_3, ..., m_M)^T$ that can fit the measured data $\boldsymbol{d} = (d_1, d_2, d_3, ..., d_N)^T$ within the expected data error. The data misfit $\boldsymbol{\Phi}_d$ to be minimized during the inversion is defined as

$$\Phi_d = \sum_{i=1}^{N}\left|\frac{d_i - f_i(\boldsymbol{m})}{e_i}\right|^2 = ||\boldsymbol{W}_d(\boldsymbol{d} - f(\boldsymbol{m}))||^2 \tag{2.15}$$

where $f(\boldsymbol{m})$ is the forward response of model $\boldsymbol{m}$, $\boldsymbol{W}_d$ is the diagonal data weighting matrix containing the data error e_i for each individual measurement. In the ideal case when the data are perfectly fitted, the normalized data misfit $\chi^2 = \boldsymbol{\Phi}_d/N$ should be equal to 1. The geoelectrical inverse problem is highly ill-posed and a regularization term $\boldsymbol{\Phi}_m$ is introduced to stabilize the inversion (*Tikhonov and Arsenin*, 1977), resulting in the following total objective function $\boldsymbol{\Phi}$ to be minimized:

$$\Phi = \Phi_d + \lambda \Phi_m \tag{2.16}$$

where λ is the regularization factor and $\boldsymbol{\Phi}_m$ is the model roughness term given by

$$\Phi_m = ||\boldsymbol{W}_m \boldsymbol{m}||^2 \tag{2.17}$$

where $\boldsymbol{W}_m$ is the regularization matrix used to specify the desired properties of the model $\boldsymbol{m}$. Depending on the desired property of the model, different implementations of $\boldsymbol{W}_m$ can be applied. The simplest case is to use an identity matrix which regularizes the individual model parameter to prevent extremely large values (*Vogel*, 2002). Smoothness constraints can be implemented by using differential operators (*Ellis and Oldenburg*, 1994). Different types of constraints can also be implemented together by simply adding the weighted operators as a single matrix (*Li and Oldenburg*, 1999). More advanced structural information (e.g. a sharp boundary between two layers) can be implemented as known information in the regularization matrix (*Smith et al.*, 1999). In this thesis, the classical smoothness constraint is used to find the smoothest model that adequately fits the data within the specified error. As in *Chou et al.* (2016), a value of $-1/n$ is assigned to all immediate neighboring elements with n being the number of immediate neighboring elements.

Using a linear Taylor series approximation and differentiating the total objective function with respect to $\Delta\boldsymbol{m}$ results in the following model update equation (*Park and Van*, 1991; *Li and Oldenburg*, 1999):

$$(\boldsymbol{G}^T \boldsymbol{W}_d^T \boldsymbol{W}_d \boldsymbol{G} + \lambda \boldsymbol{W}_m^T \boldsymbol{W}_m)\Delta\boldsymbol{m} = \boldsymbol{G}^T \boldsymbol{W}_d^T \boldsymbol{W}_d(\boldsymbol{d} - f(\boldsymbol{m})) - \lambda \boldsymbol{W}_m^T \boldsymbol{W}_m \boldsymbol{m} \tag{2.18}$$

where $\boldsymbol{G}$ is the Jacobian matrix containing individual sensitivity values calculated using Equation 2.11 and 2.12, and T indicates the transpose of a matrix.

2.4.2 Determination of the regularization parameter

The strength of the regularization is controlled by the regularization factor λ in Equation 2.16. A large regularization factor corresponds to a smooth inversion result with a relatively high data misfit, while a small regularization factor results in a rough inversion result with a low data misfit. Usually, a smooth model with limited artifacts that can fit the measured data within the expected error is preferred. Therefore, the selection of an appropriate regularization factor is a search for an appropriate compromise solution. There are different methods to determine the appropriate regularization strength, including the discrepancy, the generalized cross-validation (GCV), and the L-curve method (*Vogel*, 2002; *Farquharson and Oldenburg*, 2004). When data error estimates are available, the discrepancy method that tries to minimize the data misfit to the expected data error (e.g. $0.95 < \chi^2 < 1.05$) typically is the preferred choice (*Vogel*, 2002; *Günther*, 2004). In this case, the inversion starts with a large regularization factor estimated from the row sums of the matrix product $\boldsymbol{G}^T\boldsymbol{W}_d^T\boldsymbol{W}_d\boldsymbol{G}$ and the regularization factor is gradually reduced to reach the target data misfit. To avoid overfitting when the inversion is approaching the target misfit, a damping scheme for the decrease of λ can be used as presented in Appendix F of *Kemna* (2000). In particular, λ is initially decreased with a factor of 0.5 when the data misfit is large. A slower adjustment is considered towards the end of the inversion by gradually increasing the factor according to the obtained data misfit.

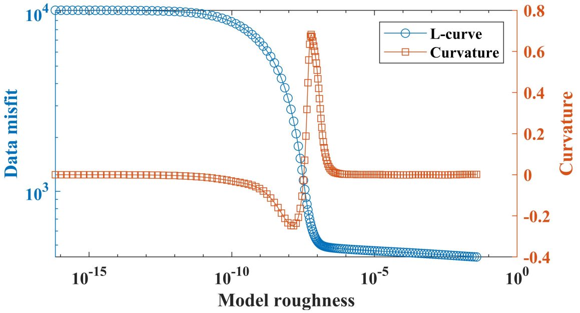

Figure 2.4: A typical L-curve and its curvature.

In the absence of data error estimates, the L-curve method is usually used to determine the regularization strength (*Li and Oldenburg*, 1999; *Loke et al.*, 2014; *Bergmann et al.*, 2017). The L-curve (*Hansen*, 1992) represents the relationship between the model roughness and the data misfit for a range of evaluated λ values, and is often presented in log space. This typically results in an L-shaped curve with a characteristic corner as shown in Figure 2.4. At this corner, a further increase of model roughness only results in a small reduction in the data misfit. Therefore, the solution at this corner is considered a good compromise between the data misfit and the model roughness. To determine this corner and the corresponding regularization factor, the curvature of the log-space L-curve can be calculated using:

$$c(\Psi_m, \Psi_d) = \frac{\Psi_d'' \Psi_m' - \Psi_d' \Psi_m''}{({\Psi_d'}^2 + {\Psi_m'}^2)^{3/2}} \tag{2.19}$$

with $\Psi_d = ln(\Phi_d)$ and $\Psi_m = ln(\Phi_m)$. The location of the corner can then be determined using the maximum value of the curvature (see Figure 2.4).

In the case of nonlinear geoelectrical inverse problems with large model domains, calculating the exact L-curve can be computationally expensive. Instead, a linear approximation can be applied (*Li and Oldenburg*, 1999; *Günther*, 2004) by using the Jacobian matrix $\boldsymbol{G}$ for calculating the forward response. In particular, after calculating the forward response and Jacobian matrix using the FEM modelling approach for a given input model, the model update $\Delta\boldsymbol{m}(\lambda)$ can be solved for a range of λ values using Equation 2.18. The corresponding forward responses can then be approximated using:

$$f(\boldsymbol{m} + \Delta\boldsymbol{m}(\lambda)) = f(\boldsymbol{m}) + \boldsymbol{G}\Delta\boldsymbol{m}(\lambda) \tag{2.20}$$

With these approximated forward responses, the model roughness and data misfit terms for each evaluated λ can be calculated using Equation 2.15 and 2.17, resulting in an approximated L-curve that can be interpreted in the same way as the full L-curve.

2.4.3 Line search

To avoid overfitting and to stabilize the nonlinear inverse problem, a line search procedure is often used to find a proper step length (*Günther*, 2004). Once the full model update $\Delta\boldsymbol{m}_i$ for the ith iteration is calculated using Equation 2.18, a suitable step length τ_{opt} should be found to update the model using $\boldsymbol{m}_{i+1} = \boldsymbol{m}_i + \tau_{\text{opt}}\Delta\boldsymbol{m}_i$. Three approaches to find the optimal step length have been used for ERT inversion. The first and most straightforward method is to calculate the exact forward response using FEM modelling for a sequence of trial step lengths in the expected range ($0< \tau \leqslant 1$), which is possible but not practically feasible due to the high computation load. The second approach is based on fitting a second order polynomial to a limited number of trial runs (*Kemna*, 2000; *Günther*, 2004). In particular, exact forward calculations are carried out for the full update ($\tau = 1$) and half the update ($\tau = 0.5$) to obtain the corresponding total objective function values. Together with the solution from the previous iteration (i.e. $\tau = 0$), the parameters of a second-order polynomial function describing the total objective term as a function of the step length can be obtained. The optimal step length τ_{opt} can then be found by searching for the minimum of the parabolic function in the range between 0 and 1. The third approach is based on a linear interpolation of the forward responses (*Günther*, 2004). In particular, the exact forward calculation is carried out for the full update ($\tau = 1$) only. Together with the solution from the previous iteration (i.e. $\tau = 0$), the forward responses for other evaluated step lengths can be interpolated using $f(\boldsymbol{m} + \tau\Delta\boldsymbol{m}_i) = f(\boldsymbol{m}) + \tau(f(\boldsymbol{m} + \Delta\boldsymbol{m}_i) - f(\boldsymbol{m}_i))$. Using the interpolated forward responses, a curve of the total objective term as a function of the step length can be obtained. The optimal step length can then be found by searching for the minimum of this curve. *Günther* (2004) has shown that all three methods provide similar optimal step lengths. Therefore, the linear interpolation method is used in this thesis given that only one FEM modelling is required.

2.4.4 Inversion workflow

The inversion workflow used throughout the thesis is summarized in Figure 2.5. In the first step (#1a), a homogeneous input model is determined from the measured data (e.g. mean value of apparent electrical conductivity), which is then used to calculate the forward response and the Jacobian matrix using FEM modelling (#1b). In the second step (#2), the calculated forward response and the Jacobian matrix are used together with the measured data to determine the model update using Equation 2.18. In the third step (#3), a line search procedure is performed to find the optimal step length to update the model. In the fourth step (#4), the stopping criteria for the inversion is checked. The inversion then repeats steps 2, 3, and 4 until it reaches the desired data misfit or convergence. In the case of the discrepancy method, the stopping criteria is that the normalized data misfit χ^2 reaches the target range (i.e. $0.95 < \chi^2 < 1.05$). When the (approximated) L-curve method is used to determine the regularization strength, a 3% relative error weighting is applied to account for the contribution of small impedances in the inversion. The inversion stops at convergence (i.e. the difference in the data misfit between two iterations is less than 5%) or when the relative RMS error is below 5%.

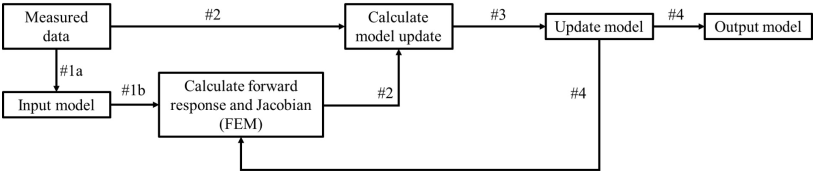

Figure 2.5: Inversion workflow.

2.4.5 Model appraisal

A low data misfit does not always ensure well-resolved inversion results due to the non-uniqueness of the geoelectrical inverse problem. Therefore, model appraisal is needed to evaluate the inversion results. The cumulative sensitivity provides a straightforward assessment of the measurement configurations in terms of the sensitivity coverage. However, it does not fully consider the regularization applied in the inversion. In addition, it has been highlighted in *Kemna* (2000) that high sensitivity does not ensure high model resolution. In this thesis, the model resolution and the relative eigenvalue range (RER) are used as model appraisal tools. The model resolution matrix $\boldsymbol{R}$ can be calculated using (*Friedel*, 2003):

$$\boldsymbol{R} = (\boldsymbol{G}^T \boldsymbol{W}_d^T \boldsymbol{W}_d \boldsymbol{G} + \lambda \boldsymbol{W}_m^T \boldsymbol{W}_m)^{-1} \boldsymbol{G}^T \boldsymbol{W}_d^T \boldsymbol{W}_d \boldsymbol{G} \tag{2.21}$$

Ideally, the main diagonal elements in the resolution matrix are all 1, which would suggest that the model is perfectly resolved. In any practical case, the main diagonal elements vary between 0 and 1. The model resolution has been widely used in optimized experimental design for ERT (*Stummer et al.*, 2004; *Wilkinson et al.*, 2006b; *Loke et al.*, 2010; *Wagner et al.*, 2015), and is considered a useful tool for the evaluation of geoelectrical inversion results.

The relative eigenvalue range is determined from the eigenvalue spectrum (Figure 2.6) of the Hessian matrix $\boldsymbol{G}^T\boldsymbol{W}_d^T\boldsymbol{W}_d\boldsymbol{G}$. The calculated eigenvalues are normalized by the largest eigenvalue, and the indices of the eigenvalues are normalized by the total number of model parameters. A threshold value of the damping level below which the eigenvalues are considered insignificant should be defined to separate the resolved model space and the null space. As defined in *Maurer et al.* (2009), the part to the left of the intersection of the spectrum with the threshold line is considered as the relative eigenvalue range (RER) and the part to the right is the null space. The RER has been used in optimized experimental design for seismic full waveform inversion (*Maurer et al.*, 2009; *Krampe et al.*, 2021) and in the assessment of geoelectrical measurement configurations (*Blome et al.*, 2011; *Wang et al.*, 2022). The choice of damping level is subjective and survey dependent as pointed out in *Krampe et al.* (2021). A threshold value of 10^{-3} as used in *Blome et al.* (2011) and *Wang et al.* (2022) for the ERT problem was adopted in this thesis.

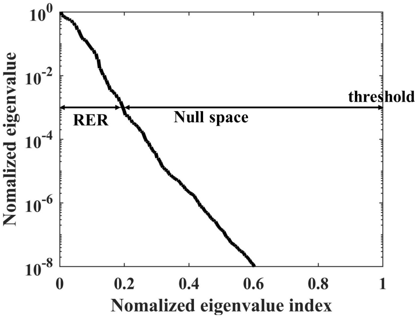

Figure 2.6: A typical eigenvalue spectrum with the relative eigenvalue range (RER) and the null space indicated.

2.5 Inversion strategies for EIT measurements

EIT data inversion deals with complex data and model parameters, which requires additional considerations within the context of the general inversion workflow outlined above. Different strategies for EIT data inversion have been proposed and are described in the following. To be consistent between the different inversion strategies, the logarithm of both the complex impedance and the complex electrical conductivity will be used in all three strategies.

2.5.1 Direct complex inversion (CVI)

The first strategy is a direct complex inversion using the general formulation described above and the complex form of data and model, i.e. $\boldsymbol{d} = ln|\boldsymbol{Z}^*| + i\boldsymbol{\varphi}_a$ and $\boldsymbol{m} = ln|\boldsymbol{\sigma}^*| + i\boldsymbol{\varphi}$. Although it has been pointed out that the direct inversion of complex data can be problematic for the imaginary part of the model (*Kemna*, 2000; *Günther and Martin*, 2016), the approach is nevertheless considered here because it is still being used. The data error in the direct complex inversion is implemented as a complex number (*Kemna*, 2000; *Flores Orozco et al.*, 2012b) with the error for the logarithm amplitude as the real part and the error for the phase as the imaginary part i.e. $e = e_A + ie_P$ with e_A and e_P being the error for the logarithm of the amplitude and the phase of the measured complex impedance, respectively. This CVI strategy requires the use of complex Jacobian and data weighting matrices, and thus the use of the conjugate (Hermitian) transpose, which is typically indicated with H instead of T in Equation 2.18. In this approach, the complex data misfit is represented by a single real number, but the χ^2 values for the final electrical conductivity amplitude and phase distributions will also be presented separately in this thesis.

2.5.2 Two-step real-valued inversion (RVI)

The second strategy is a two-step real-valued inversion approach (RVI) based on the Cauchy-Riemann condition for the real part of the sensitivity. It ignores the cross-sensitivity for the inversion of both amplitude and phase of the electrical conductivity. In the first step, the logarithmic amplitude of the measured complex impedance is inverted using a real-valued formulation, which is identical to ERT inversion. Namely, the data and model paramters $\boldsymbol{d}$ and $\boldsymbol{m}$ are the $ln(|\boldsymbol{Z}^*|)$ and $ln(|\boldsymbol{\sigma}^*|)$, respectively. The data error in the first step considers only the log-transformed data error for the logarithmic amplitude of the measured complex impedances, i.e. $e = e_A$. Since the first step of RVI strategy is identical to ERT inversion, the Jacobian matrix $\boldsymbol{G}_{RVI}$ is calculated using a real-valued form based on the reciprocity theorem presented in section 2.3.

$$\boldsymbol{G}_{RVI} = \frac{\partial ln|\boldsymbol{Z}^*|}{\partial ln|\boldsymbol{\sigma}^*|} = \frac{|\boldsymbol{\sigma}^*|}{|\boldsymbol{Z}^*|}\frac{\partial|\boldsymbol{Z}^*|}{\partial|\boldsymbol{\sigma}^*|} = -\frac{|\boldsymbol{\sigma}^*|}{|\boldsymbol{Z}^*|}\int \frac{\nabla|\boldsymbol{\phi}_C^*|}{\boldsymbol{I}_C} \cdot \frac{\nabla|\boldsymbol{\phi}_P^*|}{\boldsymbol{I}_P} d\Omega \tag{2.22}$$

In the second step, the data and model parameters $\boldsymbol{d}$ and $\boldsymbol{m}$ are the measured phase φ_a and the phase φ for each model element, respectively. The data error only consists of the estimated error for the phase, i.e. $e = e_P$. The Jacobian matrix $\boldsymbol{G}_{RVI}$ from the last iteration in the first step is used in the second step to obtain the model update and to calculate the forward phase response. This is based on the following assumption when the cross-sensitivity is ignored.

$$\boldsymbol{G}_{RVI} \approx Real(\frac{\partial ln\boldsymbol{Z}^*}{\partial ln\boldsymbol{\sigma}^*}) \tag{2.23}$$

In this case, with the use of a fixed Jacobian matrix, the inverse problem in the second step becomes linear (*Martin and Günther*, 2013).

2.5.3 Alternate inversion (ALT)

The third strategy is based on the method proposed by *Johnson and Thomle* (2018). It considers the complex coupling in the forward modelling by using a decoupled and real-valued approach, but the imaginary part sensitivity is again ignored. In the case of small phase angles below 200 mrad, this method is very similar to the two-step real-valued inversion described above. The first step is again the ERT inversion. The difference is that the calculation of the forward response in the second step is based on the decoupled approach. To address this and to compare with the approximated forward modelling using the Jacobian matrix in the RVI approach, exact complex forward modelling will be used in this thesis to calculate the forward response in the second step of the ALT approach. This then becomes the same method as the final phase improvement in *Kemna* (2000).

In the case of large phase angles, the key feature of this strategy is to alternately update the real and imaginary parts of the electrical conductivity in each iteration so that the forward calculation can be carried out based on the updated complex model. However, it should be noted that the real part of the complex sensitivity in *Johnson and Thomle* (2018) was approximated based on the reciprocity theorem (*Geselowitz*, 1971) using only the real part of the potential distribution as presented in Equation B3 of *Johnson and Thomle* (2018), which should include the contribution of the imaginary part of the potential distribution in the case of models with large phase values. To implement this strategy in terms of logarithmic amplitude and phase angle in this thesis, the forward response and the Jacobian matrix were calculated using the exact complex modelling (i.e. Equation 2.8 to 2.12), but only the real part of the calculated complex sensitivity will be used to obtain the model update in Equation 2.18. In particular, the amplitude of the complex electrical conductivity is updated first in each iteration. The line search for the amplitude is based on the phase model from the last iteration. The phase model update is then calculated using the same Jacobian matrix and the step length for the phase model is determined using the updated electrical conductivity amplitude. In the end, the forward response, the Jacobian matrix, and the data misfit are updated based on the complex model.

2.6 Field measurements and used EIT instrumentation

Three sets of field measurements will be used in this thesis to evaluate the methodological developments. One field dataset was measured in Selhausen, Germany (referred to as Selhausen dataset). The soil at this site is a Luvisol that developed in a layer with a silt loam texture (*Weihermüller et al.*, 2007; *Cai et al.*, 2016). The data was measured using a long-term EIT monitoring system which has 40 electrodes with 25 cm spacing. The selected electrode configurations (647 data points) were adapted to the capabilities of the multi-channel system, while still providing enough information about the subsurface. This dataset will be used in Chapter 3 to test different inversion strategies. For more information about the Selhausen dataset, the reader is referred to *Weigand et al.* (2022).

The other two sets of measurements were acquired near Milano, Italy and they are described in detail in *Zimmermann et al.* (2019). One set of measurements was obtained near Lozzolo (referred to as Lozzolo dataset) in a kaolinite quarry with a complex geostructural and stratigraphic setting. It was shown in *Zimmermann et al.* (2019) that this site has a subsurface with high electrical conductivity and that inductive coupling is the main source of error. This dataset will be used in Chapter 4 for a detailed investigation of inductive coupling. The other set of measurements was acquired near Senna Lodigiana (referred to as Senna Lodigiana dataset) in the Lodi plain along a terrace of the Po river. Measurements at this site showed low electrical conductivity and it was found that capacitive coupling dominated the data quality (*Zimmermann et al.*, 2019). This dataset will be used in Chapter 5 to investigate capacitive coupling in more detail. For more information about these two field sites in Italy, the reader is referred to *Inzoli* (2016). The survey layout shown in Figure 2.7 was used for measurements at both test sites in Italy. The survey line has 30 electrodes with 1 m spacing. The 30 electrodes were connected to the measurement system using 30 individual shielded cables, which were arranged in a fan shape. The system is located at 5 m distance from the survey line.

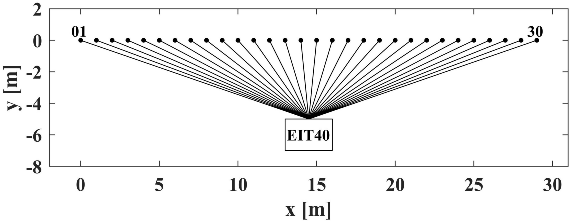

Figure 2.7: Schematic representation of a fan-shaped survey layout.

The field sEIT measurements used in this thesis were acquired by the custom-made 40-channel sEIT measurement system shown in Figure 2.8(a). More details about the system, such as correction methods for amplification errors, signal drift, current measurement errors and propagation delay, can be found in *Zimmermann et al.* (2008a) and *Zimmermann et al.* (2010). Here, only the key features of the system that are important for the developments presented in this thesis will be provided. Figure 2.8(b) shows a block diagram of the system. At each electrode module (UI01-UI40), there is an integrated amplifier for potential measurements and an integrated relay for current injection. Thus, the potential can be recorded at the electrode directly and the inner cable capacity can thereby be removed. The system measures the voltage relative to the system ground at all electrodes except the two current electrodes. The potential difference for a four-pole electrode configuration can then be calculated in a post-processing step. For each current excitation, the system measures the excitation current I_1 through the positive current pole and I_2 through the negative current pole. The symmetric current I_s and leakage current I_L can then be calculated by (*Zimmermann et al.*, 2019):

$$I_s = \frac{I_1 - I_2}{2} \tag{2.24}$$

$$I_L = I_1 + I_2 \tag{2.25}$$

Since the system measures the potential at all remaining electrodes, only the dipoles used for current injection need to be specified a priori. For the field measurements with 30 electrodes, a circulating measurement strategy was used for current injection (*Xu and Noel*, 1993) where 16 electrodes were skipped between the two current poles for each injection (i.e. current injections at 01–18, 18–05, 05–22, . . .) to obtain measurements with a high signal-to-noise ratio. This was repeated until electrode 01 was reached to ensure that each current electrode is used equally often. Four-pole measurements can be reconstructed from the measured three-pole dataset by superposition. In principle, it is possible to construct any four-pole electrode configuration from this complete three-pole dataset (*Xu and Noel*, 1993). However, only those four-pole configurations with the same current pairs as used for current excitations will be considered in this thesis to avoid the accumulation of noise during superpositioning (*Blome et al.*, 2011). To improve measurement quality, each current injection was repeated three times and measurements with exchanged current excitation electrodes (i.e. 01–18 and 18–01) were also acquired. The average of the normal and reverse excitations and the three repeated measurements was used in the sEIT data reconstruction and inversion. For each current excitation, the complex impedance was measured at 15 frequencies in the range from 0.1 Hz to 10 kHz (0.10, 0.23, 0.52, 1.18, 2.68, 6.10, 13.9, 31.3, 71.4, 164, 366, 850, 1950, 4400 and 10 000 Hz).

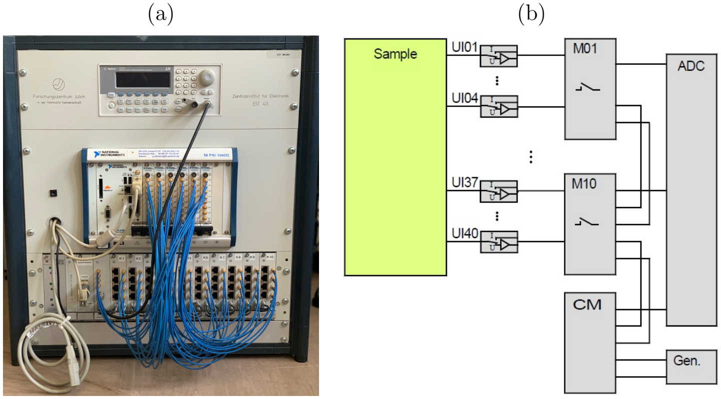

Figure 2.8: (a) The EIT40 measurement system and (b) block diagram of the system (*Zimmermann et al.*, 2008a)

Chapter 3

Comparison of different inversion strategies for EIT measurements

3.1 Introduction

In this chapter[1], the inversion strategies CVI, RVI, and ALT reviewed in Chapter 2 will be compared with a newly formulated complex inversion approach. The CVI strategy is a complex-valued approach that follows the formulation for ERT inversion, but treats all parameters as complex values. The RVI strategy is a two-step real-valued approach where the amplitude of data is inverted first in the real number domain using a standard ERT inversion routine, and the phase is then separately inverted using the final real-valued Jacobian from the first step. The ALT strategy is similar to the two-step RVI approach in case of small phase values, but considers complex forward modelling in the second step. In the case of large phase values, the ALT strategy updates the real and imaginary parts of the model alternately so that the real part of the forward response can also be calculated based on the complex model. The review of the three inversion strategies presented in Chapter 2 showed that none of them can fully address all important aspects in the EIT data inversion, including the complex nature of EIT data inversion and the different order of magnitude for the real and imaginary part of data and model. Therefore, the aim in this chapter is twofold. First, a new strategy that can fully consider the complex nature of EIT data inversion while allowing for separated treatment of the real and imaginary parts of the data and model parameters in terms of data weighting and model regularization needs to be established. Then, this new strategy will be compared with other strategies. The EIT inversion can be implemented with different formulations of the complex data and model parameters, for example the amplitude and phase (*Kemna*, 2000) and the real and imaginary parts of the complex electrical conductivity (*Johnson and Thomle*, 2018). As is well known from ERT inversion, the use of the logarithm is often desirable since it ensures the positivity of the inverted resistivity amplitude and suitably scales the inverse problem (*Loke*, 2004). In this chapter, the logarithm of both the complex impedances and the complex electrical conductivity will be considered as the data and model parameter. In the following, a detailed description of the new inversion strategy will first be presented. Next, synthetic modelling studies will be carried out for the comparison of different inversion strategies. Models with small and large phase angles will be used to investigate the performance of the different inversion strategies. In the end, inversion of actual field measurements will also be presented.

---

[1] This chapter is adapted from a manuscript submitted to Geophysical Journal International: Wang, H., Zimmermann, E., Weigand, M., Vereecken, H., and Huisman, J. A.. Comparison of different inversion strategies for electrical impedance tomography (EIT) measurements

3.2 Materials and methods

3.2.1 Improved complex inversion (CVI+)

This strategy (CVI+) is an extension of the CVI strategy. It also relies on the concept of complex inversion but treats data weighting and model regularization for the amplitude and phase separately. This was achieved by extending the data vector to $\boldsymbol{d} = (ln|\boldsymbol{Z}^{*}|, \boldsymbol{\varphi_a})^T$ and the model parameter vector to $\boldsymbol{m} = (ln|\boldsymbol{\sigma}^{*}|, \boldsymbol{\varphi})^T$, which are thus twice as large as in the CVI strategy. The data error for the amplitude and phase was separately assigned to the corresponding measurements through the diagonal of the extended data weighting matrix. Similarly, an extended regularization matrix was constructed that consists of two original regularization matrices at the main diagonal and two null matrices at the off-diagonal positions. To allow for different regularization strengths for the magnitude and phase, a diagonal matrix $\boldsymbol{L}$ with two separate regularization factors is introduced, resulting in the following modified model update equation

$$(\boldsymbol{G}^T\boldsymbol{W}_d^T\boldsymbol{W}_d\boldsymbol{G} + \lambda\boldsymbol{W}_m^T\boldsymbol{W}_m)\Delta\boldsymbol{m} = \boldsymbol{G}^T\boldsymbol{W}_d^T\boldsymbol{W}_d(\boldsymbol{d} - f(\boldsymbol{m})) - \boldsymbol{W}_m^T\boldsymbol{L}\boldsymbol{W}_m\boldsymbol{m} \qquad (3.1)$$

To complete this extended formulation, the Jacobian matrix is defined as:

$$\frac{\partial \boldsymbol{d}}{\partial \boldsymbol{m}} = \begin{bmatrix} \dfrac{\partial ln|\boldsymbol{Z}^*|}{\partial ln|\boldsymbol{\sigma}^*|} & \dfrac{\partial ln|\boldsymbol{Z}^*|}{\partial \boldsymbol{\varphi}} \\ \dfrac{\partial \boldsymbol{\varphi}_a}{\partial ln|\boldsymbol{\sigma}^*|} & \dfrac{\partial \boldsymbol{\varphi}_a}{\partial \boldsymbol{\varphi}} \end{bmatrix} \tag{3.2}$$

In each iteration, the complex forward operator is required to calculate the forward response and the complex sensitivity which is then used to construct the Jacobian in Equation 3.2 based on the Cauchy-Riemann relations. In the CVI+ approach, the data misfit term for the complete data vector and the separated data misfit terms for amplitude and phase were all examined after each iteration to stop the inversion and to adjust the corresponding regularization factors. At the end of the inversion, it was ensured that the χ^2 values for the extended data vector as well as the separate terms are all in the target range.

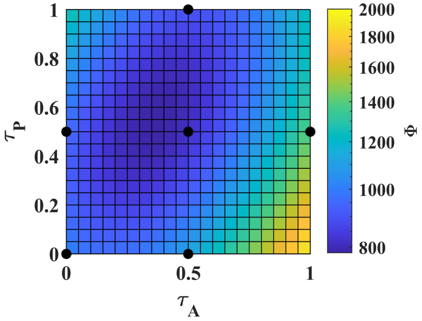

Figure 3.1: Total objective function value Φ as a function of step lengths τ_A and τ_P for the logarithmic amplitude and phase angle of the electrical conductivity. Values at the six black points are calculated from exact forward modelling to determine the six parameters in Equation 3.3.

A two-dimensional line search procedure was proposed to find the optimal step lengths τ_A and τ_P for the logarithmic amplitude and phase of the electrical conductivity, respectively. Instead of fitting a three-point polynomial function, a six-point quadratic surface is fitted

$$\Phi = A\tau_A^2 + B\tau_P^2 + C\tau_A\tau_P + D\tau_A + E\tau_P + F \tag{3.3}$$

where A-F are the six parameters to determine the quadratic surface. Figure 3.1 illustratively shows the two-dimensional line search method. Once the model update is calculated, forward modelling will be conducted for five combinations of τ_A and τ_P as represented by the black dots in Figure 3.1 (i.e. $[\tau_A\ \tau_P]$ = [0.5 0], [0 0.5], [0.5 0.5], [1 0.5], [0.5 1]). Together with the solution from the previous iteration (i.e. $[\tau_A\ \tau_P]$ = [0 0]), six parameters in Equation 3.3 can be solved and the minimum of the total functional Φ can be found in the desired range ($0 < \tau_A, \tau_P \leqslant 1$).

3.2.2 Synthetic modelling study

The two synthetic models shown in Figure 3.2 were used. Model-1 has two layers for the amplitude of the electrical conductivity. The top layer has a conductivity of 2 mS/m, representing a dry soil layer, and the bottom layer has a higher conductivity of 100 mS/m. The phase distribution shows a phase anomaly with a maximum phase angle of 30 mrad, which could for example represent a target area with zerovalent iron particles (*Joyce et al.*, 2012; *Emerson et al.*, 2021). In contrast, Model-2 has an extremely high phase angle layer of 1000 mrad, representing highly polarizable materials (e.g., rock salt). Although it is rare in reality, the amplitude of the electrical conductivity for Model-2 is deliberately set as a homogeneous model to illustrate problems with the simplified inversion approaches later on. For both subsurface models, a survey line consisting of 21 electrodes with 1 m electrode spacing and a dipole-dipole measurement scheme were used to obtain the synthetic EIT data. The modelled complex impedances for Model-1 were contaminated with 3% relative error for the amplitude and 1 mrad absolute error for the phase. For Model-2, 3% relative error for the amplitude was also applied but a higher phase error of 5 mrad was adopted. The applied errors were also used in the subsequent error-weighted inversion. This selection of error parameters is similar to previously used estimates in other studies (*Slater and Binley*, 2006; *Martin and Günther*, 2013; *Johnson and Thomle*, 2018). With this selection of error parameters, it should be noted that all the measurements were equally weighted. This is clear for the phase angle because constant phase errors were applied. For the amplitude of complex impedance, the 3% relative error also corresponds with a constant error after log-transformation (*Friedel*, 2003; *Günther et al.*, 2006).

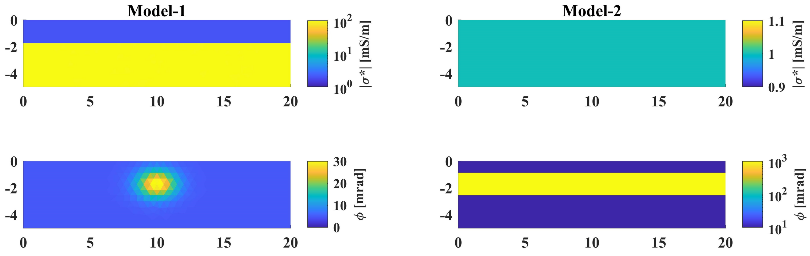

Figure 3.2: Amplitude and phase of two subsurface models used in the synthetic modelling study.

3.3 Results and discussion

3.3.1 Results for Model-1 (small phase angle)

Figure 3.3 shows the inversion results for Model-1 obtained using the four inversion strategies. It should be noted that the results for the RVI and ALT strategies for the amplitude are identical because the implementations have the same first step (i.e. ERT inversion). The results for the inverted electrical conductivity amplitude distribution were very similar for all strategies. The two layers were well reconstructed in all results. Although the data misfit term in the CVI strategy aggregates the data misfit for the amplitude and phase angle in a single real-valued misfit, the χ^2 values are calculated and presented separately for the final electrical conductivity amplitude and phase distributions. The aggregated χ^2 value for the inversion results was minimized to the target range. It was almost identical to χ^2 values of the electrical conductivity amplitude and the ERT inversion result in the first step of the RVI strategy, which indicates that the aggregated misfit in the CVI strategy was dominated by the error for the electrical conductivity amplitude as expected. The inverted phase distribution obtained with the CVI strategy showed artifacts and strongly negative phase angles. The high phase anomaly was not accurately located and the overall image appeared very rough, although the final χ^2 value of the phase inversion obtained with the CVI strategy was very close to the target range. In contrast, the phase anomaly was well resolved in the distributions obtained using the RVI, ALT, and CVI+ strategies. Moreover, the images were very similar and presented much smoother phase distributions. It should be noted that the χ^2 value for the phase distribution obtained using the RVI strategy is calculated with the forward response approximated using the Jacobian matrix. The exact χ^2 value using a complex modelling was also calculated, and the result was 1.086 instead of the 1.041 using the approximated Jacobian matrix. Although it is slightly higher than the upper limit of the target range, it is still acceptable.

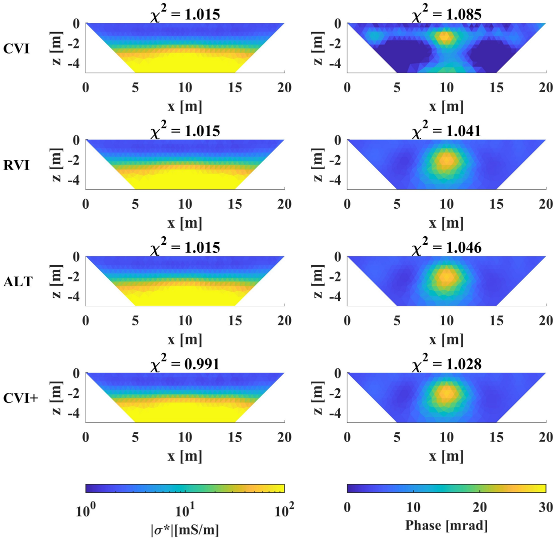

Figure 3.3: Inversion results for electrical conductivity amplitude and phase of Model-1 using the CVI (direct complex inversion), RVI (two-step real-valued inversion), ALT (alternate inversion or final phase improvement), and CVI+ (improved complex inversion) strategies.

From the imaging results presented in Figure 3.3, it is clear that visible differences can only be found in the phase images produced by the CVI strategy. This is due to the use of the same data weighting and regularization factor for the amplitude and the phase angle in the CVI strategy. However, the appropriate regularization strength and thus the optimal regularization factor can be quite different for the inversion of electrical conductivity amplitude and phase angle. Table 3.1 presents the data weighting and final regularization factors for the inversion of phase angle using different strategies. Because both the inversion of electrical conductivity amplitude and phase angle are equal-weighted inversions in this synthetic study, one value (i.e. $|1/e|^2$ in Table 3.1) can be used to represent the data weighting. The RVI, ALT, and CVI+ strategies have the same data weighting and comparable regularization factors for the inversion of the phase angle because these strategies allow for separated treatment of the amplitude and phase angle in terms of data weighting and model regularization. For the CVI strategy, the data weighting and final regularization factor were quite different from the other strategies. In principle, the CVI strategy should be able to provide a plausible phase distribution if the ratio of the final regularization factor and the data weighting would be similar as in the other strategies. However, Table 1 shows that this ratio was much smaller (0.06 compared to 1.63), indicating that the rough phase images produced by the CVI strategy are due to the smaller regularization strength applied in the phase inversion. This fundamentally explains why the direct complex inversion (CVI) is not able to produce reliable inversion results for the phase angle. Depending on the different contrasts in the amplitude and phase of the electrical conductivity distribution and different data errors in the measured amplitude and phase of the complex impedances, the phase model can be under- or overestimated. *Kemna* (2000) proposed a final phase improvement starting from the phase model obtained using the direct complex inversion, which was useful given that the cases presented in *Kemna* (2000) were underestimated or slightly overestimated. The rough phase model with negative values shown in Figure 3.3 may not be a good starting model for a second phase inversion step. Therefore, it is suggested that such a second step should start from a homogeneous model as in the RVI and ALT strategies.

Table 3.1: Data weighting and the final regularization factors for different inversion strategies in the inversion of the phase angle of Model-1.

Method	$\lvert 1/e \rvert^2$	final regularization factor λ	$\frac{\lambda}{\lvert 1/e \rvert^2}$
CVI	1.11×10^3	6.63×10^1	0.06
RVI	1.00×10^3	1.63×10^1	1.63
ALT	1.00×10^3	1.64×10^1	1.64
CVI+	1.00×10^3	1.42×10^1	1.42

The results produced by the CVI+ strategy show slightly different final χ^2 values and regularization factors compared to the RVI and ALT strategies. This is because the use of the two-dimensional line search can result in different step lengths, and thus different damping of λ. Moreover, the starting λ for the inversion of the phase angle in the CVI+ strategy is estimated based on the Jacobian calculated using a homogeneous model, while the starting λ for the phase angle in the RVI and ALT strategies is estimated based on the Jacobian for the final electrical conductivity model. Despite these differences, the final χ^2 values for the RVI, ALT, and CVI+ strategies were all in the target range and the final regularization factors were similar and of the same order of magnitude.

3.3.2 Results for Model-2 (large phase angle)

Figure 3.4 shows the inversion results for Model-2 obtained using the four inversion strategies. It is clear that only the CVI+ strategy successfully resolved the homogeneous amplitude of the electrical conductivity model, whereas the other strategies all resulted in anomalies in the inverted amplitude of the electrical conductivity. Although the phase distributions obtained by the CVI, RVI, and ALT strategies clearly showed the layered structure, it is difficult to interpret without a reliable distribution of the amplitude of the electrical conductivity. Therefore, the results obtained by the CVI+ strategy were considered as a reference and the reasons for the failure of the other three strategies will be explained in the following.

In the case of Model-1, the inversion results produced by the CVI strategy were dominated by the real part of the data and the model. However, this is not the case anymore in the presence of extremely large phase angles (i.e. Model-2). To analyze the inversion results of Model-2 produced by the CVI strategy and to compare them with the results produced by the CVI+ strategy, the data weighting and the final regularization factors for the CVI and CVI+ strategy are presented in Table 3.2. The ratio of the final regularization factor and the data weighting for the CVI strategy was about two orders of magnitude smaller (0.05 compared to 7.05) than the ratio for the CVI+ strategy in the case of the inversion of the amplitude of the impedance. This indicates that the regularization strength applied to the amplitude was too small in the CVI strategy. In the case of the inversion of the phase angle, the difference in the ratios for the CVI and CVI+ strategies were much smaller, which suggests that the inversion results for Model-2 obtained by the CVI strategy were dominated by the phase angle and not the amplitude. Although the final χ^2 value for the amplitude of the electrical conductivity was in the target range for the CVI strategy,

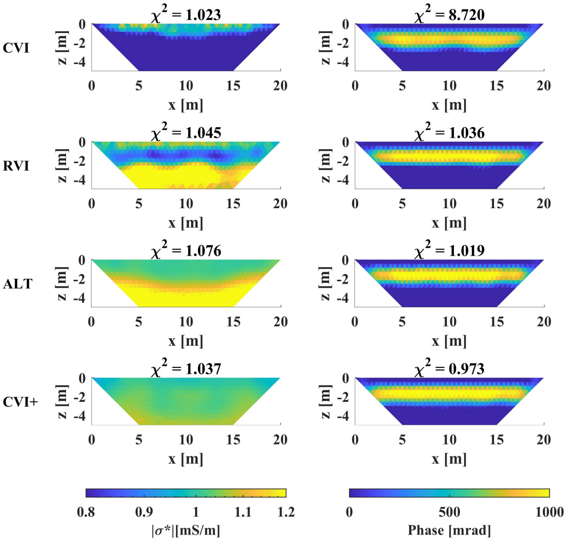

Figure 3.4: Inversion results for electrical conductivity amplitude and phase of Model-2 using the CVI (direct complex inversion), RVI (two-step real-valued inversion), ALT (alternate inversion or final phase improvement), and CVI+ (improved complex inversion) strategies.

the image presented mostly lower electrical conductivity (< 0.8 mS/m), which is much different from the expected homogeneous distribution of 1 mS/m.

The inversion results obtained by the RVI strategy showed a layered structure for the amplitude of the electrical conductivity, which is not in agreement with the homogeneous true model. The reason for the failure of the RVI strategy is rooted in the modelled amplitude of the apparent conductivity. Figure 3.5 shows the pseudo-section of the amplitude of the modelled apparent electrical conductivity using Model-2, which clearly showed a relatively low conductivity layer in the middle. This explains the layered structure obtained for the inverted amplitude of the complex conductivity using the RVI strategy. In the case of ERT or EIT with small phase values, the modelled apparent electrical conductivity for a homogeneous conductivity amplitude of 1 mS/m is expected to be 1 mS/m. Due to the extremely large phase angles, the amplitude of the modelled apparent electrical conductivity ranges from 0.92 to 1.02 mS/m, which suggests differences up to 8%.

Table 3.2: Data weighting and the final regularization factors for different inversion strategies in the inversion of the phase angle of Model-2.

Method	$\|1/e\|^2$	final regularization factor λ	$\frac{\lambda}{\|1/e\|^2}$
CVI (Amplitude)	1.11×10^3	5.95×10^1	0.05
CVI+ (Amplitude)	1.14×10^3	8.04×10^1	7.05
CVI (Phase)	1.11×10^3	5.95×10^1	0.05
CVI+ (Phase)	4.00×10^4	3.58×10^1	0.01

The final χ^2 values for the results obtained by the RVI strategy were also calculated using a complex instead of the real-valued forward modelling, and this resulted in χ^2 values of 114.16 and 787.86 for the amplitude and phase, respectively. This clearly highlights that in the case of large phase angles the RVI strategy is not suitable for the inversion of EIT data and that complex forward modelling is needed. Although the ALT strategy considered complex forward modelling, the results produced by this strategy were also not satisfactory. The reason for the failure of the ALT strategy is the negligence of the cross-sensitvity, which will be explained in detail in the next section.

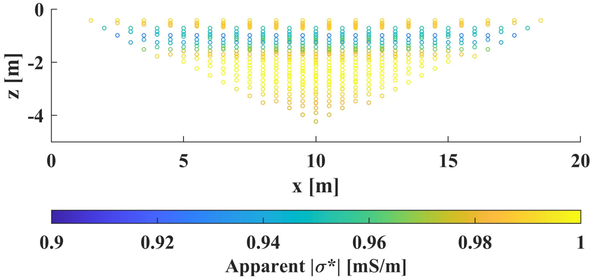

Figure 3.5: Pseudo-section of the amplitude of the modelled apparent complex conductivity using Model-2.

3.3.3 Discussion of cross-sensitivity

To explore how the cross-sensitivity contributes to the inversion of the amplitude and phase angle of the electrical conductivity, four different Jacobian matrices were defined based on the complete extended Jacobian in Equation 3.2

$$\boldsymbol{G}_{A0} = \frac{\partial ln|\boldsymbol{Z}^*|}{\partial ln|\boldsymbol{\sigma}^*|}, \boldsymbol{G}_{AX} = \begin{bmatrix} \boldsymbol{G}_{A0} \\ \dfrac{\partial \boldsymbol{\varphi}_a}{\partial ln|\boldsymbol{\sigma}^*|} \end{bmatrix}, \boldsymbol{G}_{P0} = \frac{\partial \boldsymbol{\varphi}_a}{\partial \boldsymbol{\varphi}}, \boldsymbol{G}_{PX} = \begin{bmatrix} \dfrac{\partial ln|\boldsymbol{Z}^*|}{\partial \boldsymbol{\varphi}} \\ \boldsymbol{G}_{P0} \end{bmatrix} \tag{3.4}$$

where $\boldsymbol{G}_{A0}$ and $\boldsymbol{G}_{P0}$ represent the Jacobian for the logarithm of the conductivity amplitude and the phase angle without considering the cross-sensitivity (i.e. the real part sensitivity and $\boldsymbol{G}_{A0} = \boldsymbol{G}_{P0}$), and $\boldsymbol{G}_{AX}$ and $\boldsymbol{G}_{PX}$ represent the Jacobian for the logarithm of the conductivity amplitude and the phase angle including the cross-sensitivity.

The inversion results of Model-2 obtained with the ALT and CVI+ strategy indicated that the cross-sensitivity provided unique information during the inversion. To evaluate the information content in the Jacobian matrix, the relative eigenvalue range (RER) of the Hessian matrix ($\boldsymbol{H} = \boldsymbol{G^T W_d^T W_d G}$) was adopted. In short, the RER value represents the resolved model space and high RER values correspond to a small null space in the model space. The calculated complex sensitivity of the model obtained in the first iteration was adopted for the determination of the RER value because the cross-sensitivity for the homogeneous start model is zero. It should also be noted that the eigenvalue spectra for the amplitude and phase angle should be identical in the absence of data weighting, but can be different when data weighting is considered. Figure 3.6 presents the eigenvalue spectra of different Jacobian matrices for both Model-1 and Model-2. In the case of Model-1, the RER values of the Jacobian matrices $\boldsymbol{G}_{A0}$ and $\boldsymbol{G}_{AX}$ at the selected damping level (Figure 3.6a) as well as the RER values for the spectra of $\boldsymbol{G}_{P0}$ and $\boldsymbol{G}_{PX}$ (Figure 3.6b) are identical. This explains why the negligence of the cross-sensitivity has no effect on the results of Model-1. In the case of Model-2, the RER values of the Jacobian matrices $\boldsymbol{G}_{A0}$ and $\boldsymbol{G}_{AX}$ at the selected damping level (Figure 3.6c) showed considerable differences. The RER value of $\boldsymbol{G}_{AX}$ was about 1.5 times larger than the RER value of $\boldsymbol{G}_{A0}$, which indicates that the information in the cross-sensitivity contributed significantly to the inversion of the electrical conductivity amplitude. Figure 3.6d shows that the RER values of the Jacobian matrices $\boldsymbol{G}_{P0}$ and $\boldsymbol{G}_{PX}$ for Model-2 were identical. However, the calculation of $\boldsymbol{G}_{P0}$ also requires a reliable model for the electrical conductivity amplitude, which in the case of large phase angle can only be obtained by considering both the real part sensitivity and the cross-sensitivity in the inversion. It is then inevitable to consider the cross-sensitivity in the inversion.

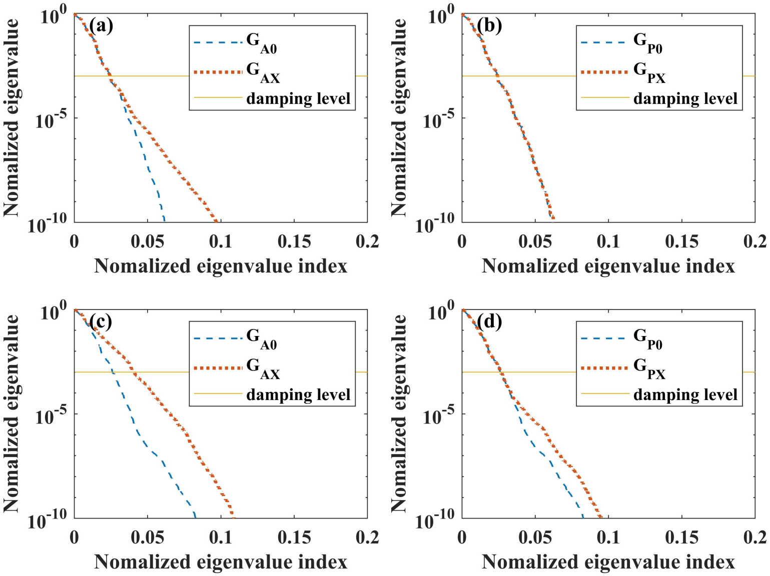

Figure 3.6: (a) Eigenvalue spectrums of the amplitude and (b) phase of electrical conductivity for Model-1 and (c) the amplitude and (d) phase of electrical conductivity for Model-2.

Finally, the model updates calculated using the Jacobian with and without cross-sensitivity were presented in Figure 3.7. The model update considering the cross-sensitivity was obtained using the CVI+ strategy. The model update calculated without cross-sensitivity was also based on the CVI+ formulation, but the off-diagonal positions in the extended Jacobian matrix were set to zero. Figure 3.7a shows the amplitude of the electrical conductivity obtained using the CVI+ strategy in the first iteration. Although the calculation was based on the logarithmic model parameter, the results in the linear space were shown to be consistent with the presentation of the true model. The electrical conductivity distribution in Figure 3.7a shows that a slightly higher conductivity layer starts to appear in the image. Figure 3.7b and 3.7c present the calculated model update in the second iteration without and with the consideration of the cross-sensitivity, respectively. The model update calculated without cross-sensitivity tends to enhance the conductive layer that appeared in the first iteration, which leads the model far from a homogeneous distribution for the electrical conductivity amplitude. In contrast, the model update calculated with cross-sensitivity updates the model towards a homogenous distribution. This highlights the unique contribution of the cross-sensitivity during the inversion.

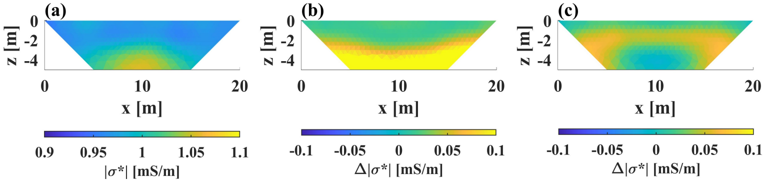

Figure 3.7: (a) Electrical conductivity amplitude obtained using CVI+ in the first iteration, (b) calculated model update without consideration of cross-sensitivity, (c) calculated model update with consideration of cross-sensitivity.

3.3.4 Inversion results for field measurements

In addition to the synthetic modelling study, two field datasets were also used to compare the inversion strategies. The first dataset is the Lozzolo dataset measured at 6 Hz where electromagnetic coupling effects can be neglected (*Zimmermann et al.*, 2019). The data error was estimated from normal and reciprocal measurements using a multi-bin approach (*Koestel et al.*, 2008) to fit the error models, as proposed by *Flores Orozco et al.* (2012b). For this, the dataset was divided into 10 equally sized logarithmic bins. The standard deviation of the normal and reciprocal errors and the mean value of the impedance amplitude in each bin were calculated and used to obtain the error parameters by fitting the corresponding error model (Figure 3.8). This resulted in 0.1% relative error and 0.014 Ω absolute error for the amplitude of measured impedance. A relative error of 0.5% was also added to the amplitude to account for modelling error. The estimated phase error using an inverse power-law model exhibited a coefficient of 0.354 mrad and the exponent of -0.454. The estimated error for both the amplitude and the phase of measured impedance were in a reasonable range and similar to other studies (*Koestel et al.*, 2008; *Kelter et al.*, 2018). The second field dataset is the Selhausen dataset. The presented data from the Selhausen site was measured at 1 Hz where the electromagnetic coupling effects can be neglected. The data error for the Selhausen dataset follows the analysis of *Weigand et al.* (2022), who determined error estimates based on a systematic parameter search.

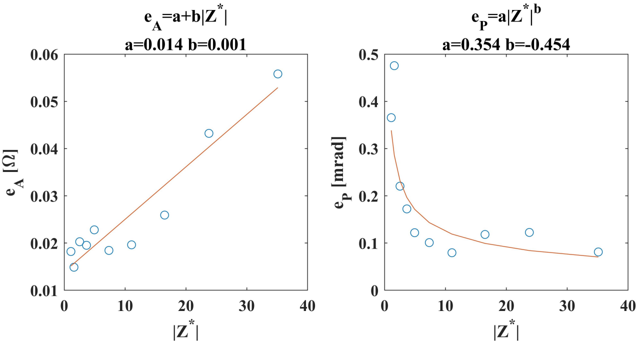

Figure 3.8: Error estimation for the amplitude of measured impedance (left-hand panel) and phase angle (right-hand panel) of the Lozzolo dataset.

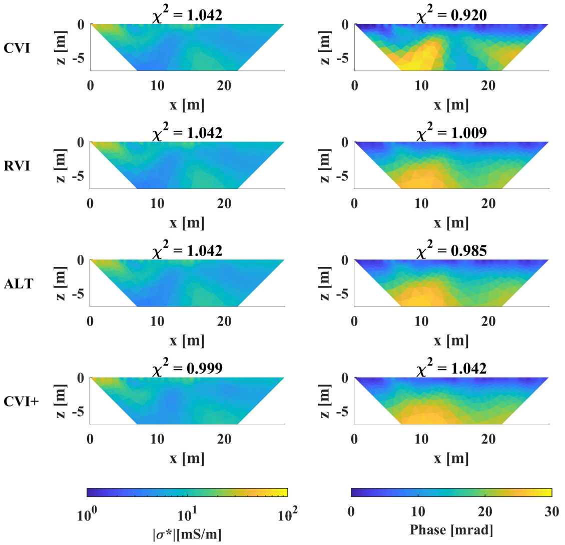

Figure 3.9: Inversion results obtained by different strategies for the Lozzolo dataset using the CVI (direct complex inversion), RVI (two-step real-valued inversion), ALT (alternate inversion or final phase improvement), and CVI+ (improved complex inversion) strategies.

Figure 3.9 shows the inversion results for the Lozzolo dataset. The inverted electrical conductivity amplitudes obtained with the four inversion strategies were similar with conductivity values mostly between 2 mS/m to 50 mS/m. Similar patterns could be observed in the inverted phase distributions. There was a weakly polarized layer near the surface and higher phase angles around 20 mrad appeared below this first layer. The inverted phase distribution obtained by the CVI method was again rougher than the other distributions and presented minor artifacts near the surface, which is due to the regularization factor as in the synthetic modelling study. Figure 3.10 shows the inversion results for the Selhausen dataset. The inverted electrical conductivity amplitude presented a very thin layer at the top with low conductivity, while the overall electrical conductivity values were at a high level of about 100 mS/m. As in the previous example, the inversion results for the electrical conductivity amplitude were similar for all inversion strategies. The inverted phase distributions produced by the RVI, ALT and CVI+ strategies were smooth and similar, while the phase distribution obtained by the CVI strategy showed extensive areas with erratic phase values in the profile. This is because the applied regularization factor is much smaller compared to the synthetic cases and the Lozzolo dataset. If the mean value of the individual data weights is used to represent the data weighting term, this is further supported by the ratio of the final regularization factor and the data weighting as in the synthetic study. This ratio was only two orders of magnitude smaller for the CVI strategy compared to the other two strategies for the Lozzolo dataset, which explains why the observed differences were relatively small. The ratio was four orders of magnitude smaller for the Selhausen dataset, which explains the erratic inversion results for the phase distribution. Overall, the results of the two field datasets showed good agreement with the synthetic modelling study in the case of small phase angles. Field measurements with large phase angles are rare and not available in this study.

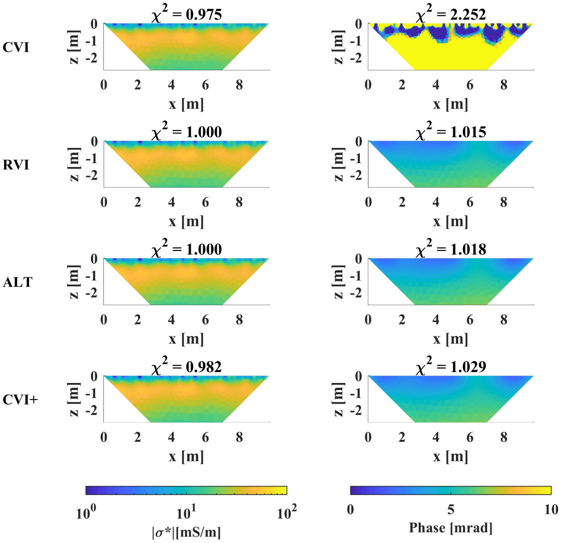

Figure 3.10: Inversion results obtained by different strategies for the Lozzolo dataset using the CVI (direct complex inversion), RVI (two-step real-valued inversion), ALT (alternate inversion or final phase improvement), and CVI+ (improved complex inversion) strategies.

3.4 Conclusions

Four strategies for EIT data inversion were compared in this chapter. The first strategy (CVI) is a complex-valued approach that follows the formulation for ERT inversion but the parameters are all complex. The second strategy (RVI) is a two-step real-valued approach where the amplitude of data is inverted first in the real number domain using the ERT inversion routine, and the phase is then separately inverted using the final real-valued Jacobian from the first step. The third strategy (ALT) in case of small phase values is similar to the two-step RVI approach but considers complex forward modelling in the second step. In the case of large phase values, the ALT strategy updates the real and imaginary parts of the model alternately so that the real part of the forward response can also be calculated based on the complex model. The fourth strategy (CVI+) is a newly formulated complex approach. Instead of using complex data and model vectors, the CVI+ strategy separates the real and imaging parts of the data and model vectors, which allows to consider the complex coupling while allowing separate data weighting and model regularization for the real and imaginary parts. Different inversion strategies were tested using two synthetic models. Model-1 represents an environmental application with small phase angles. The inverted amplitude of the electrical conductivity showed comparable images with the true model for all strategies. The inverted phase distribution obtained by the CVI strategy showed anomalies, while the inverted phase distributions obtained by the RVI, ALT, and CVI+ strategies were similar and in good agreement with the true model. The rough phase model obtained by the CVI strategy was attributed to the domination of the real part of the data and model in the inversion, which results in much smaller regularization strength for the inversion of the phase angle. It was concluded that the RVI, ALT and CVI+ strategies were all able to provide reliable inversion results in the absence of small measured phase values.

The performance of the four inversion strategies in the presence of high phase values was evaluated using Model-2, which has extremely large phase angles. For this model, only the CVI+ strategy produced plausible inversion results that were in good agreement with the true model. The reason for the failure of the CVI strategy was again related to the aggregated formulation, although the objective function was dominated by the phase angle in the case of Model-2. The failure of the RVI strategy was attributed to errors in the amplitude of the modelled data when not considering complex forward modelling, which was visualized and clearly explained by the pseudo-section of the amplitude of the modelled electrical conductivity. The ALT strategy also failed to produce reliable inversion results in the case of Model-2, which was attributed to the negligence of the cross-sensitivity in the inversion. The relative eigenvalue range was used to evaluate the information content provided by the cross-sensitivity. It was found that the RER value of the Jacobian considering the cross-sensitivity was much higher compared to the Jacobian without cross-sensitivity in the inversion of the amplitude of complex impedances, which indicates that the cross-sensitivity provided unique information in the inversion. This was supported by the calculated model update using different Jacobian matrices.

It should be noted that the RVI strategy has its practical advantage that no complex calculations are required, which substantially reduces the computation load. Therefore, it can be concluded that the CVI+ strategy is theoretically the most comprehensive and correct approach for EIT data inversion, but that in the case of small phase angles the RVI strategy should be preferred given its fast calculation and low storage requirement. In the remainder of this thesis, RVI will be adopted for data inversion since no extremely high phase values appeared in the field measurements.

Chapter 4

Experimental design to reduce inductive coupling in sEIT measurements

4.1 Introduction

In this chapter[1], inductive coupling in sEIT measurements will be investigated for two different cable layouts. One is a fan-shaped layout proposed by *Zimmermann et al.* (2019), where the electrodes are connected to the system using individual coaxial cables. This obviously leads to a larger separation between electrical wires compared to multicore cables and allows to accurately calculate the mutual inductance from the known cable geometry and thus to correct EIT measurements for inductive coupling. However, the fan-shaped layout may be complex to arrange in the field and requires more space than the use of multicore cables. *Dahlin and Leroux* (2012) proposed a dual-spread cable layout where cables for current injection and potential measurements are separated to reduce capacitive coupling between cables. Such a cable layout is also of interest to reduce inductive coupling since inductive coupling decreases with increasing separation between cables for current and potential measurements. In a first step, a novel measure will be proposed to assess the inductive coupling strength of a given electrode and cable configuration. This measure of coupling strength will also be used as a filter that selects data with limited inductive coupling. The inductive coupling strength of fan-shaped and parallel cable layouts and different electrode configurations will be evaluated for different homogeneous subsurface models. A detailed analysis and investigation will be presented to compare the fan-shaped and parallel cable layouts, demonstrating their ability to acquire measurements with low inductive coupling strength. In a second step, a sequence of electrode configurations with negligible inductive coupling will be identified using the proposed filter, and a synthetic model study will be used to illustrate the usefulness of the proposed filter. In a final step, the novel filtering approach will be applied to actual surface sEIT measurements.

---

[1] This chapter is adapted from a journal article published as: Wang, H., Huisman, J. A., Zimmermann, E., and Vereecken, H. (2021). Experimental design to reduce inductive coupling in spectral electrical impedance tomography (sEIT) measurements. Geophysical Journal International, 225(1), 222-235. https://doi.org/10.1093/gji/ggaa594

4.2 Materials and methods

4.2.1 Inductive coupling strength (ICS)

The measured mutual impedance between two grounded wires is given by *Sunde* (1968):

$$Z_m = \int_{C1}^{C2} \int_{P1}^{P2} \left[\frac{\partial^2 Q(r)}{\partial \overrightarrow{s}\, \overrightarrow{S}} + P(r) \right] d\overrightarrow{s}\, d\overrightarrow{S} \tag{4.1}$$

where $Q(r)$ describes the response from the soil, $P(r)$ is the inductive contribution, $d\overrightarrow{s}$ and $d\overrightarrow{S}$ are the discretized elements in the current and potential paths, respectively (Figure 4.1), and r is the distance between the two discretized elements. For a homogeneous subsurface model, $P(r)$ is given by:

$$P(r) = \frac{i\mu\omega}{2\pi r} \left[\frac{1-(1+\eta r)e^{-\eta r}}{(\eta r)^2} \right] \tag{4.2}$$

where i is the imaginary unit, μ is the magnetic permeability ($4\pi \times 10^{-7} H/m$), ω is the angular frequency, and $\eta = (i\sigma^* \mu\omega)^{0.5}$ is the eddy current constant. In the case of small electrode layouts, the effect of eddy currents can be neglected (*Wait*, 1984; *Zhao et al.*, 2013, 2015), which leads to the following simplification:

$$P(r) = \frac{i\mu\omega}{4\pi r} \tag{4.3}$$

which depends only on the measurement frequency and cable geometry. Using this simplification, the inductive term in Equation 4.1 can be considered as a frequency dependent mutual inductance and can be written as:

$$Z_m = Z_0 + i\omega M = Z_0' + iZ_0'' + i\omega M \tag{4.4}$$

where Z_0 corresponds to $Q(r)$ and is the noise-free complex impedance, Z_0' and Z_0'' are the real and imaginary part of the noise-free impedance, and M is the mutual inductance between cables used for current injection and potential measurements. This mutual inductance can be calculated by a Neumann's integral (*Henke*, 2011):

$$M = \frac{\mu}{4\pi} \int_{C1}^{C2} \int_{P1}^{P2} \frac{d\overrightarrow{s} d\overrightarrow{S}}{r} \tag{4.5}$$

Equation 4.4 shows that inductive coupling only affects the imaginary part of the complex impedance. Therefore, an index is proposed to quantify the inductive coupling strength ICS (in %) of each measurement:

$$\text{ICS} = 100 \times \left| \frac{\omega M}{Z_0''} \right| (\%) \tag{4.6}$$

where the imaginary part of the impedance Z_0'' for a homogeneous subsurface can be calculated by

$$Z_0'' = -\frac{sin(\varphi)}{K|\sigma^*|} \tag{4.7}$$

where $|\sigma^*|$ is the magnitude of the subsurface conductivity, φ is the phase angle at the frequency selected to evaluate M, and K is the geometric factor of the measurement configuration being considered, which depends only on the electrode positions. Low ICS values are desirable for sEIT measurements because it implies that the contribution of the inductive coupling to the measured imaginary part of the complex impedance is small. From Equations 4.6 and 4.7, it can be seen that the ICS value depends on the measurement frequency, the geometry of the cable layout, soil properties and the geometric factor of the measurement configuration.

4.2.2 Cable layouts

As discussed above, the cable layout directly influences the mutual inductance. In this chapter, analysis was focused on a 29 m long electrode array with 30 electrodes with 1 m

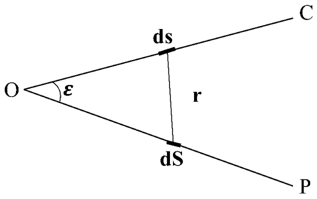

Figure 4.1: Layout of two straight grounded wires connected to the system at position O in a horizontal plane (C is the current electrode and P is the potential electrode).

electrode spacing. Two cable layouts were considered. The first layout is the fan-shaped layout (Figure 2.7) that was used in *Zimmermann et al.* (2019) for surface sEIT data acquisition. In this layout, each electrode is connected to the system with an individual straight electrical wire and the distance from the system to the mid-point of the survey line is 5 m. The second layout consists of two parallel multicore cables that allow making measurements where wires for current and potential measurements are separated. The distance between the two cables is 2 m and the distance along the x-axis from the system to the first electrode is 1 m (Figure 4.2a). For illustrative purposes, the internal wire structure of the multicore cables is assumed to be the same as that of the borehole logging cable presented in *Zhao et al.* (2013) (Figure 4.2b). This cable has 16 wires that are twisted inside. However, they were assumed to be straight in this study to simplify the calculations. All odd-numbered electrodes were connected to one cable and all even-numbered electrodes were connected to the second cable (Figure 4.2a). In detail, electrode 1 was connected to wire 1 of the first cable, electrode 2 was connected to wire 1 of the second cable, electrode 3 was connected to wire 2 of the first cable, etc. With these assumptions, the mutual inductance between any two wires can easily be calculated using Equation 4.5. As illustrated in Chapter 2, the comprehensive dataset including all three types of configuration will be considered.

In order to illustrate the value of analyzing the ICS, two homogeneous models were used to evaluate the two cable layouts for all possible electrode configurations. Model-1 has a conductivity magnitude of 4 mS/m and a phase angle of 5 mrad, whereas Model-2 has a conductivity magnitude of 40 mS/m and a phase angle of 5 mrad. A frequency of 1 kHz was used in the following analysis because this frequency has been used as a high-

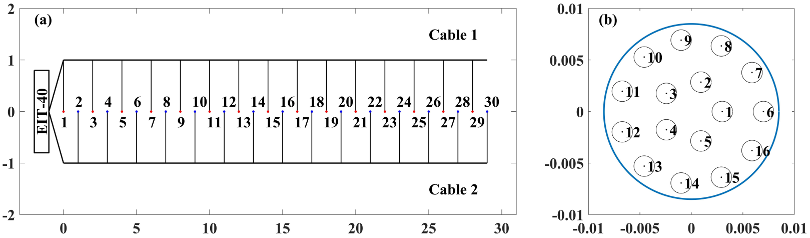

Figure 4.2: (a) Geometry of parallel cables; and (b) cross-section of multicore cable.

frequency limit in previous studies dealing with the correction of inductive coupling (*Zhao et al.*, 2013, 2015).

4.2.3 Synthetic modelling experiment

A synthetic modelling experiment was used to evaluate whether the ICS can be used to select electrode configurations that allow to image the subsurface complex conductivity distribution without data correction for inductive coupling. The 2D subsurface model for the synthetic modelling study is presented in Figure 4.3. A survey line with 30 electrodes with 1 m electrode spacing was again used. Two anomalies with 5 m length and 2 m depth were introduced in the subsurface. The center of the first anomaly is located at x = 9.5 m and z = -3 m, and the center of the second anomaly is located at x = 19.5 m and z = -4 m. These two anomalies have a conductivity magnitude of 10 mS/m and a phase angle of 40 mrad. The background conductivity magnitude and phase angle are 30 mS/m and 5 mrad, respectively.

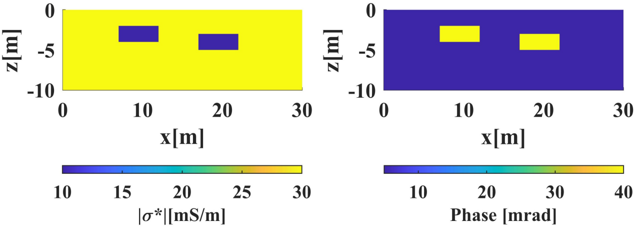

Figure 4.3: Subsurface model used in the synthetic modelling experiments.

To demonstrate the usefulness of the ICS for data filtering, a commonly used conventional dipole-dipole data acquisition strategy was compared with ICS-filtered configurations. The dipole-dipole data acquisition contains 1061 electrode configurations and used a maximum dipole length of 5 m and a maximum dipole separation of 6 m. In a first step, the simulated impedances for the synthetic modelling experiment were contaminated by 3% relative noise for the amplitude and 1 mrad random noise for the phase angle. In a second step, the inductive coupling was simulated by calculating the mutual inductance for each electrode configuration using the known cable layout and added to the simulated impedance using Equation 4.4. Data with random noise and added inductive coupling will be referred to as raw data in the synthetic experiment. In total, four different datasets were compared: (1) Raw dipole-dipole data without correction for inductive coupling, (2) dipole-dipole data corrected for inductive coupling, (3) Raw data of ICS-filtered arrays without correction for inductive coupling, and (4) ICS-filtered arrays corrected for inductive coupling.

4.2.4 Analysis of Lozollo dataset

For the analysis of the field dataset, it is not possible to use the same ICS-filtered electrode configurations used in the synthetic study because the latter were selected from the comprehensive set of 82215 configurations. As illustrated in Chapter 2, the four-pole dataset that can reliably be reconstructed from the selected current injections for the field measurements has 11340 data points. Based on the inversion results of *Zimmermann et al.* (2019), the calculation of the ICS was repeated for a homogeneous model with a conductivity magnitude of 10 mS/m and a phase angle of 30 mrad for the 11340 four-pole configurations. The selected ICS-filtered dataset will be compared with a so-called complete dataset that has been presented in *Zimmermann et al.* (2019), which will be referred to as the EZ dataset in the following. In particular, they used electrode configurations with equal separation for current injection and potential measurements, which resulted in a total of 810 data points. After filtering for geometric factors larger than 1000, 792 configurations remained for data inversion. In total, four different datasets were compared in the evaluation of the field data: (1) EZ arrays without correction for inductive coupling (EZ), (2) EZ arrays corrected for inductive coupling (EZ-C), (3) 5% ICS-filtered arrays without correction for inductive coupling (ICS5), (4) 5% ICS-filtered arrays corrected for inductive coupling (ICS5-C).

4.3 Results and discussion

4.3.1 Evaluation of ICS for fan-shaped layout

To illustrate how the choice of electrode configuration influences the ICS, detailed results for Model-2 (40 mS/m with phase shift of 5 mrad) for some specific configurations of the fan-shaped cable layout are presented in Table 4.1. For the configuration [1, 30, 2, 29] where the loop for the cables used for the potential measurements almost completely overlaps the loop of the cables for current injection, the mutual inductance M is very high. Even though the geometric factor is low, the resulting high ICS value of 491% indicates that the contribution of inductive coupling to the measured imaginary part of the impedance is almost five times larger than the actual imaginary part of the impedance. The configuration [2, 1, 29, 30] has a large separation between the cables used for current injection and potential measurements, which leads to a much lower mutual inductance compared to measurements with the electrode configuration [1, 30, 2, 29]. However, the geometric factor is high and thus the ICS value is still high. The electrode configuration [3, 13, 12, 21] is the one with the lowest ICS value among all possible 82215 configurations. For this electrode configuration, the loop of the cables used for current injection only has a small overlapping area with the loop of the potential cables, which resulted in a very low value for the mutual inductance. In addition, the geometric factor is also small, thus resulting in a very low ICS value. The smaller M for electrode configuration [3, 13, 12, 21] compared to the M of electrode configuration [2, 1, 29, 30] highlights the complexity of the mutual inductance variations in the fan-shaped layout, which is related to both the wire length and the angle between the wires. Although evident from Equation 4.6 and 4.7, it is important to stress here that a small mutual inductance is not sufficient to ensure a small effect of inductive coupling on the measured impedance.

In a next step, Figure 4.4 presents the amount of configurations with an ICS below a given threshold for the fan-shaped layout for two subsurface models with a low (Model-1, 4 mS/m) and high (Model-2, 40 mS/m) conductivity magnitude and a phase shift of 5 mrad. For both subsurface models, the amount of configurations gradually increases with an increasing threshold ICS value. In addition, Model-1 always has more configurations than Model-2 at a given threshold ICS value. Only 15% of the 82215 possible electrode configurations have an ICS above 100% for Model-1. In contrast, 75% of the possible electrode configurations have an ICS above 100% for Model-2. In the case of Model-2

Table 4.1: Mutual inductance, geometric factor and ICS values for three selected electrode configurations for Model-2 using the fan-shaped layout with 30 electrodes and 1 m electrode spacing.

$[\mathrm{C1}, \mathrm{C2}, \mathrm{P1}, \mathrm{P2}]$	M (Henry)	K (m)	ICS (%)
$[1, 30, 2, 29]$	3.0×10^{-5}	3.26×10^{0}	4.91×10^{2}
$[2, 1, 29, 30]$	3.3×10^{-9}	6.90×10^{4}	1.13×10^{3}
$[3, 13, 12, 21]$	1.3×10^{-11}	7.67×10^{0}	5.10×10^{-4}

with a high conductivity magnitude and thus a low imaginary part of the impedance in Equation 4.6, the ICS for a certain configuration is always higher in Model-2, which leads to fewer configurations with low ICS for Model-2.

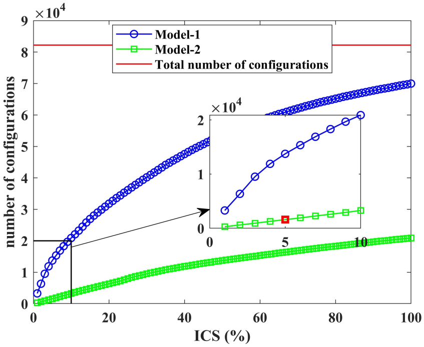

Figure 4.4: Number of electrode configurations below a given ICS value for fan-shaped layout (30 electrodes with 1 m electrode spacing) for two subsurface models. The red horizontal line indicates the total number of configurations.

Assuming that an ICS value below 5% is acceptable for sEIT inversion without data correction for inductive coupling, there are 1596 possible electrical configurations (982 β type and 614 γ type) for Model-2 with a high conductivity magnitude (red point in the zoom panel in Figure 4.4). Model-2 can be considered as a worst-case scenario since configurations with a low ICS for Model-2 also have a low ICS for subsurface materials with lower conductivity and higher phase angle. The configurations with an ICS below 5% for Model-2 all have a geometric factor below 4500 and 98% of the configurations have a geometric factor below 1000. This ensures that reliable potential measurements can actually be made in field conditions (*Stummer et al.*, 2004; *Wilkinson et al.*, 2006b; *Loke et al.*, 2010).

From a close inspection of Equation 4.6 and 4.7, it can be seen that the rank of a particular electrode configuration only depends on the multiplication of the mutual inductance M and the geometric factor K. Therefore, it is interesting to evaluate the ICS value of the electrode configuration with rank 1596 (i.e. the 5% threshold for Model-2) as a function of conductivity magnitude and phase angle (Figure 4.5). For weakly polarizable subsurface materials with a phase angle of 1 mrad, the electrode configuration with rank 1596 only has an ICS value of 5% or lower when the conductivity magnitude is lower than 8 mS/m. Therefore, accurate sEIT measurements that do not need correction for inductive coupling are difficult to obtain for highly conductive but weakly polarizable subsurface materials. For subsurface materials with a higher phase angle of 5 or 10 mrad, the electrode configuration with rank 1596 has an ICS value below 5% even in conductive environments with a conductivity magnitude of 40 mS/m or lower. It is important to realize that these results are only valid for relatively short survey lines with 30 electrodes and 1 m electrode spacing where the cables are arranged using a fan-shaped layout with 5 m distance from the system to the line.

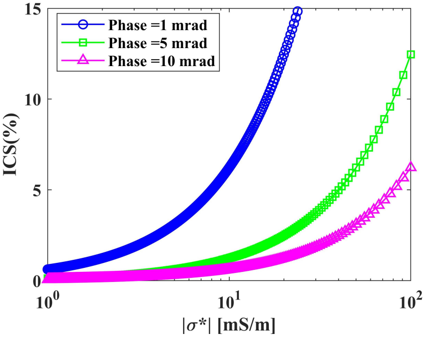

Figure 4.5: ICS values of the rank 1596 configuration for different subsurface conductivity magnitude and phase angle for the fan-shaped cable layout with 30 electrodes and 1 m electrode spacing.

Figure 4.6 shows the amount of configurations with an ICS value below a given threshold separately for α, β and γ type electrode configurations for the fan-shaped layout and Model-2 only. The total amount of configurations is 27405 for each of the three types. It can be seen that the β type configuration always has the most configurations with an ICS value below a given threshold followed by the γ type configuration. The α type configuration has the least amount of electrode configurations for a given threshold. This is due to the high M values associated with the α type configurations where the cables for the potential measurements form a loop inside the cable loop for the current electrodes. For the fan-shaped layout with the subsurface properties of Model-2 and a frequency of 1 kHz, 98% of the α type arrays have an ICS value over 100%. This clearly suggests that surface sEIT measurements with this type of electrode configuration should be avoided when a fan-shaped layout is used.

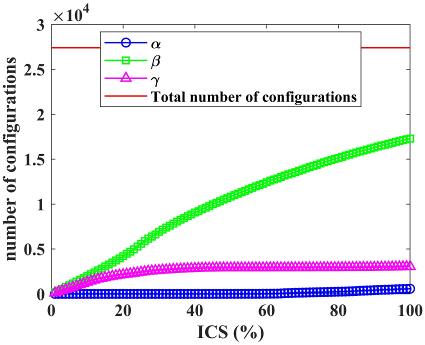

Figure 4.6: Number of electrode configurations below a given ICS value for α, β and γ type configurations for Model-2 using a fan-shaped layout with 30 electrodes and 1 m electrode spacing.

The sensitivity of the ICS values to small changes in the position of the EIT system (and thus the cable positioning) for the fan-shaped layout was also evaluated. For this, all electrode configurations with an ICS less than 5% (Model-2 at 1 kHz) were selected for a system positioned 5.0 m away from the survey line. Next, the ICS values for these electrode configurations were calculated for a system moved 0.1 m in all four directions (i.e. left, right, towards, and away from the survey line). When the system was moved towards or away from the survey line, more than 90% of the configurations still had an ICS below 5%. The remaining 10% of the configurations had ICS values ranging from 5% to 7.5%, which is still relatively low. When the system was moved to the left or right, more than 80% of the configurations still showed ICS values below 5% and the remaining configurations also showed ICS values ranging from 5% to 7.5%. Therefore, it was concluded that configurations with a low ICS are not sensitive to small positional errors in the cable layout for the fan-shaped layout.

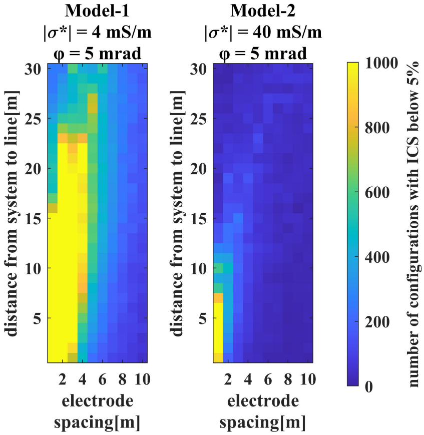

Figure 4.7: Number of configurations with ICS below 5 per cent for a fan-shaped layout with different separation between the EIT system and the survey line and different electrode spacings for a survey line with 30 electrodes for Model-1 (left-hand panel) and Model-2 (right-hand panel).

To illustrate the applicability of the proposed filtering method for larger electrode spacings and layouts, a survey line with 30 electrodes with different electrode spacing ranging from 1 m to 10 m was investigated (i.e. survey line lengths ranging from 29 m to 290 m). In addition, different distances from the system to the survey line were considered. In this investigation, the inductive term in Equation 4.1 was calculated using the full equation $P(r)$ (Equation 4.2), which resulted in a complex inductive term. The influence of inductive coupling on the real part of the measured impedance was evaluated, and was found to be small and was thus neglected. Therefore, only the imaginary part of the complex inductive term was taken into account to calculate the ICS values. Figure 4.7 presents the number of configurations with an ICS below 5% as a function of electrode spacing and distance to survey line. Assuming that 1000 configurations are required to image the subsurface, it can be concluded that the proposed filtering method is restricted to small layouts in the case of conductive and weakly polarizable subsurface environments (Model-2). In the case of more resistive and highly polarizable subsurface environments (Model-1), the proposed filtering method can be applied to larger layouts up to an electrode spacing of 4 m. Overall, the applicability of the proposed method for a given application should be evaluated based on the exact layout and proper subsurface information given the strong dependence on the subsurface properties.

4.3.2 Evaluation of ICS for parallel cable layout

Figure 4.8 shows the amount of configurations with an ICS value below a given threshold for the parallel cable layout (Figure 4.2a) for the two subsurface models. It is clear that the parallel cable layout always has less arrays for a certain threshold ICS value than the fan-shaped layout (Figure 4.4). There are only 276 electrode configurations with an ICS below 5% for Model-2, which suggests that the fan-shaped layout has considerably more potential to provide sEIT measurements with acceptable ICS values. The main reason for the higher ICS values for the parallel cable layout is the small separation between the wires compared to the fan-shaped layout. In particular, the wire separation inside the cables is in the millimeter range and the separation between the cables is only 2 m, which results in high M values.

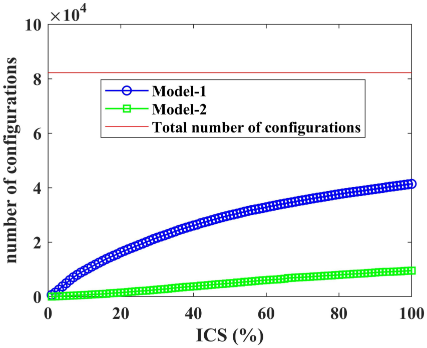

Figure 4.8: Number of electrode configurations below a given ICS value for parallel cable layout for two subsurface models.

For the parallel cable layout, it is especially interesting to analyze the configurations with

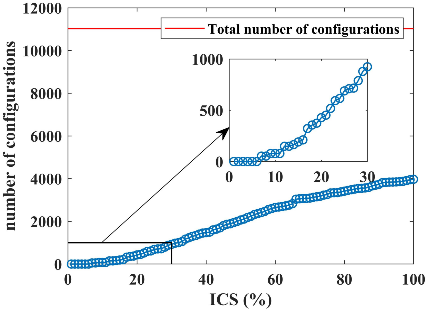

Figure 4.9: Number of configurations below a given ICS value for configurations with separated transmitter and receiver cables for Model-2.

separated current injection and potential measurements (i.e. wires for current injection in cable 1 and wires for potential measurements in cable 2 or vice versa). Such measurements were suggested by *Dahlin and Leroux* (2012) to reduce the capacitive coupling between cables. In total, there are 11025 out of a possible 82215 electrode configurations that have separated cables for current injection and potential measurements. Figure 4.9 shows the amount of electrode configurations with an ICS value below a given threshold for these configurations for the more challenging Model-2 only. It can be seen that most configurations have a high ICS value and that the lowest ICS value is 6.2%. The lowest ICS values are associated with current dipoles with small separations. In this case, the mutual inductance between the two current and potential wires almost cancel each other. EIT measurements with a large separation between electrodes (e.g. electrodes 1 and 29 for current injection and electrodes 2 and 30 for potential measurement) will lead to a high mutual inductance because of the considerable extra length of one current wire between electrodes 1 and 29 that is not compensated by the second current wire. In addition, the cable separation of 2 m is relatively low compared to many of the separations obtained with the fan-shaped layout.

In the case of separated current and potential cables in the parallel cable layout, larger cable separations could be helpful to obtain more configurations with low ICS. To investigate this, mutual inductances and ICS values were calculated for different cable separations ranging from 1 m to 10 m at 1 kHz using Model-2. Figure 4.10 shows that the number of configurations with an ICS below 5% increased with increasing cable separation for both the comprehensive dataset and the reduced dataset with separated wires for current and potential measurements. Even for the large cable separation of 10 m, there are only 1200 configurations for the comprehensive dataset and only 880 configurations for the reduced dataset with an ICS value below 5%. This clearly highlights that it is difficult to obtain sufficient measurements with low contributions of inductive coupling for the parallel cable layout. Moreover, a large cable separation of 10 m also requires long additional cables to connect the electrodes to the multi-core cables. In fact, the benefits of the parallel cable layout relative to the fan-shaped layout in terms of handling in the field are not existent anymore for connecting cables with a length of 10 m.

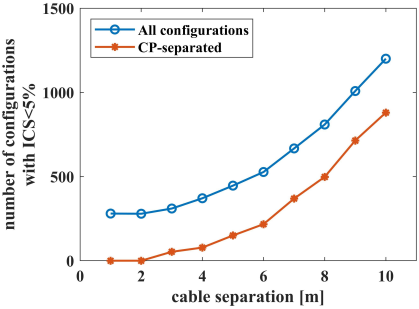

Figure 4.10: Number of configurations with ICS below 5 per cent for the parallel cable layout as a function of cable separations for Model-2 for both the comprehensive dataset and the reduced dataset with wires for current and potential measurements in separate cables (CP-separated).

To better understand how the increase in cable separation affects the mutual inductance and the inductive coupling strength, it is useful to separate the mutual inductance M into a horizontal part Mh and a vertical part Mv. In Figure 4.11, the current and potential wires for a certain electrode configuration are shown. The mutual inductance M was first calculated for the full path (C1-system-C2; P1-system-P2). Next, the horizontal part Mh was calculated using the path without the four connection wires (i.e. C1*-system-C2*; P1*-system-P2*). It was found that Mh will often be dominated by the horizontal wire segments between the electrodes (bold lines between C1* and C2*, and between P1* and P2*) because the inductive coupling introduced by the other segments typically cancels each other out because the current is flowing in both directions. Since the angle between these two horizontal wire segments is always 0°, Mh is always positive. The difference between M and Mh is the contribution of the four connection wires, and is called Mv in the following. Mv consists of four parts: M_{AM}, M_{AN}, M_{BM}, and M_{BN}, which are the mutual inductances between wires C1C1* and P1P1*, C1C1* and P2P2*, C2C2* and P1P1*, and C2C2* and P2P2*, respectively. In the current setup, M_{AM} and M_{BN} are always negative and M_{BM} and M_{AN} are always positive. Because of the complexity in the superposition, Mv can be positive or negative depending on the configuration.

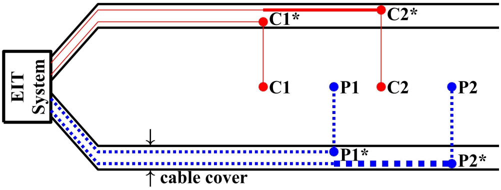

Figure 4.11: Schematic illustration showing the separation of the mutual inductance in several parts for configurations with wires for current and potential measurements in separate cables.

An analysis of M, Mh, and Mv for three representative configurations is presented in Figure 4.12. The first column presents results for the configuration [1 29 2 28]. This configuration has a long dipole length for both current and potential pairs. The ICS value of this configuration decreases with increasing cable separation because of the decreasing mutual inductance M. For this configuration, M is dominated by Mh, which is mainly determined by the contribution of the current wire between electrodes 1 and 29 and the potential wire between electrodes 2 and 28. In this case, the contribution from Mv relative to Mh is small. The Mv for this configuration is negative because the distances between C1C1* and P1P1* and between C2C2* and P2P2* are small. With increasing cable separation, the distance between the dominant wires increases while the length remains the same, which results in a decrease of Mh and M and thus ICS. The second column presents results for configuration [25 27 4 6]. For this configuration, the wire segments between C1* and C2* and electrodes P1* and P2* are short and the distance between them is high. Therefore, M is much smaller than for the first configuration. The ICS value increases with increasing cable separation and is still dominated by the contribution from Mh. However, the change in Mh with increasing cable separation is more complex. Mh first increases and then decreases with increasing separation. The Mv is positive for this configuration. The increase in Mv with increasing cable separation is larger than the decrease in Mh, which results in an increasing M and ICS with increasing separation. The third column presents results for the configuration [1 5 2 6], which also has a short wire segment between the two current and the potential electrodes. However, the distance between the two extra wire segments is now small. In this case, the ICS value first decreases up to a cable separation of 6 m, and then starts to increase. Mh decreases with increasing cable separation for this configuration, but the absolute value of Mv increases (i.e. it becomes more negative). Again, the negative Mv is due to the small distances between C1C1* and P1P1* and between C2C2* and P2P2*. In this case, M turns from positive to negative and the ICS increases again because it is calculated from the absolute value of the mutual inductance (see Equation 4.6).

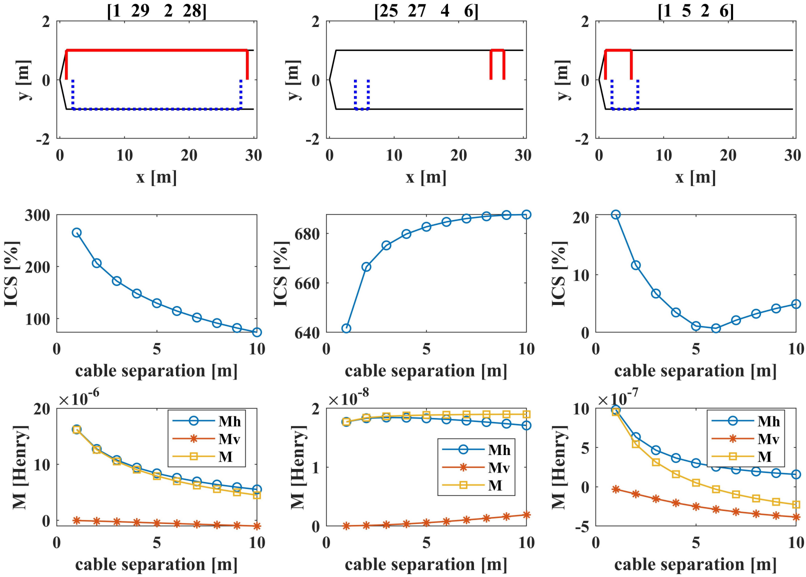

Figure 4.12: Contribution of horizontal and vertical cable segments (Mh and Mv) on mutual inductance M and inductive coupling strength ICS as a function of cable separation for three representative electrode configurations.

Based on the detailed analyses above, it can be concluded that a larger cable separation still did not result in a sufficient amount of electrode configurations with low ICS. Therefore, sEIT measurements with parallel multicore cables cannot reliably be used without correction of inductive coupling effects unless measurements are made with sufficiently low frequency to ensure negligible inductive coupling. In the remainder of this chapter, the parallel cable layout is not considered anymore.

4.3.3 Synthetic model study

Figure 4.13 compares the inversion results of the synthetic modelling experiments for conductivity amplitude and phase angle for different datasets using the fan-shaped cable layout. The second row (DD-C) presents the inversion results at 1 kHz for dipole-dipole measurements that have been corrected for inductive coupling. The results of DD-C should thus be considered as the reference here. In the first row (DD), inversion results at 1 kHz are presented for the same set of dipole-dipole measurements that were not corrected for inductive coupling. As was already shown by *Kelter et al.* (2018) and *Zimmermann et al.* (2019), the magnitude of the inverted complex conductivity is not affected by inductive coupling, but the inverted phase angle at 1 kHz is erroneous if inductive coupling is not removed before inversion. The third row (ICS5) shows the inversion results of ICS-filtered arrays with inductive coupling. The anomalies in the results of ICS5 are as well resolved as in the reference case DD-C, which indicates that the ICS-filtered arrays can provide reliable inversion results without data correction. The fourth row (ICS5-C) presents inversion results for the same 1596 electrode configurations as in ICS5 after removing inductive coupling. This resulted in almost identical inversion results as in ICS5, which suggests that a threshold of 5% for the ICS-filter is acceptable. Overall, the results of this synthetic model study support the idea that it is possible to obtain reliable inversion results without corrections for inductive coupling if data are filtered based on the ICS value in case of relatively small electrode layouts and a fan-shaped cable layout.

Figure 4.14 presents the resolution (Equation 2.21) of the conventional dipole-dipole arrays and the ICS-filtered arrays. The ICS-filtered arrays are the 1596 arrays obtained for Model-2 (worst case scenario) using a threshold ICS value of 5%. As expected, the resolution decreases with depth in both cases. Although the ICS-filtered array showed a lower resolution in the deeper subsurface compared to the dipole-dipole array, the resolution maps for both dipole-dipole arrays and the ICS-filtered arrays show a similar distribution. This suggests that the ICS-filtered arrays have the potential to adequately resolve the subsurface complex conductivity distribution.

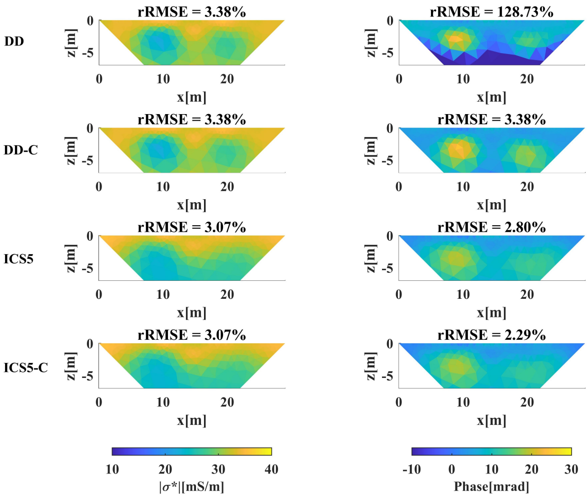

Figure 4.13: Inversion results for synthetic datasets: DD. Raw data of dipole–dipole array without correction for inductive coupling; DD-C. DD with correction for inductive coupling; ICS5. Raw data of 5 per cent ICS-filtered array without correction for inductive coupling; ICS5-C. ICS5 with correction for inductive coupling.

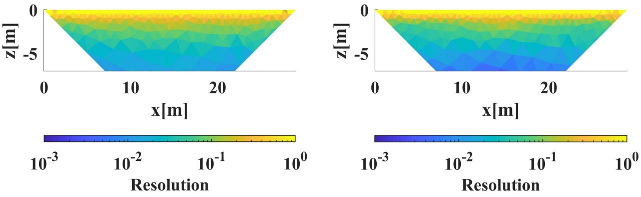

Figure 4.14: Resolution of configuration dipole–dipole (left-hand panel) and 5 per cent ICS-filtered arrays (right-hand panel).

4.3.4 Field example

The inversion results for the field sEIT measurements are presented in Figure 4.15. The inverted conductivity magnitude is shown for 6.1 Hz only since the magnitude is almost independent of frequency, and the phase of the complex conductivity is shown for three selected frequencies (6.1 Hz, 71.4 Hz, 1950 Hz). The first and second row show the results for the electrode configurations used in *Zimmermann et al.* (2019) without (EZ) and with (EZ-C) correction for inductive coupling, respectively. It can be seen that the correction for inductive coupling has a considerable effect on the inverted phase values at 1950 Hz, but that the inverted phase distributions at 6.1 Hz and 71.4 Hz are not strongly affected. After correction for inductive coupling, the results for the phase angle show better spectral consistency. The relative RMS error for the phase result produced by EZ-C dataset at 1950 Hz is still high, which is due to the extremely high ICS values for EZ configuration and will be discussed in more detail in the following.

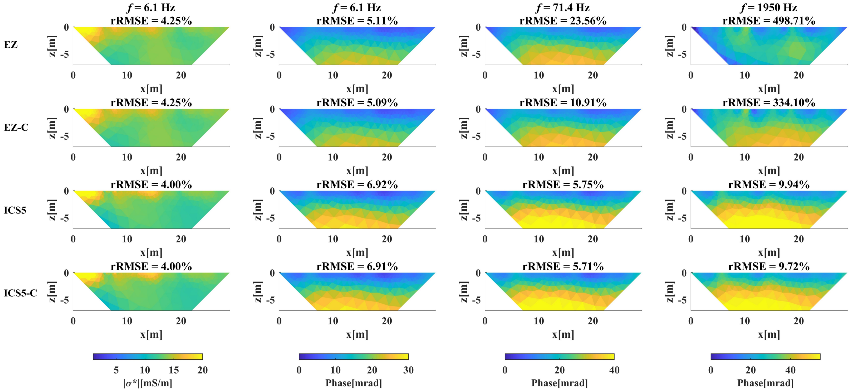

Figure 4.15: Inversion results for field datasets: EZ. EZ arrays without correction for inductive coupling; EZ-C. EZ configurations corrected for inductive coupling; ICS5. 5 per cent ICS-filtered arrays without correction for inductive coupling; ICS5-C. 5 per cent ICS-filtered arrays corrected for inductive coupling.

The amount of electrode configurations below a given ICS value for the 11340 possible configurations in this field example is shown in Figure 4.16. These ICS values were calculated using a homogeneous model with conductivity magnitude of 10 mS/m and a phase angle of 30 mrad at 1950 Hz based on the inversion results presented in *Zimmermann et al.* (2019). About 85% of the 11340 configurations have an ICS value below 100%. Using a 5% threshold (red point in the zoom panel in Figure 4.16) for the ICS again, there are 1418 electrode configurations that can be used for inversion. The results for these ICS-filtered arrays without and with corrections for inductive coupling are presented in the last two rows in Figure 4.15. In contrast to the uncorrected results for the EZ dataset at 1950 Hz, the inversion results obtained with the filtered configurations without correction for inductive coupling (ICS5) show no signs of inductive coupling and good spectral consistency. Comparing the results of EZ-C and ICS5, they show good agreement on the main characteristics for both conductivity magnitude and phase spectrum although some minor differences can also be observed. The inversion results obtained with the filtered electrode configurations after correction for inductive coupling (ICS5-C) are almost identical to the inversion results without correction (ICS5) even at the highest frequency of 1950 Hz. As was already shown in the synthetic model experiment, this suggests that the small amount of inductive coupling remaining in the selected electrode configurations after filtering does not substantially affect the inversion results. The resolution maps of both the EZ configurations and the ICS-filtered configurations are presented in Figure 4.17. The two resolution maps show a similar distribution and similar values at depth, which again confirms that the ICS-filtered configurations have the potential to image the subsurface complex conductivity.

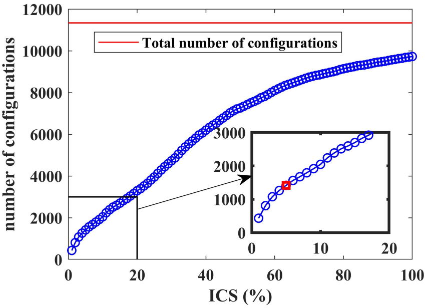

Figure 4.16: Number of electrode configurations below a given ICS value for the field measurement configurations.

The difference between the inversion results of the EZ-C and ICS5 datasets, especially at the highest frequency, can be attributed to the high ICS values for some measurements in the EZ datasets. It is important to realize that the inversion results for the EZ-C dataset should not be considered as the reference in this analysis. In order to illustrate this, the phase angle and the imaginary part of the measured impedance at 1950 Hz are presented in Figure 4.18 for all four datasets. It can be seen that the phase of the measurements in the uncorrected EZ dataset shows physically implausible negative values. The imaginary part of the impedance also shows some positive values. After correction, the phase of some measurements in the EZ-C dataset still show erratic values. An analysis of the ICS values associated with these outliers showed that they all have very high ICS values (>400%). In contrast, the phase values for the ICS5 dataset are all in a smaller range between 11 and 45 mrad and the imaginary impedances are all negative as expected. This highlights that some of the electrode configurations used in *Zimmermann et al.* (2019) may not have been accurately corrected for inductive coupling, and that this likely also affected the inversion results for the EZ-C dataset.

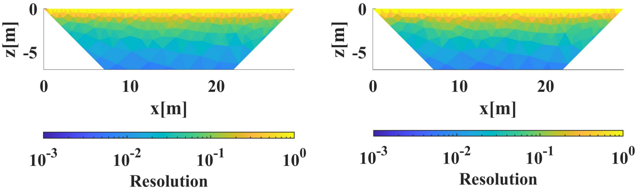

Figure 4.17: Resolution of EZ (left-hand panel) and ICS5 (right-hand panel) arrays.

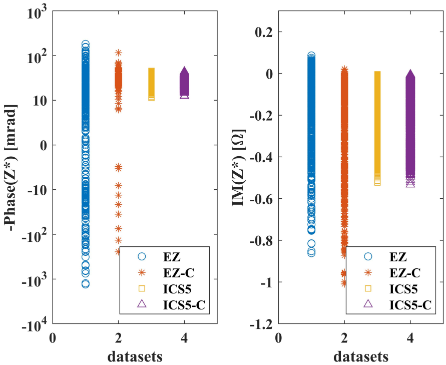

Figure 4.18: Phase angle (left-hand panel) and imaginary part (right-hand panel) of complex impedance for four different datasets.

4.4 Conclusions

A new index called inductive coupling strength (ICS) was proposed to quantify the effect of inductive coupling between cables on sEIT measurements. In a first step, the ICS was evaluated for different subsurface properties, cable layouts and electrode configurations for a short electrode layout with 30 electrodes and 1 m electrode spacing. With a fan-shaped cable layout, results for different subsurface properties showed that accurate sEIT measurements that do not need correction for inductive coupling are difficult to obtain for highly conductive but weakly polarizable subsurface materials. It was also shown that configurations with low ICS in the fan-shaped layout are not sensitive to small errors in cable position, which is advantageous for field handling. The analysis of different types of electrode configurations showed that the widely used α type electrode configurations have a much higher ICS than other types of electrode configurations when using a fan-shaped cable layout. Based on the analysis of ICS values for different cable layouts, it was also found that a fan-shaped cable layout should be preferred over more commonly used layouts with parallel multicore cables if corrections for inductive coupling are not envisioned. The feasibility of applying to large cable layout was also discussed. It was shown that it is very challenging to acquire enough measurements with low ICS values for layout with several hundred meters long survey line. However, the applicability of the proposed filtering method should be carefully evaluated based on the exact layout and reliable prior information about the subsurface complex conductivity given the strong dependence of the ICS on the subsurface properties, and thus a reliable correction for inductive coupling may be applied in terms of large scale survey. In a second step, a synthetic model study using the same fan-shaped cable layout was presented. Here, a set of electrode configurations was selected using 5% as a threshold for the ICS value. Next, these ICS-filtered measurements were inverted to compare the inversion results with reference datasets. The results showed that it is possible to conduct inversion without data correction by applying the fan-shaped layout and a filter based on ICS in the case of the relatively short electrode layout considered in this study. In a third and final step, actual field sEIT measurements with the same setup as used in the synthetic model study were analyzed. The inversion results for the field data further validated the proposed idea of using ICS to select data with negligible inductive coupling. It was also shown that electrode configurations with high ICS should be filtered out even when sEIT measurements have been corrected for inductive coupling in order to avoid unreliable corrections.

Chapter 5

Reduction of capacitive coupling in broadband sEIT measurements

5.1 Introduction

In this chapter [1], the capacitive coupling in sEIT measurements will be investigated in more detail. Capacitive coupling usually refers to the leakage of electric current through possible capacitances wherever a potential difference exists. There are mainly three types of sources in sEIT measurements: coupling between the cables, coupling between the ground and electrodes and coupling between the ground and cables (*Radić*, 2004; *Dahlin and Leroux*, 2012; *Zhao et al.*, 2013). The first type of capacitive coupling is usually the most important one when using non-shielded multicore cables. With the use of shielded cables, the capacitive coupling between cables can be significantly reduced (*Flores Orozco et al.*, 2012a; *Zhao*, 2017; *Flores Orozco et al.*, 2021). A remaining source of capacitive coupling when using shielded cables is the capacitance between the inner wire and the shield, which can be eliminated by using so-called active electrodes (i.e. amplifiers mounted at the electrodes) as in *Zimmermann et al.* (2010). The second type of capacitive coupling between the ground and electrodes is associated with the contact impedance and the internal electronics in the amplifier (i.e. the input capacitance). *Kelter et al.* (2015) and *Huisman et al.* (2016) have presented methods to estimate the contact impedance and correct the induced error at the field and laboratory scale, respectively. With the use of active electrodes, the input capacitance for voltage measurement can be largely reduced to 5 pF (*Zimmermann et al.*, 2008a), which can be further corrected by implementing this capacitance at the electrodes in the forward modelling (*Zimmermann et al.*, 2019). With all these advanced improvements, the first two types of capacitive coupling can be suppressed to a large extent. The remaining main source of capacitive coupling then becomes the capacitive coupling between the cable shield and the ground (*Zhao et al.*, 2013, 2015; *Zimmermann et al.*, 2019).

---

[1] This chapter is adapted from a manuscript submitted to Geophysical Journal International: Wang, H., Huisman, J. A., Zimmermann, E., and Vereecken, H. Reduction of capacitive coupling in broadband sEIT measurements

In the case of conductive soil, the applied electric current preferentially flows through the soil, which leads to insignificant capacitive coupling as is the case in Chapter 4. In a resistive environment, the capacitive coupling becomes more pronounced. *Zimmermann et al.* (2019) demonstrated improvements in the imaging results by considering the capacitance and leakage current in the FEM forward modelling during inversion. However, the results were only partly satisfactory at the highest frequency and limited to a so-called complete configuration. Following the idea in Chapter 4 to deal with inductive coupling, the aim of this study is to improve the accuracy of sEIT inversion results in a broad frequency range by identifying and filtering out measurements that are strongly affected by capacitive coupling. In a first step, a new strategy to model the impedances induced by capacitive coupling will be presented. A novel index to quantify the capacity coupling strength (CCS) will then be proposed. The capacitive coupling strength of all possible electrode configurations will then be examined assuming that only capacitive coupling needs to be considered and that other sources of measurement error are of secondary importance. In a final step, electrode configurations with low capacitive coupling strength will be selected for inversion of sEIT data and the results will be compared to inversion results obtained using the complete configuration considered in *Zimmermann et al.* (2019).

5.2 Materials and methods

5.2.1 Conceptual model

As introduced in Chapter 1 and the introduction above, the investigation of capacitive coupling in this thesis is focused on the capacitance between ground and cable shield. *Wang and Slater* (2019) dealt with the leakage current and corrected the associated capacitive coupling in laboratory four-point SIP measurements using a simplified electric circuit model, which requires many additional measurements and can not be easily extended to deal with capacitive coupling in field sEIT measurements. This is also related to the heterogeneous conductivity distribution in field conditions as compared to a small and typically rather homogeneous sample column. Figure 5.1 shows a schematic illustration of capacitive coupling between ground and cable shield. The injected current flows from the positive current electrode C+ to the ground and back to the system through two different paths. The first path is the desirable path through the negative current electrode C- (green path). The second path is the leakage currents through the capacitance between ground and cable shield (red path). It is clear from the schematic illustration that the paths of the leakage current can be very complicated. It can flow through the capacitance to the system ground and then from the system ground back to soil. In contrast to *Wang and Slater* (2019) where the exact current flowing through the target sample segment can be determined, the symmetric current and leakage current coexist everywhere within the survey area in the case of field measurements. This indicates that dealing with capacitive coupling at the field scale requires a more comprehensive model including the information about the subsurface heterogeneity, the capacitance between cable shield and ground, and the leakage current. This information can be obtained by prior analysis of the measurements, which will be introduced in detail next.

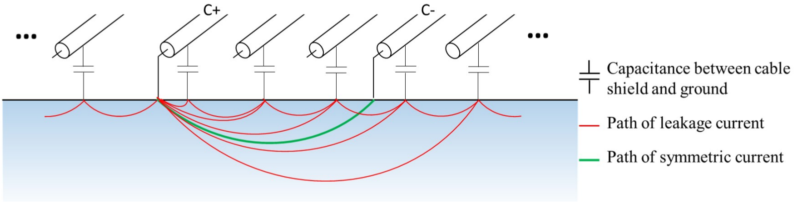
C+
C-
...
...
Capacitance between cable shield and ground
Path of leakage current
Path of symmetric current

Figure 5.1: Schematic illustrating capacitive coupling between ground and cable shield, modified after *Zimmermann et al.* (2019).

5.2.2 Normalized leakage current and the total capacitance

As introduced in Chapter 2, the system measures the excitation current at both current channels and the symmetric current I_s and leakage current I_L can then be calculated using Equation 2.24 and 2.25. The normalized leakage current nLS is defined as the ratio of the leakage current and the symmetric current expressed as a percentage,

$$nLS = 100 \times \frac{I_L}{I_s} (\%) \tag{5.1}$$

The real part of the normalized leakage current reflects the loss in the real part of the injected currents I_1 and I_2, whereas the imaginary part of the normalized leakage current indicates how large the phase shift between the excitation currents is. Usually, the real part of the normalized leakage current is much smaller than the imaginary part because capacitive coupling mainly induces a phase shift in the applied currents. The absolute value of the normalized leakage current as used in *Zimmermann et al.* (2019) represents the total loss in the injected currents.

To obtain the total capacitance between the cable shield and the ground, additional measurements with single pole excitation were conducted in *Zimmermann et al.* (2019). In particular, a current I_i was injected at one electrode and the potential measurements U_p were carried out at all other electrodes relative to system ground. The total capacitance C_T can then be calculated using:

$$i2\pi f C_T = \frac{I_i}{mean(U_p)} \tag{5.2}$$

Where i is the imaginary unit, f is the measurement frequency. To achieve high accuracy of the estimated total capacitance, the same procedure to estimate the total capacitance was repeated at each electrode and the mean value of all estimated total capacitances was then used. The idea behind estimating the total capacitance with Equation 5.2 is to obtain the applied current and voltage that act on the capacitances. In this thesis, an alternative approach to directly derive the total capacitance from field sEIT measurements was used. In particular, the leakage current I_L and voltages U_p for each current injection were used to determine the total capacitance using Equation 5.2 without the need for additional measurements. This is possible since the leakage currents through the capacitances and the potentials relative to the system ground are also available for regular sEIT measurements.

5.2.3 Decoupling of capacitive coupling

The forward problem in the EIT method is to solve Equation 2.8. The matrices form of Equation 2.8 can be written as

$$\boldsymbol{Y}^{*}\boldsymbol{U}^{*} = \boldsymbol{I}_{s} \tag{5.3}$$

where $\boldsymbol{Y}^{*}$ is a sparse matrix containing the information of the complex conductivity distribution, $\boldsymbol{U}^{*}$ is the complex potential vector to be solved, and $\boldsymbol{I}_s$ is the applied symmetric unit current. Considering the real and imaginary components of $\boldsymbol{Y}^{*}$ and $\boldsymbol{U}^{*}$, Equation 5.3 can be written as

$$(\boldsymbol{Y}_s' + i\boldsymbol{Y}_s'')(\boldsymbol{U}' + i\boldsymbol{U}_s'') = \boldsymbol{I}_s \tag{5.4}$$

where $\boldsymbol{Y}_s'$ and $\boldsymbol{Y}_s''$ represent the real and imaginary parts of the electrical conductivity distribution of the subsurface, $\boldsymbol{U}'$ is the real part of the electrical potential, and $\boldsymbol{U}_s''$ is the imaginary part of the electrical potential due to polarization of the materials. Since the applied symmetric unit current $\boldsymbol{I}_s$ is real-valued, the imaginary terms in the left-hand side of Equation 5.4 should cancel each other, and the following relations can be obtained:

$$\boldsymbol{Y}_s'\boldsymbol{U}' - \boldsymbol{Y}_s''\boldsymbol{U}_s'' = \boldsymbol{I}_s \tag{5.5}$$

and

$$\boldsymbol{Y}_s'\boldsymbol{U}_s'' + \boldsymbol{Y}_s''\boldsymbol{U}' = 0 \tag{5.6}$$

The second term $\boldsymbol{Y}_s''\boldsymbol{U}_s''$ in the left-hand side of Equation 5.5 is negligible for near surface applications with small phase angles below 200 mrad (*Johnson and Thomle*, 2018), which means that the real part of the electrical potential field mainly depends on the real part of the complex conductivity distribution and is largely independent of the imaginary part of the subsurface electrical conductivity. Equation 5.6 illustrates that the imaginary part of the potential field ($\boldsymbol{U}_s''$) is determined by the real part of the potential field acting on the imaginary part of the electrical conductivity distribution. It should be noted that the relation shown in Equation 5.6 is independent of boundary conditions.

Zimmermann et al. (2019) proposed to consider both the capacitances and leakage currents in the forward model used for inversion to remove the effect of capacitive coupling. In particular, the total estimated capacitance between the cable shield and the ground was distributed along the known positions of the cables in the 3D forward model. In addition, the leakage current can be integrated in the modelling by using the two measured excitation currents I_1 and I_2 for the current term instead of the unit symmetric current. Ignoring the influence of capacitive coupling on the measured real part of the complex impedance, the real part of the current term can be simply considered as the symmetric part of the current and the imaginary part represents the leakage current in the modelling. Taking the capacitances and leakage currents into account, Equation 5.4 can then be extended as

$$(\boldsymbol{Y}_s' + i\boldsymbol{Y}_s'' + i\boldsymbol{Y}_c'')(\boldsymbol{U}' + i\boldsymbol{U}_s'' + i\boldsymbol{U}_c'') = \boldsymbol{I}_s + i\boldsymbol{I}_L \tag{5.7}$$

where $\boldsymbol{Y}_c''$ is a diagonal matrix containing information on the distributed capacitances, and $\boldsymbol{U}_c''$ is the imaginary part of the potential distribution induced by capacitive coupling. Since $\boldsymbol{I}_s$ is real-valued, the imaginary terms in the left-hand side of Equation 5.7 should be equal to the leakage current:

$$\boldsymbol{Y}_s'\boldsymbol{U}_s'' + \boldsymbol{Y}_s''\boldsymbol{U}' + \boldsymbol{Y}_s'\boldsymbol{U}_c'' + \boldsymbol{Y}_c''\boldsymbol{U}' = \boldsymbol{I}_L \tag{5.8}$$

Using Equation 5.6, Equation 5.8 can be further reduced to:

$$\boldsymbol{Y}_s'\boldsymbol{U}_c'' + \boldsymbol{Y}_c''\boldsymbol{U}' = \boldsymbol{I}_L \tag{5.9}$$

Equation 5.9 clearly shows that the imaginary part of the electrical potential due to capacitive coupling $\boldsymbol{U}_c''$ depends on the real part of the electrical conductivity, the resulting real part of the electrical potential distribution, the capacitances and the leakage currents. Therefore, $\boldsymbol{U}_c''$ can be obtained by solving

$$(\boldsymbol{Y}_s' + i\boldsymbol{Y}_c'')(\boldsymbol{U}' + i\boldsymbol{U}_c'') = \boldsymbol{I}_s + i\boldsymbol{I}_L \tag{5.10}$$

without considering the imaginary part of the electrical conductivity distribution. To ensure that all leakage currents flow through the distributed capacitances, a Neumann (no-flow) boundary condition was applied to all the surrounding boundaries and the subsurface boundaries were put sufficiently far away from the survey area of interest. One problem of using pure Neumann boundary condition is that the admittance matrix ($\boldsymbol{Y}_s'$) is singular.

However, this problem is solved with the consideration of the distributed capacitances ($\boldsymbol{Y}_s' + i\boldsymbol{Y}_c''$).

5.2.4 Capacitive coupling strength

Assuming that all other sources of measurement error are negligible and only capacitive coupling needs to be considered for the imaginary part of measured impedance, the measured complex impedance Z_m can be written as

$$Z_m = Z_0 + iZ_c'' = Z_0' + iZ_0'' + iZ_c'' \tag{5.11}$$

where Z_0 is the noise-free impedance, Z_0' is the real part of the measured impedance, Z_0'' is the imaginary part of the impedance due to polarization of the subsurface, and Z_c'' is the imaginary part of the impedance induced by capacitive coupling. The capacitive coupling strength CCS (in percentage) for a measurement with a given electrode configuration can now be defined as:

$$\mathrm{CCS} = 100 \times \left| \frac{Z_c''}{Z_0''} \right| (\%) \tag{5.12}$$

A small CCS value indicates that the contribution of capacitive coupling to the measured impedance is low, which is desirable for sEIT measurements. However, it is difficult to infer which type of configuration is more sensitive to capacitive coupling a priori because the influence of capacitive coupling depends on the distribution of the real part of the electrical conductivity and the resulting potential distribution, which are heterogeneous and unknown a priori. Therefore, CCS values for different electrode configurations are not general and vary for each survey. They should be analyzed on a case by case basis using the actual on-site sEIT measurements.

Figure 5.2 illustrates the workflow to calculate the CCS. Based on the decoupling approach described above, the distribution of the real part of the electrical conductivity must be obtained first in order to calculate Z_c'' from the FEM modelling. In the first step, the real part of the impedances are therefore inverted to obtain the 2D electrical conductivity distribution. In a second step, the 2D distribution is mapped to a 3D model. It should be noted that the total capacitance is distributed homogeneously along the cable layout in the 3D model and the corresponding nodes of the capacitances were defined in the 3D model with 0.3 m spacing for generating the grid. In a third step, the 3D FEM modelling is performed by solving Equation 5.10 to obtain Z_c''. In the final step, the CCS values of all measurements are calculated using Equation 5.12. According to this workflow, it should be noted that the measured data can also be corrected for capacitive coupling by removing Z_c'' from the measurements.

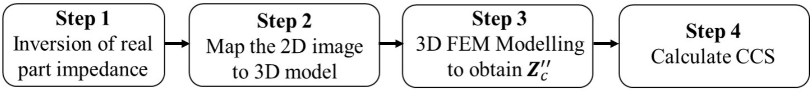
Step 1
Inversion of real part impedance
Step 2
Map the 2D image to 3D model
Step 3
3D FEM Modelling to obtain Z_c''
Step 4
Calculate CCS

Figure 5.2: Workflow to calculate the capacitive coupling strength (CCS).

5.2.5 Field measurements

As illustrated in Chapter 2, a fan-shaped cable layout with 30 electrodes and 30 current injections with a scheme of skip-16 were used to obtain the Senna Lodigiana dataset. In the end, there were 11340 measurements that can potentially be reconstructed in the post-processing. Some general data filters were applied before further analysis. First, modelling accuracy was evaluated using a homogeneous model and measurement configurations with modelling error larger than 1% were removed. Then, configurations with large geometric factors were also excluded. In particular, a threshold geometric factor value of 1000 was applied for the so-called α and β types configurations and a more strict threshold value of 100 was adopted for γ type configurations. Measurements with negative apparent electrical conductivity values were also removed prior to further analysis.

5.3 Results and discussion

5.3.1 Total capacitance and leakage current

Figure 5.3(a) shows the relationship between the mean value of the recorded voltages U_p and the leakage currents I_L for all excitations at 1950 Hz, and a nearly perfect linear relation was obtained. The slope of this relationship reflects the left term in Equation 5.2, and is thus determined by the angular frequency multiplied with the total capacitance. This results in an estimated total capacitance of 10.67 nF using the actual EIT measurements, which is in good agreement with the estimated value of 10.50 nF obtained from calibration measurements in *Zimmermann et al.* (2019). This new approach was also tested with measurements at other frequencies, and the estimated total capacitances are presented in Figure 5.3(b). The estimated total capacitance decreased with increasing frequency, which is attributed to a decrease in the dielectric permittivity of the cable insulation. A similar decrease was also observed in *Zhao et al.* (2013) for the measured capacitance of multicore cable in the frequency range from 10 Hz to 10 kHz. It should be noted that the estimated total capacitance using measurements at lower frequencies is more uncertain because the leakage currents at low frequencies are much smaller. The estimates at higher frequencies where capacitive coupling is expected to affect the measurement accuracy have comparably small uncertainty and are thus more reliable. These results show that it is feasible to estimate the total capacitance from the EIT measurements directly. In the following, the estimated value of 10.67 nF at 1950 Hz was used for the total capacitance in the FEM modelling.

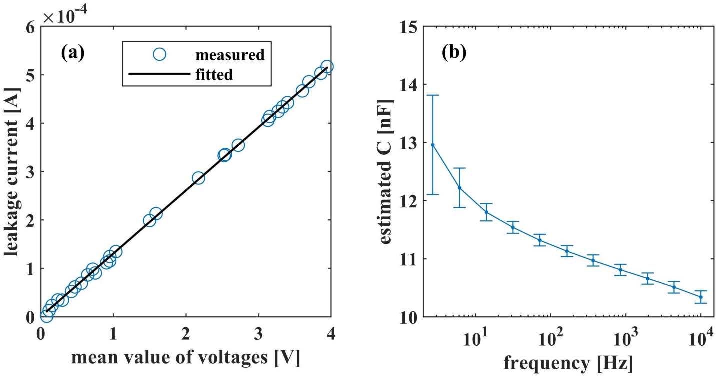

Figure 5.3: (a) Relationship between the mean value of recorded voltages U_p and the corresponding leakage current I_L for all excitations at 1950 Hz and (b) estimated total capacitances as a function of frequency.

An assumption in the proposed approach (Equation 5.10) is that the real part of the excitation current can represent the symmetric current. To evaluate this assumption, the real parts of the measured excitation currents I_1 and $-I_2$ are shown in Figure 5.4(a). It can be seen that the measured excitation currents match very well. Figure 5.4(b) shows the relationship between the real and imaginary parts of the normalized leakage current.

Again, a strong relationship is observed, which shows that the loss in the real part of the excitation currents correlates well with the imaginary part of the normalized leakage current. This indicates that the filtering of large normalized leakage currents will remove measurements with a large loss in both the real part and phase shift of the excitation currents I_1 and $-I_2$.

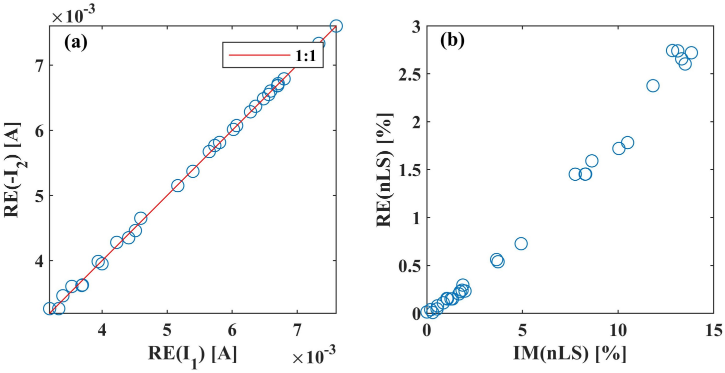

Figure 5.4: (a) Relationship between real part of the injected current I_1 and the real part of $-I_2$ at 1950 Hz and (b) the relationship between the real and imaginary part of the normalized leakage current at 1950 Hz.

5.3.2 Evaluation of CCS

Measurements at 1950 Hz were used for the analysis of the CCS. For the data acquisition strategy used here, there are 11340 measurements that can be reconstructed in post-processing. A threshold value of 10% as used in *Zimmermann et al.* (2019) for the absolute normalized leakage current was first adopted, which results in 8316 measurements (i.e. 22 current excitations) to be considered for the CCS evaluation. Additional data filtering based on modelling error, geometric factor, and negative apparent electrical conductivity values further reduced the number of measurements to 7745. Following the workflow shown in Figure 5.2, the distribution of the real part of the electrical conductivity was obtained for these 7745 measurements. The resulting 2D inversion result is presented in Figure 5.5(a), and the relative RMS error is low with 2.67%. The inverted electrical conductivity ranges from 0.1 mS/m to 10 mS/m and the distribution shows a very resistive region at the right side of the profile with an electrical conductivity below 1 mS/m. Next, the 2D inversion result was mapped to a 3D distribution shown in Figure 5.5(b) and the estimated total capacitance of 10.67 nF was distributed homogeneously along the fan-shaped cable layout. By solving Equation 5.10 for this extended 3D grid while only considering the real part of the subsurface electrical conductivity, the imaginary part of the impedance Z_c'' induced by the capacitances was obtained and used to obtain the CCS values of all 7745 measurements using Equation 5.12.

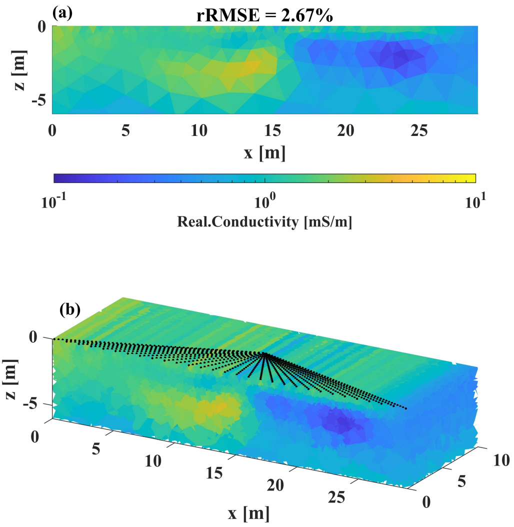

Figure 5.5: (a) 2D inversion result for the real part of the electrical conductivity; (b) 3D conductivity model with integrated capacitances (black dots).

Figure 5.6(a) shows the percentage of measurements with a CCS value above 50% as a function of the absolute normalized leakage current for each current excitation. For excitations with a normalized leakage current larger than 3%, about 80% or more of the measurements have a CCS higher than 50%. This clearly illustrates that high CCS values are more likely to occur when the normalized leakage current is large. It is also clear from Figure 5.6(a) that measurements with small normalized leakage current can nevertheless also have relatively large CCS values above 50%, which is due to the real part of the potential distribution that acts on the capacitances and induces a secondary current source term, i.e. $\boldsymbol{Y}_c''\boldsymbol{U}'$ in Equation 5.9. Although the normalized leakage current can be very small, this secondary source term applied to the electrical conductivity distribution may also result in a sufficiently high imaginary part of the potential such that the accuracy of the measured imaginary part of the impedance is noticeably affected. Based on these findings, it was decided to use a more strict threshold value of 3% for the normalized leakage current, which resulted in a reduction from 7745 to 5288 measurements.

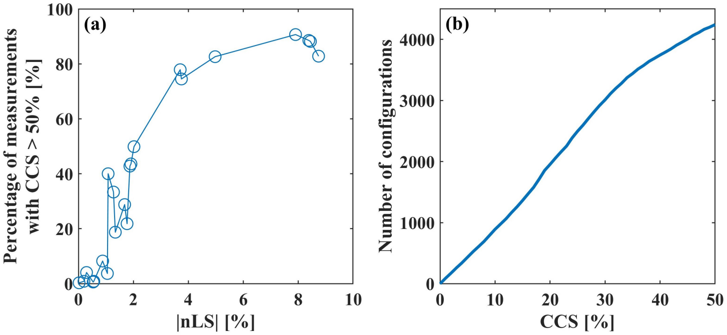

Figure 5.6: (a) Percentage of measurements with CCS > 50% as a function of the absolute normalized leakage current for the 22 selected excitations and (b) number of electrode configurations below a given CCS value in the remaining 5288 measurements after filtering.

Figure 5.6(b) shows the number of electrode configurations below a given CCS threshold value for the remaining 5288 measurements. It can be seen that there are about 4000 measurements with a CCS value below 50%, 1433 measurements with a CCS value below 15% (CCS15 dataset), and 463 measurements with a CCS value below 5% (CCS5 dataset). It is reasonable to assume that the imaginary part of the impedance induced by capacitive coupling can be neglected for the CCS5 dataset, but the number of remaining electrode configurations is low. Although the measured imaginary part of the impedance of the CCS15 dataset may need to be corrected for capacitive coupling, this dataset is expected to provide better sensitivity coverage than the small CCS5 dataset. Based on these considerations, the following datasets were considered for further analysis. First, the uncorrected measurements of the CCS5 and CCS15 datasets were analyzed (CCS5 and CCS15). Next, the CCS5 and CCS15 datasets were analyzed using the correction approach of *Zimmermann et al.* (2019) (CCS5-C and CCS15-C). As a reference, the results are compared to results obtained in *Zimmermann et al.* (2019) using a complete set of electrode configurations (*Xu and Noel*, 1993). This dataset was filtered with a threshold value of 10% for the normalized leakage current as in *Zimmermann et al.* (2019) and the general filters were also applied, which resulted in a final dataset with 544 measurements. Datasets without and with corrections (EZ and EZ-C) were considered.

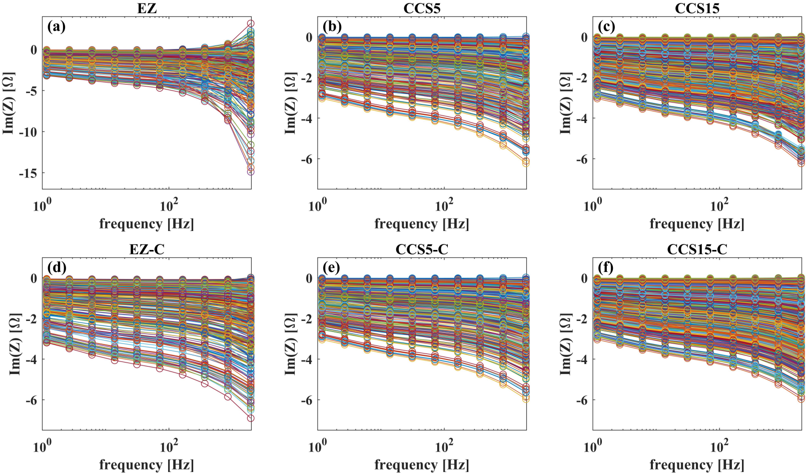

Figure 5.7: Spectra of the imaginary part of the impedance for different datasets before and after correction: (a,d) the complete datasets EZ and EZ-C, (b,e) 5% CCS-filtered datasets CCS5 and CCS5-C, (c,f) 15% CCS-filtered datasets CCS15 and CCS15-C.

Figure 5.7 shows the imaginary part of the impedances of the different datasets over a broad frequency range. The measurements of the EZ dataset (Figure 5.7(a)) are noisy and have many positive imaginary part impedances at higher frequencies. After correction for capacitive coupling, the measurements are significantly improved (Figure 5.7(d)) as already reported in Zimmermann et al. (2019). However, measurements at the highest frequency of 1950 Hz still seem to be noisy, and a small amount of measurements with positive imaginary part impedance remained. The CCS values of the EZ dataset ranged from 0.15% to about 4000%. About 20% of the measurements have a CCS value larger than 100% and about 40% of the measurements have a CCS value larger than 50%. Again, the high CCS values above 500% were associated with normalized leakage currents larger than 3%. This suggests that many measurements of the EZ dataset need considerable correction. For the CCS5 and CCS15 datasets, no apparent improvements can be identified after correction. However, the spectra of the CCS15 dataset seem to show more spectral consistency after correction.

5.3.3 Inversion results of sEIT measurements

The inversion results for the real part of the electrical conductivity distribution using different datasets were all nearly identical to the results presented in Figure 5.5(a). No differences in the inversion results were observed for the raw and corrected data. Therefore, only the results for the imaginary part of the electrical conductivity distribution are presented here (Figure 5.8) for four selected frequencies. The inversion results at 6.1 Hz and 71.4 Hz showed no apparent differences between uncorrected and corrected datasets for all considered datasets, although the relative RMS error for the EZ dataset at 71.4 Hz is slightly higher compared to other results at this frequency. At 367 Hz, the inversion result for the uncorrected EZ dataset showed different features compared to the results at lower frequencies and the relative RMS error was high. After correction, the relative RMS error was reduced considerably and the inversion result was more consistent with the results at lower frequencies. This indicates that the correction at this frequency was successful for the EZ dataset. At the highest considered frequency of 1950 Hz, the inversion result showed anomalies with unrealistically high and low values and the relative RMS error was high. Both the inversion result and the relative RMS error were improved after correction for capacitive coupling. However, the final inversion did not agree well with results at lower frequencies and the relative RMS was still high. This means that the correction of capacitive coupling improved the data quality but that not all measurements were reasonably corrected. This is attributed to several high CCS values in the EZ dataset.

The inversion results for the CCS5 dataset before and after correction showed very similar distributions of the imaginary part of the electrical conductivity and the relative RMS errors were comparably low. The results for the different frequencies showed good spectral consistency and there were no anomalies. The inversion results for the CCS15 dataset are very similar to the results produced by the CCS5 configuration even without correction for capacitive coupling. However, a decrease in the relative RMS error after correction for capacitive coupling was observed for the CCS15 dataset. Overall, the inversion results for the CCS-filtered datasets are very promising. Without correction for capacitive coupling, reliable and spectrally consistent inversion results were achieved.

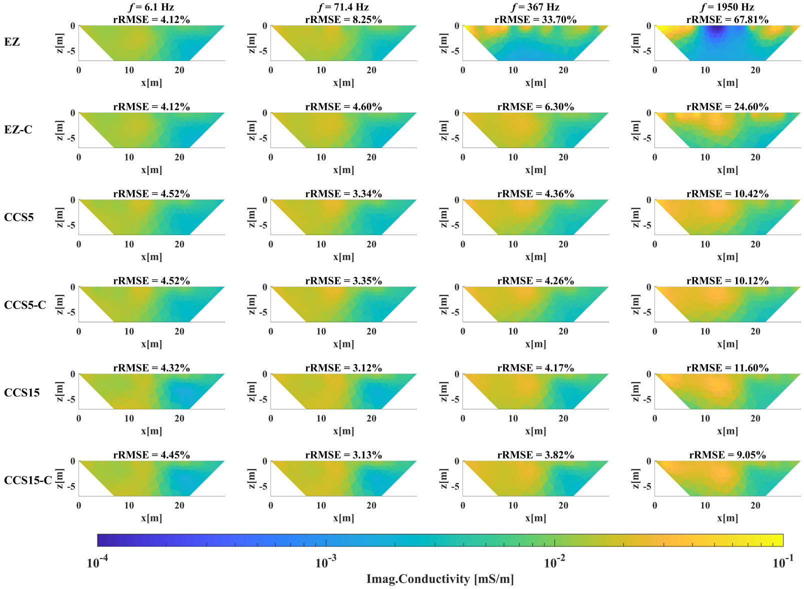

Figure 5.8: Inversion results for the imaginary part of the electrical conductivity for the following datasets: EZ: EZ configurations without correction for capacitive coupling; EZ-C: EZ configurations corrected for capacitive coupling; CCS5: CCS-filtered (5%) configurations without correction for capacitive coupling; CCS5-C: CCS-filtered (5%) configurations corrected for capacitive coupling; CCS15: CCS-filtered (15%) configurations without correction for capacitive coupling; CCS15-C: CCS-filtered (15%) configurations corrected for capacitive coupling.

Figure 5.9 presents the resolution of the different datasets based on the final conductivity model. The three datasets showed a similar resolution distribution. Considering the EZ dataset as the reference here, the ratio of the resolution of CCS5 dataset and the EZ dataset has a mean value of 0.92, indicating that the CCS5 configuration has the potential to resolve the subsurface conductivity distribution, although it has fewer data points compared to EZ configuration. This mean ratio is 1.2 for CCS15 dataset, indicating that CCS15 configuration has even better ability to capture the subsurface information compared to EZ configuration.

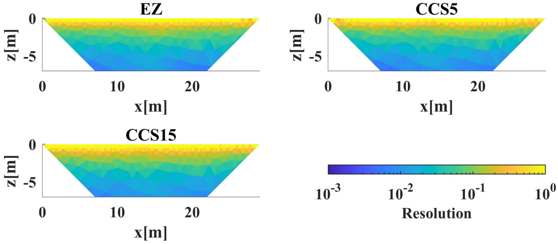

Figure 5.9: Resolution of the complete configuration EZ, 5% CCS-filtered configurations CCS5, and 15% CCS-filtered configurations CCS15.

5.4 Conclusions

A method to evaluate the capacitive coupling strength (CCS) of sEIT measurements was proposed. The CCS is defined as the ratio of the imaginary part of the impedance induced by capacitive coupling and the imaginary part of the impedance due to soil polarization. Based on an analysis of the forward modelling considering leakage currents and capacitances, it was shown that the imaginary part of the impedance due to capacitive coupling can be separately obtained without knowing the imaginary part of the electrical conductivity distribution. With the use of a customized sEIT measurement system that can measure the excitation current at both the positive and negative current electrodes, a method was proposed to derive the total capacitance directly from actual sEIT measurement instead of from previously used calibration measurements based on a single-point excitation. It was shown that the total capacitance obtained from the actual sEIT measurement was similar to the value obtained in previous work using single pole measurements.

In a next step, a workflow to calculate the CCS values for each possible measurement was proposed. For this, the measurements with large modelling error, large geometric factor, and large normalized leakage current were first filtered out. The remaining measurements after filtering were used to obtain the distribution of the real part of the electrical conductivity through inversion of the measured real part of the impedance. The obtained 2D distribution was mapped to a 3D model and the total capacitance was distributed along the cables by integrating the corresponding nodes in the 3D forward model. The FEM modelling with the real part of the electrical conductivity distribution, integrated capacitances and measured leakage currents was conducted to obtain the imaginary part of the impedance induced by capacitive coupling. Finally, the CCS values for all considered measurements were calculated by assuming that all other sources of errors are negligible. The resulting CCS values showed that high normalized leakage currents are likely to produce measurements with a high CCS, while a low normalized leakage current does not ensure a small CCS.

After the calculation of the CCS values, measurements with CCS values below 5% (CCS5) and 15% (CCS15) were selected for data inversion to obtain the imaginary part of the electrical conductivity distribution for a range of frequencies. The inversion results were compared with a complete configuration (EZ) that was considered in previous work. An analysis of the measured impedance spectra showed that significant improvements can be observed for the EZ datasets before and after correction for capacitive coupling. However, for CCS-filtered datasets, no apparent changes were observed. The inversion results for the EZ datasets showed that the correction for capacitive coupling was only partly successful, which is due to the high CCS values and large leakage current for the electrode configurations used in the EZ dataset. The inverted imaginary part of the electrical conductivity distributions obtained with the CCS-filtered datasets showed good spectral consistency before and after correction for capacitive coupling for a broad frequency range up to kHz.

Chapter 6

Conclusions and outlook

In this chapter, the conclusions of this thesis will be presented first. After this, possible directions for future research will be discussed.

6.1 Conclusions

sEIT is a promising technology to image the subsurface complex conductivity distribution in a broad frequency range from mHz to kHz, which helps to better characterize the complexity of subsurface materials and processes (*Flores Orozco et al.*, 2011; *Kemna et al.*, 2012; *Weigand and Kemna*, 2019; *Mudler et al.*, 2022). Laboratory studies have provided promising results and strongly raised interest in applications at the field scale (*Binley et al.*, 2005; *Flores Orozco et al.*, 2013; *Revil et al.*, 2017; *Mellage et al.*, 2018b). To obtain reliable imaging results over a broad frequency range, a proper inversion strategy as well as accurate measurements are both important. A range of studies in the past two decades have refined the inversion of sEIT data with a focus on simplification for efficient computation (*Johnson and Thomle*, 2018), improved forward modelling to account for all kinds of inductive coupling (*Commer et al.*, 2011), and spectrally constrained inversion (*Günther and Martin*, 2016). However, the complex nature of sEIT data inversion has never been fully considered. Moreover, the use of simplified inversion strategies relies on the small phase assumption, but extremely large phase angles have occasionally been reported (*Kulenkampff and Yaramanci*, 1993; *Peruzzo et al.*, 2021). Several studies have also addressed EM coupling effects in sEIT measurements (*Routh and Oldenburg*, 2001; *Huisman et al.*, 2016; *Zhao et al.*, 2013, 2015; *Wang and Slater*, 2019; *Wang et al.*, 2021;

Flores Orozco et al., 2021), which was an important step forward for accurate broadband sEIT measurements at both the laboratory and field scale. Although the developed correction methods for EM coupling provided promising results (*Zhao et al.*, 2013, 2015; *Zimmermann et al.*, 2019), it is still of interest to explore whether a careful selection of electrode configurations would allow to obtain reliable broadband inversion results without the need for correction of EM coupling effects. Therefore, the overall objective of this thesis was to enhance the applicability of sEIT technology at the field scale by addressing the above mentioned knowledge gaps and research questions. To address this overall objective, three sub-objective were defined.

The first sub-objective was to develop a comprehensive inversion strategy for EIT data taking into account its complex nature and incorporating separate data weighting and model regularization components, and to compare this newly formulated strategy with other available inversion strategies. To address this sub-objective, existing inversion strategies were reviewed in detail in Chapter 2, including the direct complex inversion strategy (CVI), the two-step real-valued strategy (RVI), and the alternate inversion strategy (ALT). Then, the newly formulated strategy (CVI+) was presented in Chapter 3. Instead of using complex data and model vectors, the CVI+ strategy assembles the real and imaginary part of the data and model vectors into real-valued and extended data and model vectors. This allows to consider the complex coupling while also allowing separate data weighting and model regularization for the real and imaginary parts. In a next step, the different strategies were evaluated using two synthetic models. Model-1 represents an environmental application with small phase angles, while Model-2 has extremely large phase angles for example representing a subsurface with an inclusion of rock salt. The inversion results showed that the CVI strategy is not suitable for EIT data inversion because of the aggregated formulation. In particular, it was found that the inversion using the CVI strategy is dominated by the real part of the data and model in the case of small phase angles and by the imaginary part in the presence of large phase angles. The inversion results also showed that the other three strategies provided accurate and consistent inversion results in the case of small phase angles, but in the case of large measured phase values only the newly formulated CVI+ strategy provided plausible inversion results that were in good agreement with the true model. The better performance is related to the impact of the large phase angles on the modelled amplitude of the data, which emphasized the importance of considering complex forward modelling in the case of large phase angles and explained the failure of the RVI strategy. The imaginary part of the complex sensitivity (i.e. the cross-sensitivity), which is usually ignored, was found to provide unique information during the inversion in the presence of large phase values. This finding was further supported by the analysis of the relative eigenvalue range of the different Jacobian matrices and the resulting model updates. It was concluded that the CVI+ strategy is theoretically the most comprehensive and correct approach for EIT inversion, but that in the case of small phase angles the RVI strategy has the practical advantage that no complex calculations are required, which substantially reduces the required computational effort.

The second sub-objective was to investigate whether a careful selection of electrode configurations for sEIT measurements would allow to obtain reliable broadband inversion results without the need for correction of inductive coupling. This was addressed in Chapter 4. In a first step, a new index called inductive coupling strength (ICS) was proposed to quantify the effect of inductive coupling on sEIT measurements. In a second step, the ICS was evaluated for different cable layouts, subsurface properties, and electrode configurations for a short electrode layout with 30 electrodes and 1 m electrode spacing. It was found that a fan-shaped cable layout should be preferred over more commonly used layouts with parallel multicore cables because the wire separation in the fan-shaped layout is much larger than in the multicore cables. Using a fan-shaped cable layout and considering different subsurface properties, it was shown that accurate sEIT measurements that do not need correction for inductive coupling are difficult to obtain for highly conductive but weakly polarizable subsurface materials. The analysis of different types of electrode configurations showed that the widely used α type electrode configurations have a much higher ICS than other types of electrode configurations when using a fan-shaped cable layout. In a third step, a synthetic modeling study was presented and actual field sEIT measurements were analyzed. The results of both synthetic and field datasets showed that it is possible to obtain accurate inversion results without data correction by applying the fan-shaped layout and a filter based on ICS in the case of the relatively short electrode layout considered in this study. The feasibility of using the proposed workflow to address inductive coupling in larger cable layouts was also discussed. It was shown that it is challenging to acquire a sufficient amount of measurements with low ICS values for cable layouts with an extent of several hundred of meters. However, the applicability of the proposed filtering method should be carefully evaluated based on the exact cable layout and reliable prior information about the subsurface complex conductivity given the strong dependence of the ICS on the subsurface properties. In case of favorable site conditions, the proposed method to avoid measurements with strong inductive coupling may also be applicable for large scale surveys.

The third sub-objective was to explore the possibility to obtain reliable inversion results by selecting electrode configurations that do not require correction of capacitive coupling. This was investigated in Chapter 5. Based on forward modelling considering integrated capacitances and leakage currents, an approach to model the impedances induced by capacitive coupling was proposed first. It was shown that the imaginary part of the impedance due to capacitive coupling can be separately obtained without knowledge of the imaginary part of the electrical conductivity distribution in the subsurface. In analogy to the ICS index proposed in Chapter 4, an index was proposed to evaluate the capacitive coupling strength (CCS) in sEIT measurements. The CCS index is defined as the ratio of the imaginary part of the impedance induced by capacitive coupling and the imaginary part of the impedance due to polarization processes in the subsurface. A workflow to calculate the CCS was presented. In particular, the EIT measurements were first used to obtain the subsurface distribution of the real part of the electrical conductivity. The obtained 2D distribution was mapped to a 3D model and the total capacitance between the cable shield and ground was distributed along the cables by integrating the corresponding nodes in the 3D forward model. The forward modelling with the real part of the electrical conductivity distribution, integrated capacitances and measured leakage currents was then conducted to obtain the imaginary part of the impedance induced by capacitive coupling. Finally, the CCS values for all considered measurements were calculated by assuming that all other sources of errors are negligible. The resulting CCS values showed that high normalized leakage currents are likely to produce measurements with a high CCS, while a low normalized leakage current does not ensure a small CCS value. After the calculation of the CCS values, measurements with low CCS values were selected for data inversion to obtain the imaginary part of the electrical conductivity distribution for a broad range of frequencies. The inversion results were compared with a complete configuration (EZ) that was considered in previous work (*Zimmermann et al.*, 2019). It was shown in *Zimmermann et al.* (2019) that the correction of capacitive coupling in the EZ dataset was only partly successful, which in this thesis was found to be due to the high CCS values and large leakage current for some EZ configurations. The inverted imaginary part of the electrical conductivity distribution obtained with the CCS-filtered datasets showed good spectral consistency before and after correction for capacitive coupling for a broad frequency range up to kHz.

Overall, the results presented in this thesis have largely improved the applicability of sEIT technology at the field scale. First, a newly formulated comprehensive complex inversion approach enables accurate processing of field sEIT measurements with large phase angles. Comparison of this new approach with other strategies clarified the feasibility of using simplified strategies for the inversion of sEIT measurements with small phase angles, which is the common case in the near-surface sEIT measurements. Second, the use of the proposed experimental design methods to deal with inductive coupling enables reliable inversion results in a broad frequency range up to kHz without the need for correction of inductive coupling. The proposed method can be used with any customized or commercial EIT instrument, and thus provides clear benefits for the entire community working with sEIT. Finally, the proposed method to deal with capacitive coupling together with a customized measurement system allowed to obtain plausible broadband imaging results without correction of capacitive coupling even for resistive subsurface conditions. Although this approach can only be used with customized EIT measurement systems, the results highlighted the technological improvements that are required for next generation commercial sEIT systems to address capacitive coupling.

6.2 Outlook

While this thesis provided promising improvements for both the inversion and EM coupling reduction of sEIT measurements, there still is scope for additional research. In addition, several follow-up research questions emerged from this thesis. In the following, some possible research topics related to the inversion and EM coupling reduction of sEIT measurements will be discussed.

6.2.1 Inversion

In addition to the important decisions for the formulation of the geoelectrical inverse problem discussed in Chapter 2, such as the selection of the regularization factor and step length, the type of data and model parameters used in inversion are also important to consider. In the case of ERT inversion, the data can be resistance, apparent resistivity, logarithm of the resistance or apparent resistivity. The use of a logarithmic model parameter has been widely accepted given that it scales the model parameter better and ensures positive model resistivity or conductivity (*Günther*, 2004; *Loke*, 2004). However, one can still choose between logarithmic resistivity and conductivity. Considering a same data type no matter what it is, the model roughness term for the logarithmic conductivity $\boldsymbol{\Phi}_m(ln\boldsymbol{\sigma})$ and logarithmic resistivity $\boldsymbol{\Phi}_m(ln\boldsymbol{\rho})$ are $||\boldsymbol{W}_m ln\boldsymbol{\sigma}||^2$ and $||\boldsymbol{W}_m ln\boldsymbol{\rho}||^2$, respectively. The relation between these two model roughness terms is $||\boldsymbol{W}_m ln\boldsymbol{\sigma}||^2 = ||\boldsymbol{W}_m ln\frac{1}{\boldsymbol{\rho}}||^2 = ||\boldsymbol{W}_m(0-ln\boldsymbol{\rho})||^2 = ||\boldsymbol{W}_m ln\boldsymbol{\rho}||^2$. It is clear from the equation that the model roughness term for logarithmic conductivity equals the one for logarithmic resistivity. This indicates that the choice of resistivity and conductivity in the ERT inversion does not make a difference when a logarithmic model parameter is applied. With the use of a logarithmic model parameter, the data misfit terms for the different data types in ERT inversion can be written as

$$\boldsymbol{\Phi}_d(R) = \sum_{i=1}^{N} \left| \frac{R_i - f_i(\boldsymbol{m})}{e_i} \right|^2 \tag{6.1}$$

$$\boldsymbol{\Phi}_d(\rho_a) = \sum_{i=1}^{N} \left| \frac{KR_i - Kf_i(\boldsymbol{m})}{Ke_i} \right|^2 \tag{6.2}$$

$$\boldsymbol{\Phi}_d(lnR) = \sum_{i=1}^{N} \left| \frac{lnR_i - lnf_i(\boldsymbol{m})}{ln(R+e_i) - ln(R)} \right|^2 \tag{6.3}$$

where e_i is the data error for measured resistance R_i, $f_i(\boldsymbol{m})$ is the modelled resistance for a given model m. It can be easily seen that Equation 6.2 becomes identical to Equation 6.1 after eliminating the geometric factor K. Therefore, it can be concluded that the inversion of resistance and apparent resistivity are identical when considering data weighting. Assuming that the data error e_i is sufficiently small relative to R_i, the limit of Equation 6.3 when $f_i(\boldsymbol{m})$ approaches R_i also approaches Equation 6.1. Therefore, it can be anticipated that the use of logarithmic data becomes nearly the same as the use of regular data when the same data weighting is applied.

To test the above considerations, Model-1 defined in Chapter 2 was again used but only the modelled amplitude of the complex impedance is used to demonstrate the impact of

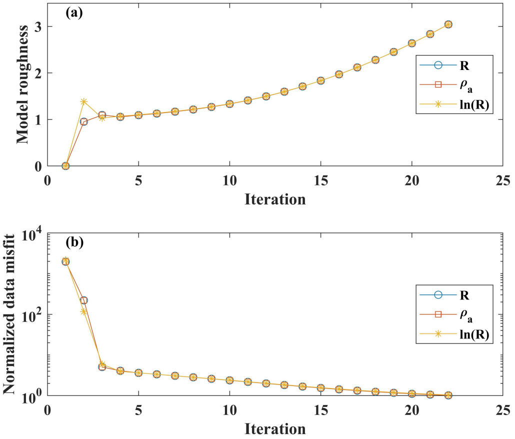

Figure 6.1: (a) Development of the normalized data misfit, and (b) the model roughness during ERT inversion using different data types.

different data types on the ERT inversion results. The inversion starts from a relatively high regularization factor and gradually decreases it to reach the target data misfit. It should be noted that the regularization factors for different data types were the same at the same iteration. Figure 6.1 shows the development of the normalized data misfit and the model roughness for the ERT inversion using different data types. It is clear that the results of using resistance and apparent resistivity completely overlap, indicating the equivalence of these two formulations. The final inverted images produced by these two data types were also examined pixel by pixel and the difference was found to be zero. In the case of logarithmic resistance, apparent differences compared to resistance can be observed at the beginning of the inversion but the curves converged after several iterations. The imaging results were also checked and the maximum relative difference between pixels was below 2%. These results suggest that the different data types do not make a significant difference in the inversion of ERT data as long as a proper data weighting is used. This also provides a solution when dealing with the inversion involving γ type configurations or cross-hole measurements where the intrinsic negative apparent resistivity can appear (*Carpenter and Habberjam*, 1956; *Mura et al.*, 2011). Instead of using logarithmic data, the measured resistance can be directly inverted with a proper data weighting, which allows to consider the additional information provided by these unconventional electrode configurations while stabilizing the inversion. It should be noted that the ERT inversion results using different data types can be different in the absence of data weighting.

The discussion of different data and model types becomes more complicated when complex quantities are involved as in the case of the inversion of EIT measurements. The linear space complex data and model refer to the real and imaginary part of the measured complex impedance and the complex conductivity used in the modelling, while the logarithm of complex data and model refer to the logarithmic amplitude and phase of the measured complex impedance and the complex conductivity. With the use of separated formulations, such as the RVI, ALT, and CVI+ strategies illustrated in Chapter 2 and Chapter 3, logarithmic values can also be used for the real and imaginary part of the complex conductivity and even for the phase. These different data and model types can be arbitrarily combined and none of these combinations is conceptually wrong. For example, one can use the real and imaginary part of the measured impedances as data and the logarithmic amplitude and phase of the complex conductivity as model parameters.

To evaluate the impact of using different data types, it may be feasible to consistently use one type of model parameter. However, to compare the different data types using one type of model parameter, it is important to have reliable error models for different data types and error transformations from one data type to the other. To estimate the error in EIT measurements, normal and reciprocal measurements are commonly used with a multi-bin approach (*Koestel et al.*, 2008). Different error models have been proposed for different data types. For example, linear and inverse power law models have been used for the amplitude and phase of the complex impedances (*Flores Orozco et al.*, 2012b), and linear models have been used for the real and imaginary part of the complex impedance (*LaBrecque et al.*, 1996; *Flores Orozco et al.*, 2012b; *Kelter et al.*, 2015). It has been shown in *Flores Orozco et al.* (2012b) that the error in sEIT measurements in terms of different data types can be well described with the proposed models. However, the transformations between different error models and the resulting impact on the inversion results have not been sufficiently evaluated yet, and should be investigated in more detail. In addition, the performance of these error models in the presence of large phase angles should also be tested.

Regarding the different model types, one interesting point is associated with the choice of electrical conductivity and resistivity. This choice does not make a difference in the case of the ERT problem when using logarithmic model parameters. In the case of EIT, this choice may have an influence on the modelling and inversion when simplifications are made, such as the negligence of the imaginary part model in the modeling of real part data. *Johnson and Thomle* (2018) analyzed the error in the modelled real part of the impedance induced by neglecting the second term in the left-hand side of Equation 5.5. Considering a homogeneous conductivity distribution and a pole-pole configuration, the analytical solution for the complex impedance Z^* is given by

$$Z^* = \frac{1}{2\pi r \sigma^*} \tag{6.4}$$

where r is the distance between the two electrodes and σ^* is the homogeneous complex electrical conductivity. The real part of the impedance Z' according to Equation 6.4 is given by

$$Z' = \frac{\sigma'}{2\pi r(\sigma'^2 + \sigma''^2)} \tag{6.5}$$

where σ' and σ'' are the real and imaginary parts of the complex electrical conductivity, respectively. When the imaginary part of the electrical conductivity is ignored, the approximated real part of the measured impedance Z'_{app} is

$$Z'_{\text{app}} = \frac{1}{2\pi r \sigma'} \tag{6.6}$$

Therefore, *Johnson and Thomle* (2018) concluded that the relative error $rErr$ in the modelled real part of the impedance due to neglecting the imaginary part of the electrical conductivity can be quantified using

$$rErr = \frac{Z'_{\text{app}} - Z'}{Z'} = \left(\frac{\sigma''}{\sigma'}\right)^2 \tag{6.7}$$

This equation suggests that the error is less than 4% for a model with phase angles smaller than 200 mrad.

The same analysis (Equation 6.4 to 6.7) can be repeated using the complex resistivity ρ^* as model. Equation 6.4 can be rewritten as

$$Z^* = \frac{\rho^*}{2\pi r} \tag{6.8}$$

The real part of the impedance Z' according to Equation 6.8 is

$$Z' = \frac{\rho'}{2\pi r} \tag{6.9}$$

When the imaginary part of the complex resistivity is ignored, the approximated real part of the measured impedance is the same as presented in Equation 6.9, resulting in no error in the case of a homogeneous model no matter how large the phase angle is. This indicates that the choice of complex electrical conductivity or resistivity as model may influence the EIT data inversion. Overall, the choice of linear and logarithmic data and model should be investigated and the differences between electrical conductivity and resistivity as model parameter should be clarified in the future to further extend the guidelines for EIT data inversion.

6.2.2 EM coupling reduction

In Chapter 4, the experimental design to reduce inductive coupling has been successfully applied to surface sEIT measurements. It would also be interesting to apply this strategy to borehole EIT measurements. *Zhao et al.* (2015) and *Kelter et al.* (2018) have shown promising results with cross-hole sEIT measurements after correction of inductive coupling and capacitive coupling effects. It was noticed that inductive coupling is much more pronounced than capacitive coupling in cross-hole sEIT measurements because the borehole electrodes are in direct contact with ground water, which results in low contact impedances. Therefore, it is necessary to investigate the proposed approach in terms of cross-hole sEIT measurements to achieve reliable imaging results without correction of inductive coupling. The cable arrangement of cross-hole measurements is similar to the parallel cable layout discussed in Chapter 4. It was shown in Chapter 4 that it is relatively difficult to acquire enough measurements with small ICS using the parallel cable layout. However, in the case of cross-hole surveys where the cable bundles are bended at the opening of the boreholes, part of the mutual inductance will be cancelled out by the 90 ° bending. This may provide room for more measurements with small ICS. The choice of cross-hole electrode configurations should also be taken into account carefully when applying the experimental design. Electrode configurations that have small mutual inductance (e.g. current electrodes and potential electrodes in different boreholes) may have very limited resolution and can be very sensitive to noise (*Zhou and Greenhalgh*, 2000).

Using filtering based on the newly proposed CCS value, reliable inversion results for the imaginary part of the electrical conductivity up to kHz frequencies were achieved in Chapter 5, even in the case of a resistive subsurface. Despite the promising results, one critical problem is the 2.5D assumption. The current flows in 3D and also the electrical conductivity distribution is 3D in reality. In the modelling with leakage current and capacitances, the model must be in 3D to distribute the capacitances. Therefore, the question arises to what extent the 2.5D assumption for the electrical conductivity distribution affects the accuracy of the modelling with 3D distributed capacitances. To investigate this question, two directions of possible work can be identified. One is to develop modelling approaches to simulate the leakage current for a given electrical conductivity distribution and total capacitance. The other direction is to experimentally investigate this topic at a well-investigated site with buried targets. Addressing this question can help understanding the behaviour of capacitive coupling and ensuring accurate modelling and correction of capacitive coupling. Besides the 2.5D assumption, the error associated with the 3D capacitance distribution should also be noted. In Chapter 5, a uniform distribution of the total capacitance was used, indicating that the distance between the ground and the cable shield is the same for all cable segments. In reality, this distance can vary along the cable from millimetres to centimetres. This also is an important aspect that needs to be investigated in more detail.

The results presented in Chapter 5 showed that it is of great importance to measure both leakage currents and the total capacitance if accurate sEIT measurements are required in the presence of capacitive coupling in resistive environments. This has obvious implications for the future direction of system design for commercial sEIT equipment. Determination of the leakage current would on the one hand be useful to model capacitive coupling and calculate the CCS which can then be used for data filtering as shown in this thesis. On the other hand, it could also be used for the on-site determination of an optimized current excitation scheme using a test measurement at a high frequency. In this thesis, a customized sEIT measurement system was used that allows to measure leakage currents and potentials relative to a common ground point, which are both essential to address capacitive coupling. It is not straightforward to apply the method developed in Chapter 5 to commercial devices, but some useful insights on tackling capacitive coupling with such devices can nevertheless be obtained. First of all, it is important to identify the possible paths for leakage current as realized by *Wang and Slater* (2019) for laboratory SIP measurements using a commercially available instrument. The possible paths for leakage current or the types of capacitive coupling can be quite different depending on the design of the measurement instruments, survey setup, and types of cable. When measuring with four electrodes and a single recording channel in a laboratory environment, it is possible to determine the exact current and voltage applied to the sample by additional measurements, for example using the equivalent electric circuit model in *Wang and Slater* (2019). In the case of multi-channel measurement strategies in the field with multiple electrodes, it becomes very challenging to determine the exact amount of current between two arbitrary receivers. In this case, the modelling method and the approach for data filtering proposed in this work are advantageous but require information about the total leakage current and the capacitances. Obtaining this necessary information is not yet possible with commercial devices. Therefore, future development of commercial devices for accurate sEIT measurements should focus on changing the system design such that both leakage currents and the total capacitance can be determined. One strategy to determine the leakage current would be to measure the current with shunt resistors at both ends of the voltage or current sources. It is important to note that shielded cables with a common ground point for all shields are also recommended for accurate sEIT measurements. Without shielded cables with a common ground, it is highly challenging to determine the total capacitance and to model capacitive effects. From a practical perspective, it would also be beneficial to know the leakage current for on-site determination of the current excitations. As well-known and also shown again in this thesis, measurements with low normalized leakage current are preferred. If measured leakage currents would be available, the following strategy to obtain measurements with small leakage current could be applied to obtain accurate field sEIT measurements with multiple electrodes. In a first step, a measurement at a high frequency (e.g. 1 kHz) with all possible combinations of the excitation pairs could be conducted. After this, the normalized leakage current for all excitations could be obtained and electrode combinations with low normalized leakage current could be considered for actual spectral measurements.

Chapter 5 dealt with capacitive coupling between the ground and cable shield. The capacitance of the cable itself was eliminated by using active electrodes where the amplifiers were mounted at the electrodes (*Zimmermann et al.*, 2008a). For commercial systems, a central multiplexer is typically used, which is connected to the electrodes using shielded cables. Therefore, the cable capacitance should additionally be considered when a centralized multiplexer is used. With the approach developed in this study, it is also possible to address this type of capacitive coupling by integrating the cable capacitances at the electrodes in the modelling. Since there is no commercial system that can measure the leakage current yet, a preliminary analysis of the viability of this approach can be performed as a next step using a centralized switching tool attached to the customized EIT40 system.

References

Aal, G. Z. A., L. D. Slater, and E. A. Atekwana (2006), Induced-polarization measurements on unconsolidated sediments from a site of active hydrocarbon biodegradation, *Geophysics*, *71*(2), H13–H24, doi:10.1190/1.2187760.

Acworth, R. I. (1981), The evaluation of groundwater resources in the crystalline basement of Northern Nigeria, PhD thesis, University of Birmingham.

Archie, G. E. (1942), The electrical resistivity log as an aid in determining some reservoir characteristics, *Transactions of the American Institute of Mining and Metallurgical Engineers*, *146*, 54–61, doi:10.2118/942054-g.

Attwa, M., and T. Günther (2013), Spectral induced polarization measurements for predicting the hydraulic conductivity in sandy aquifers, *Hydrology and Earth System Sciences*, *17*(10), 4079–4094, doi:10.5194/hess-17-4079-2013.

Auken, E., L. Pellerin, N. B. Christensen, and K. Sørensen (2006), A survey of current trends in near-surface electrical and electromagnetic methods, *Geophysics*, *71*(5), G249–G260.

Bairlein, K., M. Bücker, A. Hördt, and B. Hinze (2016), Temperature dependence of spectral induced polarization data: experimental results and membrane polarization theory, *Geophysical Journal International*, *205*(1), 440–453, doi:10.1093/gji/ggw027.

Beard, L. P., G. W. Hohmann, and A. C. Tripp (1996), Fast resistivity IP inversion using a low-contrast approximation, *Geophysics*, *61*(1), 169–179, doi:10.1190/1.1443937.

Bergmann, P., C. Schmidt-Hattenberger, T. Labitzke, F. M. Wagner, A. Just, C. Flechsig, and D. Rippe (2017), Fluid injection monitoring using electrical resistivity tomography five years of CO_2 injection at Ketzin, Germany, *Geophysical Prospecting*, *65*(3), 859–875, doi: 10.1111/1365-2478.12426.

Binley, A., L. D. Slater, M. Fukes, and G. Cassiani (2005), Relationship between spectral induced polarization and hydraulic properties of saturated and unsaturated sandstone, *Water Resources Research*, *41*(12), doi:10.1029/2005wr004202.

Blome, M., H. Maurer, and S. Greenhalgh (2011), Geoelectric experimental design - Efficient acquisition and exploitation of complete pole-bipole data sets, *Geophysics*, *76*(1), F15–F26, doi:10.1190/1.3511350.

Cai, G. C., J. Vanderborght, A. Klotzsche, J. van der Kruk, J. Neumann, N. Hermes, and H. Vereecken (2016), Construction of Minirhizotron Facilities for Investigating Root Zone Processes, *Vadose Zone Journal*, *15*(9), doi:10.2136/vzj2016.05.0043.

Carpenter, E., and G. Habberjam (1956), A tri-potential method of resistivity prospecting, *Geophysics*, *21*(2), 455–469, doi:10.1190/1.1438247.

Chambers, J., P. Wilkinson, G. Wealthall, M. Loke, R. Dearden, R. Wilson, D. Allen, and R. Ogilvy (2010), Hydrogeophysical imaging of deposit heterogeneity and groundwater chemistry changes during DNAPL source zone bioremediation, *Journal of Contaminant Hydrology*, *118*(1-2), 43–61.

Chou, T.-K., M. Chouteau, and J.-S. Dube (2016), Intelligent meshing technique for 2D resistivity inverse problems, *Geophysics*, *81*(4), IM45–IM56, doi:10.1190/geo2015-0177.1.

Clifford, J., and A. Binley (2010), Geophysical characterization of riverbed hydrostratigraphy using electrical resistance tomography, *Near Surface Geophysics*, *8*(6), 493–501.

Coggon, J. H. (1984), New 3-point Formulas for inductive doupling removal in induced polarization, *Geophysics*, *49*(3), 307–309, doi:10.1190/1.1441665.

Cole, K. S., and R. H. Cole (1941), Dispersion and absorption in dielectrics I. Alternating current characteristics, *Journal of Chemical Physics*, *9*(4), 341–351, doi:10.1063/1.1750906.

Commer, M., G. A. Newman, K. H. Williams, and S. S. Hubbard (2011), 3D induced-polarization data inversion for complex resistivity, *Geophysics*, *76*(3), F157–F171, doi:10.1190/1.3560156.

Dahlin, T., and V. Leroux (2012), Improvement in time-domain induced polarization data quality with multi-electrode systems by separating current and potential cables, *Near Surface Geophysics*, *10*(6), 545–565, doi:10.3997/1873-0604.2012028.

Dahlin, T., and B. Zhou (2004), A numerical comparison of 2D resistivity imaging with 10 electrode arrays, *Geophysical Prospecting*, *52*(5), 379–398, doi:10.1111/j.1365-2478.2004.00423.x.

Dey, A., and H. F. Morrison (1979), Resistivity modeling for arbitrary shaped 2-dimensional structures, *Geophysical Prospecting*, *27*(1), 106–136, doi:10.1111/j.1365-2478.1979.tb00961.x.

Dimech, A., L. Z. Cheng, M. Chouteau, J. Chambers, S. Uhlemann, P. Wilkinson, P. Meldrum, B. Mary, G. Fabien-Ouellet, and A. Isabelle (2022), A Review on Applications of Time-Lapse Electrical Resistivity Tomography Over the Last 30 Years : Perspectives for Mining Waste Monitoring, *Surveys in Geophysics*, *43*(6), 1699–1759, doi:10.1007/s10712-022-09731-2.

Ellis, R. G., and D. W. Oldenburg (1994), Applied Geophysical Inversion, *Geophysical Journal International*, *116*(1), 5–11, doi:10.1111/j.1365-246X.1994.tb02122.x.

Emerson, H. P., J. E. Szecsody, A. R. Lawter, C. D. Halter, A. R. Mangel, E. H. Fernald, C. T. Resch, K. A. Muller, C. E. Bagwell, M. E. Bowden, O. Qafoku, J. N. Thomle, N. Qafoku, and V. L. Freedman (2021), Spectral Induced Polarization-Biogeochemical Relationships for Remediation Amendment Monitoring, *Report*, Pacific Northwest National Lab. (PNNL), Richland, WA (United States), doi:10.2172/1835069.

Farquharson, C. G., and D. W. Oldenburg (2004), A comparison of automatic techniques for estimating the regularization parameter in non-linear inverse problems, *Geophysical Journal International*, *156*(3), 411–425, doi:10.1111/j.1365-246X.2004.02190.x.

Flores Orozco, A. (2012), Characterization of contaminated sites and monitoring of processes accompanying bioremediation using spectral induced polarization imaging, PhD thesis, Rheinische Friedrich-Wilhelms-Universität Bonn.

Flores Orozco, A., K. H. Williams, P. E. Long, S. S. Hubbard, and A. Kemna (2011), Using complex resistivity imaging to infer biogeochemical processes associated with bioremediation of an uranium-contaminated aquifer, *Journal of Geophysical Research-Biogeosciences*, *116*, doi:10.1029/2010jg001591.

Flores Orozco, A., A. Kemna, C. Oberdoerster, L. Zschornack, C. Leven, P. Dietrich, and H. Weiss (2012a), Delineation of subsurface hydrocarbon contamination at a former hydrogenation plant using spectral induced polarization imaging, *Journal of Contaminant Hydrology*, *136*, 131–144, doi:10.1016/j.jconhyd.2012.06.001.

Flores Orozco, A., A. Kemna, and E. Zimmermann (2012b), Data error quantification in spectral induced polarization imaging, *Geophysics*, *77*(3), E227–E237, doi:10.1190/geo2010-0194.1.

Flores Orozco, A., K. H. Williams, and A. Kemna (2013), Time-lapse spectral induced polarization imaging of stimulated uranium bioremediation, *Near Surface Geophysics*, *11*(5), 531–544, doi:10.3997/1873-0604.2013020.

Flores Orozco, A., L. Aigner, and J. Gallistl (2021), Investigation of cable effects in spectral induced polarization imaging at the field scale using multicore and coaxial cables, *Geophysics*, *86*(1), E59–E75, doi:10.1190/geo2019-0552.1.

Friedel, S. (2003), Resolution, stability and efficiency of resistivity tomography estimated from a generalized inverse approach, *Geophysical Journal International*, *153*(2), 305–316, doi:10.1046/j.1365-246X.2003.01890.x.

Gao, Z., F. H. Haegel, O. Esser, E. Zimmermann, H. Vereecken, and J. A. Huisman (2019), Spectral Induced Polarization of Biochar in Variably Saturated Soil, *Vadose Zone Journal*, *18*(1), doi:10.2136/vzj2018.12.0213.

Geselowitz, D. B. (1971), Application of electrocardiographic lead theory to impedance plethysmography, *Ieee Transactions on Biomedical Engineering*, *BM18*(1), 38–+, doi:10.1109/tbme.1971.4502787.

Geuzaine, C., and J.-F. Remacle (2009), Gmsh: A 3-D finite element mesh generator with built-in pre- and post-processing facilities, *International Journal for Numerical Methods in Engineering*, *79*(11), 1309–1331, doi:10.1002/nme.2579.

Griffiths, D., and R. Barker (1993), Two-dimensional resistivity imaging and modelling in areas of complex geology, *Journal of applied Geophysics*, *29*(3-4), 211–226.

Günther, T. (2004), Inversion methods and resolution analysis for the 2D/3D reconstruction of resistivity structures from DC measurements, PhD thesis, Universitätsbibliothek der TU BAF.

Günther, T., and T. Martin (2016), Spectral two-dimensional inversion of frequency-domain induced polarization data from a mining slag heap, *Journal of Applied Geophysics*, *135*, 436–448, doi:10.1016/j.jappgeo.2016.01.008.

Günther, T., C. Rücker, and K. Spitzer (2006), Three-dimensional modelling and inversion of dc resistivity data incorporating topography - II. Inversion, *Geophysical Journal International*, *166*(2), 506–517, doi:10.1111/j.1365-246X.2006.03011.x.

Hansen, P. C. (1992), Analysis of discrete ill-posed problems by means of the L-curve, *Siam Review*, *34*(4), 561–580, doi:10.1137/1034115.

Henke, H. (2011), *Elektromagnetische Felder: Theorie und Anwendung*, Springer-Verlag.

Huisman, J. A., E. Zimmermann, O. Esser, F. H. Haegel, A. Treichel, and H. Vereecken (2016), Evaluation of a novel correction procedure to remove electrode impedance effects from broadband SIP measurements, *Journal of Applied Geophysics*, *135*, 466–473, doi:10.1016/j.jappgeo.2015.11.008.

Ingeman-Nielsen, T., and F. Baumgartner (2006a), Numerical modelling of complex resistivity effects on a homogenous half-space at low frequencies, *Geophysical Prospecting*, *54*(3), 261–271, doi:10.1111/j.1365-2478.2006.00532.x.

Ingeman-Nielsen, T., and F. Baumgartner (2006b), CR1Dmod: A Matlab program to model 1D complex resistivity effects in electrical and electromagnetic surveys, *Computers & Geosciences*, *32*(9), 1411–1419, doi:10.1016/j.cageo.2006.01.001.

Inzoli, S. (2016), Experimental and statistical methods to improve the reliability of spectral induced polarization to infer litho-textural properties of alluvial sediments, PhD thesis, Universitá Degli Studi Di Milano.

Izumoto, S., J. A. Huisman, Y. Wu, and H. Vereecken (2020), Effect of solute concentration on the spectral induced polarization response of calcite precipitation, *Geophysical Journal International*, *220*(2), 1187–1196.

Johnson, T. C., and J. Thomle (2018), 3-D decoupled inversion of complex conductivity data in the real number domain, *Geophysical Journal International*, *212*(1), 284–296, doi:10.1093/gji/ggx416.

Joyce, R. A., D. R. Glaser, D. D. Werkema, and E. A. Atekwana (2012), Spectral induced polarization response to nanoparticles in a saturated sand matrix, *Journal of Applied Geophysics*, *77*, 63–71, doi:10.1016/j.jappgeo.2011.11.009.

Kelter, M., J. A. Huisman, E. Zimmermann, A. Kemna, and H. Vereecken (2015), Quantitative imaging of spectral electrical properties of variably saturated soil columns, *Journal of Applied Geophysics*, *123*, 333–344, doi:10.1016/j.jappgeo.2015.09.001.

Kelter, M., J. A. Huisman, E. Zimmermann, and H. Vereecken (2018), Field evaluation of broadband spectral electrical imaging for soil and aquifer characterization, *Journal of Applied Geophysics*, *159*, 484–496, doi:10.1016/j.jappgeo.2018.09.029.

Kemna, A. (2000), Tomographic inversion of complex resistivity, *Ruhr-Universität Bochum.*

Kemna, A., A. Binley, G. Cassiani, E. Niederleithinger, A. Revil, L. Slater, K. H. Williams, A. F. Orozco, F. H. Haegel, A. Hordt, S. Kruschwitz, V. Leroux, K. Titov, and E. Zimmermann (2012), An overview of the spectral induced polarization method for near-surface applications, *Near Surface Geophysics*, *10*(6), 453–468, doi:10.3997/1873-0604.2012027.

Koch, K., A. Kemna, J. Irving, and K. Holliger (2011), Impact of changes in grain size and pore space on the hydraulic conductivity and spectral induced polarization response of sand, *Hydrology and Earth System Sciences*, *15*(6), 1785–1794, doi:10.5194/hess-15-1785-2011.

Koestel, J., A. Kemna, M. Javaux, A. Binley, and H. Vereecken (2008), Quantitative imaging of solute transport in an unsaturated and undisturbed soil monolith with 3-D ERT and TDR, *Water Resources Research*, *44*(12), doi:10.1029/2007wr006755.

Krampe, V., P. Edme, and H. Maurer (2021), Optimized experimental design for seismic full waveform inversion: A computationally efficient method including a flexible implementation of acquisition costs, *Geophysical Prospecting*, *69*(1), 152–166, doi:10.1111/1365-2478.13040.

Kulenkampff, J. M., and U. Yaramanci (1993), Frequency-dependent complex resistivity of rock-salt smaples and related petrophysical parameters, *Geophysical Prospecting*, *41*(8), 995–1008, doi:10.1111/j.1365-2478.1993.tb00895.x.

Kwok, Y. K. (2010), *Applied complex variables for scientists and engineers*, Cambridge University Press.

LaBrecque, D. J., M. Miletto, W. Daily, A. Ramirez, and E. Owen (1996), The effects of noise on Occam's inversion of resistivity tomography data, *Geophysics*, *61*(2), 538–548, doi:10.1190/1.1443980.

Leroy, P., A. Revil, A. Kemna, P. Cosenza, and A. Ghorbani (2008), Complex conductivity of water-saturated packs of glass beads, *Journal of Colloid and Interface Science*, *321*(1), 103–117, doi:10.1016/j.jcis.2007.12.031.

Lesmes, D. P., and K. M. Frye (2001), Influence of pore fluid chemistry on the complex conductivity and induced polarization responses of Berea sandstone, *Journal of Geophysical Research-Solid Earth*, *106*(B3), 4079–4090, doi:10.1029/2000jb900392.

Li, Y., and D. W. Oldenburg (1999), *3-D inversion of DC resistivity data using an L-curve criterion*, pp. 251–254, Society of Exploration Geophysicists.

Li, Y., and K. Spitzer (2002), Three-dimensional DC resistivity forward modelling using finite elements in comparison with finite-difference solutions, *Geophysical Journal International*, *151*(3), 924–934, doi:10.1046/j.1365-246X.2002.01819.x.

Loke, M. H. (2004), *Tutorial: 2-D and 3-D electrical imaging surveys*, Birmingham, UK.

Loke, M. H., and R. D. Barker (1996), Rapid least-squares inversion of apparent resistivity pseudosections by a quasi-Newton method, *Geophysical Prospecting*, *44*(1), 131–152, doi:10.1111/j.1365-2478.1996.tb00142.x.

Loke, M. H., J. E. Chambers, and R. D. Ogilvy (2006), Inversion of 2D spectral induced polarization imaging data, *Geophysical Prospecting*, *54*(3), 287–301, doi:10.1111/j.1365-2478.2006.00537.x.

Loke, M. H., P. B. Wilkinson, and J. E. Chambers (2010), Fast computation of optimized electrode arrays for 2D resistivity surveys, *Computers & Geosciences*, *36*(11), 1414–1426, doi:10.1016/j.cageo.2010.03.016.

Loke, M. H., J. E. Chambers, D. F. Rucker, O. Kuras, and P. B. Wilkinson (2013), Recent developments in the direct-current geoelectrical imaging method, *Journal of Applied Geophysics*, *95*, 135–156, doi:10.1016/j.jappgeo.2013.02.017.

Loke, M. H., T. Dahlin, and D. F. Rucker (2014), Smoothness-constrained time-lapse inversion of data from 3D resistivity surveys, *Near Surface Geophysics*, *12*(1), 5–24, doi:10.3997/1873-0604.2013025.

Luo, Y., and G. Zhang (1998), *Theory and application of spectral induced polarization*, Society of exploration geophysicists.

Marshall, D. J., and T. R. Madden (1959), Induced polarization, a study of its causes, *Geophysics*, *24*(4), 790–816.

Martin, T., and T. Günther (2013), Complex resistivity tomography (CRT) for fungus detection on standing oak trees, *European Journal of Forest Research*, *132*(5-6), 765–776, doi:10.1007/s10342-013-0711-4.

Maurer, H., S. Greenhalgh, and S. Latzel (2009), Frequency and spatial sampling strategies for crosshole seismic waveform spectral inversion experiments, *Geophysics*, *74*(6), WCC79–WCC89, doi:10.1190/1.3157252.

Mellage, A., A. B. Holmes, S. Linley, L. Vallee, F. Rezanezhad, N. Thomson, F. Gu, and P. Van Cappellen (2018a), Sensing Coated Iron-Oxide Nanoparticles with Spectral Induced Polarization (SIP): Experiments in Natural Sand Packed Flow Through Columns, *Environmental Science & Technology*, *52*(24), 14,256–14,265, doi:10.1021/acs.est.8b03686.

Mellage, A., C. M. Smeaton, A. Furman, E. A. Atekwana, F. Rezanezhad, and P. Van Cappellen (2018b), Linking Spectral Induced Polarization (SIP) and Subsurface Microbial Processes: Results from Sand Column Incubation Experiments, *Environmental Science & Technology*, *52*(4), 2081–2090, doi:10.1021/acs.est.7b04420.

Mudler, J., A. Hördt, D. Kreith, M. Sugand, K. Bazhin, L. Lebedeva, and T. Radić (2022), Broadband spectral induced polarization for the detection of Permafrost and an approach to ice content estimation - a case study from Yakutia, Russia, *Cryosphere*, *16*(11), 4727–4744, doi:10.5194/tc-16-4727-2022.

Mura, M., G. Deidda, and F. Schirru (2011), Negative Apparent Resistivity and Chargeability in Crosshole Electrical Surveys, in *73rd EAGE Conference and Exhibition incorporating SPE EUROPEC 2011*, pp. cp–238–00,562, European Association of Geoscientists & Engineers, doi:10.3997/2214-4609.20149506.

Murai, T., and Y. Kagawa (1985), Electrical impedance computed tomography based on a finite element model, *IEEE Transactions on Biomedical Engineering*, *32*(3), 177–184, doi:10.1109/tbme.1985.325526.

Oldenburg, D. W., and Y. G. Li (1994), Inversion of induced polarization data, *Geophysics*, *59*(9), 1327–1341, doi:10.1190/1.1443692.

Park, S. (1998), Fluid migration in the vadose zone from 3-D inversion of resistivity monitoring data, *Geophysics*, *63*(1), 41–51, doi:10.1190/1.1444326.

Park, S. K., and G. P. Van (1991), Inversion of pole-pole data for 3D resistivity structure beneath arrays of electrodes, *Geophysics*, *56*(7), 951–960, doi:10.1190/1.1443128.

Pelton, W. H., S. H. Ward, P. G. Hallof, W. R. Sill, and P. H. Nelson (1978), Mineral discrimination and removal of inductive coupling with multifrequency-IP, *Geophysics*, *43*(3), 588–609, doi:10.1190/1.1440839.

Peruzzo, L., X. Liu, C. Chou, E. B. Blancaflor, H. Zhao, X. Ma, B. Mary, V. Iván, M. Weigand, and Y. Wu (2021), Three-channel electrical impedance spectroscopy for field-scale root phenotyping, *The Plant Phenome Journal*, *4*(1), e20,021.

Pidlisecky, A., and R. Knight (2008), FW25D: A MATLAB 2.5-D electrical resistivity modeling code, *Computers & Geosciences*, *34*(12), 1645–1654, doi:https://doi.org/10.1016/j.cageo.2008.04.001.

Radić, T. (2004), Elimination of cable effects while multi-channel SIP measurements, in *Near Surface 2004-10th EAGE European Meeting of Environmental and Engineering Geophysics*, pp. cp–10, European Association of Geoscientists & Engineers.

Rayner, S. F., L. R. Bentley, and D. M. Allen (2007), Constraining aquifer architecture with electrical resistivity imaging in a fractured hydrogeological setting, *Journal of Environmental and Engineering Geophysics*, *12*(4), 323–335.

Revil, A. (2012), Spectral induced polarization of shaly sands: Influence of the electrical double layer, *Water Resources Research*, *48*, doi:10.1029/2011wr011260.

Revil, A., and N. Florsch (2010), Determination of permeability from spectral induced polarization in granular media, *Geophysical Journal International*, *181*(3), 1480–1498, doi:10.1111/j.1365-246X.2010.04573.x.

Revil, A., K. Koch, and K. Holliger (2012), Is it the grain size or the characteristic pore size that controls the induced polarization relaxation time of clean sands and sandstones?, *Water Resources Research*, *48*, doi:10.1029/2011wr011561.

Revil, A., A. Coperey, Z. Shao, N. Florsch, I. L. Fabricius, Y. Deng, J. R. Delsman, P. S. Pauw, M. Karaoulis, P. G. B. de Louw, E. S. van Baaren, W. Dabekaussen, A. Menkovic, and J. L. Gunnink (2017), Complex conductivity of soils, *Water Resources Research*, *53*(8), 7121–7147, doi:10.1002/2017wr020655.

Routh, P. S., and D. W. Oldenburg (2001), Electromagnetic coupling in frequency-domain induced polarization data: a method for removal, *Geophysical Journal International*, *145*(1), 59–76, doi:10.1111/j.1365-246X.2001.00384.x.

Sasaki, Y. (1992), Resolution of resistivity tomography inferred from numerical simulation, *Geophysical Prospecting*, *40*(4), 453–463, doi:10.1111/j.1365-2478.1992.tb00536.x.

Schütze, C., T. Vienken, U. Werban, P. Dietrich, A. Finizola, and C. Leven (2012), Joint application of geophysical methods and Direct Push-soil gas surveys for the improved delineation of buried fault zones, *Journal of Applied Geophysics*, *82*, 129–136.

Skold, M., A. Revil, and P. Vaudelet (2011), The pH dependence of spectral induced polarization of silica sands: Experiment and modeling, *Geophysical Research Letters*, *38*(12).

Slater, L., and A. Binley (2006), Synthetic and field-based electrical imaging of a zerovalent iron barrier: Implications for monitoring long-term barrier performance, *Geophysics*, *71*(5), B129–B137, doi:10.1190/1.2235931.

Slater, L., and D. P. Lesmes (2002), Electrical-hydraulic relationships observed for unconsolidated sediments, *Water Resources Research*, *38*(10), doi:10.1029/2001wr001075.

Smith, T., M. Hoversten, E. Gasperikova, and F. Morrison (1999), Sharp boundary inversion of 2D magnetotelluric data, *Geophysical Prospecting*, *47*(4), 469–486, doi:10.1046/j.1365-2478.1999.00145.x.

Stummer, P., H. Maurer, and A. G. Green (2004), Experimental design: Electrical resistivity data sets that provide optimum subsurface information, *Geophysics*, *69*(1), 120–139, doi:10.1190/1.1649381.

Sunde, E. D. (1968), *Earth conduction effects in transmission systems*, Dover Publications Inc.

Szalai, S., K. Szokoli, E. Pracser, M. Metwaly, M. Zubair, and L. Szarka (2020), An alternative way in electrical resistivity prospection: the quasi-null arrays, *Geophysical Journal International*, *220*(3), 1463–1480, doi:10.1093/gji/ggz518.

Tarasov, A., and K. Titov (2013), On the use of the Cole-Cole equations in spectral induced polarization, *Geophysical Journal International*, *195*(1), 352–356, doi:10.1093/gji/ggt251.

Tikhonov, A. N., and V. Y. Arsenin (1977), Solutions of ill-posed problems. Scripta Series in Mathematics, *Washington, DC, USA: Winston.*

Tsukanov, K., and N. Schwartz (2021), Modeling Plant Roots Spectral Induced Polarization Signature, *Geophysical Research Letters*, *48*(5), doi:10.1029/2020gl090184.

Ulrich, C., and L. D. Slater (2004), Induced polarization measurements on unsaturated, unconsolidated sands, *Geophysics*, *69*(3), 762–771, doi:10.1190/1.1759462.

Vogel, C. R. (2002), *Computational methods for inverse problems*, Society for Industrial and Applied Mathematics.

Wagner, F. M., T. Gunther, C. Schmidt-Hattenberger, and H. Maurer (2015), Constructive optimization of electrode locations for target-focused resistivity monitoring, *Geophysics*, *80*(2), E29–E40, doi:10.1190/geo2014-0214.1.

Wait, J. R. (1984), Electromagnetic response of a discretely grounded circuit, *Geophysics*, *49*(5), 577–580, doi:10.1190/1.1441692.

Wait, J. R., and T. P. Gruszka (1986), On electromagnetic coupling removal from induced polarization surveys, *Geoexploration*, *24*(1), 21–27, doi:10.1016/0016-7142(86)90016-5.

Wang, C., and L. D. Slater (2019), Extending accurate spectral induced polarization measurements into the kHz range: modelling and removal of errors from interactions between the parasitic capacitive coupling and the sample holder, *Geophysical Journal International*, *218*(2), 895–912, doi:10.1093/gji/ggz199.

Wang, H., J. A. Huisman, E. Zimmermann, and H. Vereecken (2021), Experimental design to reduce inductive coupling in spectral electrical impedance tomography (sEIT) measurements, *Geophysical Journal International*, *225*(1), 222–235, doi:10.1093/gji/ggaa594.

Wang, H., C. P. Lin, T. H. Mok, P. L. Wu, and H. C. Liu (2022), High-fidelity subsurface resistivity imaging incorporating borehole measurements for monitoring underground construction, *Engineering Geology*, *299*, doi:10.1016/j.enggeo.2022.106558.

Waxman, M. H., and L. J. M. Smits (1968), Electrical conductivities in oil-bearing shaly sands, *Society of Petroleum Engineers Journal*, *8*(2), 107–+, doi:10.2118/1863-a.

Weigand, M., and A. Kemna (2019), Imaging and functional characterization of crop root systems using spectroscopic electrical impedance measurements, *Plant and Soil*, *435*(1-2), 201–224, doi:10.1007/s11104-018-3867-3.

Weigand, M., E. Zimmermann, V. Michels, J. A. Huisman, and A. Kemna (2022), Design and operation of a long-term monitoring system for spectral electrical impedance tomography (sEIT), *Geosci. Instrum. Method. Data Syst. Discuss.*, *2022*, 1–35, doi:10.5194/gi-2021-36.

Weihermüller, L., J. A. Huisman, S. Lambot, M. Herbst, and H. Vereecken (2007), Mapping the spatial variation of soil water content at the field scale with different ground penetrating radar techniques, *Journal of Hydrology*, *340*(3-4), 205–216, doi:10.1016/j.jhydrol.2007.03.013.

Weller, A., M. Seichter, and A. Kampke (1996), Induced-polarization modelling using complex electrical conductivities, *Geophysical Journal International*, *127*(2), 387–398, doi:10.1111/j.1365-246X.1996.tb04728.x.

Weller, A., M. Gruhne, F. D. Börner, and M. Seichter (1997), Monitoring hydraulic experiments by complex conductivity tomography, *European Journal of Environmental and Engineering Geophysics*, *1*, 209–228.

Wilkinson, P. B., P. I. Meldrum, J. E. Chambers, O. Kuras, and R. D. Ogilvy (2006a), Improved strategies for the automatic selection of optimized sets of electrical resistivity tomography measurement configurations, *Geophysical Journal International*, *167*(3), 1119–1126, doi:10.1111/j.1365-246X.2006.03196.x.

Wilkinson, P. B., J. E. Chambers, P. I. Meldrum, R. D. Ogilvy, and S. Caunt (2006b), Optimization of array configurations and panel combinations for the detection and imaging of abandoned mineshafts using 3D cross-hole electrical resistivity tomography, *Journal of Environmental and Engineering Geophysics*, *11*(3), 213–221, doi:10.2113/jeeg11.3.213.

Williams, K. H., A. Kemna, M. J. Wilkins, J. Druhan, E. Arntzen, A. L. N'Guessan, P. E. Long, S. S. Hubbard, and J. F. Banfield (2009), Geophysical monitoring of coupled microbial and geochemical processes during stimulated subsurface bioremediation, *Environmental Science & Technology*, *43*(17), 6717–6723.

Xu, B. W., and M. Noel (1993), On the completeness of data sets with nultielectrode systems for electrical resistivity survey, *Geophysical Prospecting*, *41*(6), 791–801, doi:10.1111/j.1365-2478.1993.tb00885.x.

Xu, S. Z., B. C. Duan, and D. H. Zhang (2000), Selection of the wavenumbers k using an optimization method for the inverse Fourier transform in 2.5D electrical modelling, *Geophysical Prospecting*, *48*(5), 789–796, doi:10.1046/j.1365-2478.2000.00210.x.

Zhao, Y. (2017), Numerical modeling of electromagnetic coupling effects for phase correction in borehole EIT measurements, PhD thesis, Rheinische Friedrich-Wilhelms-Universität Bonn.

Zhao, Y., E. Zimmermann, J. A. Huisman, A. Treichel, B. Wolters, S. van Waasen, and A. Kemna (2013), Broadband EIT borehole measurements with high phase accuracy using numerical corrections of electromagnetic coupling effects, *Measurement Science and Technology*, *24*(8), doi:10.1088/0957-0233/24/8/085005.

Zhao, Y., E. Zimmermann, J. A. Huisman, A. Treichel, B. Wolters, S. van Waasen, and A. Kemna (2015), Phase correction of electromagnetic coupling effects in cross-borehole EIT measurements, *Measurement Science and Technology*, *26*(1), doi:10.1088/0957-0233/26/1/015801.

Zhou, B., and S. A. Greenhalgh (2000), Cross-hole resistivity tomography using different electrode configurations, *Geophysical Prospecting*, *48*(5), 887–912, doi:10.1046/j.1365-2478.2000.00220.x.

Zimmermann, E. (2011), Phasengenaue Impedanzspektroskopie und -tomographie für geophysikalische Anwendungen, PhD thesis, Rheinische Friedrich-Wilhelms-Universität Bonn.

Zimmermann, E., A. Kemna, J. Berwix, W. Glaas, and H. Vereecken (2008a), EIT measurement system with high phase accuracy for the imaging of spectral induced polarization properties of soils and sediments, *Measurement Science and Technology*, *19*(9), doi:10.1088/0957-0233/19/9/094010.

Zimmermann, E., A. Kemna, J. Berwix, W. Glaas, H. M. Muench, and J. A. Huisman (2008b), A high-accuracy impedance spectrometer for measuring sediments with low polarizability, *Measurement Science and Technology*, *19*(10), doi:10.1088/0957-0233/19/10/105603.

Zimmermann, E., J. Huisman, A. Kemna, J. Berwix, W. Glaas, H. Meier, B. Wolters, and O. Esser (2010), Advanced electrical impedance tomography system with high phase accuracy, in *Proceedings of the 6th World Congress on industrial process tomography (WCIPT6), Beijing, China*, pp. 583–591.

Zimmermann, E., J. A. Huisman, A. Mester, and S. van Waasen (2019), Correction of phase errors due to leakage currents in wideband EIT field measurements on soil and sediments, *Measurement Science and Technology*, *30*(8), doi:10.1088/1361-6501/ab1b09.